CAVITY-ENHANCED EVANESCENT-WAVE CHEMICAL SENSING USING MICRORESONATORS

By

GEORGE FARCA

Bachelor of Science
West University of Timisoara
Timisoara, Romania
1996

Submitted to the Faculty of the
Graduate College of the
Oklahoma State University
in partial fulfillment of
the requirements for
the Degree of
DOCTOR OF PHILOSOPHY
December, 2006

CAVITY-ENHANCED EVANESCENT-WAVE

CHEMICAL SENSING USING

MICRORESONATORS

Dissertation Approved:

Albert T. Rosenberger
Dissertation Adviser

Donna K. Bandy

Gil Summy

Daniel Grischkowsky

A. Gordon Emslie
Dean of the Graduate College

ACKNOWLEDGEMENT

Amicus certus in re incerta cernitur.

I would like to thank all my *amici* who supported me throughout the years in the academic field or in a personal nature. I would like to give my special appreciation to my wife, Anca, for her love, endless words of encouragement, patience, and understanding. I also wish to express my wholehearted appreciation to my advisor, Dr. Rosenberger, for his vast expertise and working model he offered me, his patient and constructive guidance, his speedy comments on my numerous tedious drafts, and his kind words of encouragement. I hope my other committee members, Dr. Bandy, Dr. Summy, and Dr. Grischkowsky will also accept my sincere appreciation for their suggestions, guidance, and support throughout the pursuit of this degree.

I am grateful to all my friends and colleagues in the Physics Department, in particular to Siyka Shopova for her generous support during the long hour in the lab. Together we constituted a strong team.

In addition, I would like to thank my parents and my brother for the love and support they have given me all my life.

TABLE OF CONTENTS

LIST OF TABLES

LIST OF FIGURES

CHAPTER I

INTRODUCTION

1. Overview

Optical resonators are widely used in various areas of research and the use of standard mirror-based resonators is often limited due to their size, stability, and quality factor. Dielectric microresonators using optical whispering-gallery modes (WGMs), on the other hand, have quality factors as large as 10^{10} [1], are extremely stable or can be easily stabilized [2], and their typical size does not exceed 1 mm in diameter.

A WGM is a mode of propagation guided along a curved, closed, and connected boundary. Such a phenomenon was first investigated at the beginning of the last century for sound waves inside the dome of St. Paul's Cathedral in London [3-5]. A mathematical treatment for electromagnetic waves in dielectric spheres was developed by Debye [6] followed by Mie with a theoretical investigation of scattering of plane electromagnetic waves by spheres [7]. Initially, dielectric WGM resonators were studied in the microwave and millimeter-wave regime [8,9]. At optical wavelengths the first observation of WGMs in dielectric materials was made possible by the advent of laser technology.

Optical WGM microresonators of various geometries can be produced including cylindrical [10], toroidal [11], spherical [12], spheroidal [13], and disk shaped [14],

depending on their application. By far the most promising geometries are the cylindrical and the spheroidal given the ease of manufacturing them.

Optical WGM resonances have been studied in various materials including liquid droplets [15,16], polymers [17-21], fused silica, and transparent crystals [22-27]. Given the fact that liquid droplets are extremely difficult to handle and the fact that polymer microresonators have small quality factors due to their rather large absorption the remaining choices for a robust and high quality resonator are the use of either fused silica or crystalline microresonators. Nevertheless, high quality crystalline resonators are rather difficult to obtain using very involved polishing techniques.

In the present work the WGM microresonators are produced from readily available and inexpensive fused silica. Cylindrical resonators are obtained by carefully removing the jacket from standard optical fiber, the remaining cylinder having a surface roughness small enough to produce quality factors exceeding 10^7 [28,29]. Spheroidal microresonators are obtained by melting the end of an unjacketed optical fiber. The molten fused silica takes a spheroidal shape due to surface tension, resulting in a high quality microresonator with a surface roughness of less than 1 nm. Quality factors exceeding 10^9 were obtained in such a microresonator.

Due to their high quality factors and large field densities WGM resonators were used for resonant enhancement of nonlinear interactions of various kinds [30-35]. WGM resonances provided a high nonlinear response even from materials with low nonlinearity.

Considerable effort was dedicated to using WGM resonators in conjunction with a gain medium in order to obtain laser emission. The first lasers based on WGM resonators

were investigated using solid state resonators [22,23,36]. Other investigations revealed laser emission from liquid droplets [37-42] and microspheres doped with rare earth ions [43-46]. An important advancement in microlaser development based on WGM resonators was realized with the surface coating of the microresonator using semiconductor nanoparticles as gain medium. In this manner ultra-low threshold continuous-wave laser emission was obtained at room temperature using HgTe quantum dots [47]. By selecting the size and composition of the quantum dots the laser emission can be tuned over a wide wavelength region.

The use of WGM resonators as chemical or biosensors was also envisioned and most of the effort was geared towards monitoring the WGM resonance shift of a coated microresonator in the presence of an analyte [48-55]. In principle the microresonator is coated with a binding agent that permits the selective attachment to the surface of the molecule of interest. This results in a small change in the index of refraction and triggers a shift of a WGM resonance. Nevertheless, in spite of its advantage of selective detection this method relies on the detection of WGM frequency shifts on the order of a fiftieth of a WGM linewidth, or ~ 4 MHz. It is well known that the temperature variation produces WGM frequency shifts as large as 1.6 GHz per degree Celsius [56], and separating the shifts due to molecular surface adsorption from the thermal shifts could be quite challenging.

Other sensors based on the observation of the quality factor spoiling with the presence of chemicals within the evanescent fraction of a WGM were also proposed. Besides being a parameter difficult to monitor in a real life setup, the quality factor measurement can be adversely affected by thermal effects. Depending on the scan

direction and speed the WGM resonances could appear narrower when the scan direction is towards lower wavelength and wider for scans towards longer wavelengths [56]. This thermal bistability effect is due to the fact that as light enters a WGM resonance the resonance position shifts thermally towards longer wavelengths.

The WGM sensor described in this dissertation is immune to thermal effects as the parameter monitored is the amplitude of a WGM resonance. Besides the benefit of thermal immunity it also permits the development of a novel type of spectroscopic technique analogous to Laser Spectroscopy (LS). Instead of scanning an absorption profile with a tunable laser and monitoring the changes in the intensity with frequency, a WGM resonance is locked to the laser [2] and it follows the laser scan over the absorption profile. Changes in the WGM resonance amplitude are monitored and an enhancement of the detection pathlength is obtained due to the fact that on resonance an average photon executes thousands of cavity round trips, interacting many times with the analyte.

An outlook of this dissertation follows. In the rest of Chapter I, the microresonator and input tapered fiber fabrication methods are presented. Adiabatically tapering the input fiber is a requirement for all the experiments described in this dissertation. As such, an exact treatment of the fiber modes along with a tapering method is developed.

In Chapter II the theoretical model for a WGM resonator is described, both for cylindrical and for spherical microresonators used in this work. A novel experimental method is also presented for non-invasive determination of the WGM resonance coupling regime.

Chapter III describes the use of a WGM resonator for a cavity-enhanced LS experiment along with other detection mechanisms for detecting trace gases in the atmosphere. Long effective absorption path lengths are obtained, orders of magnitude larger than the linear dimension of the detection area. The frequency tuning of a cylindrical WGM resonance that is realized using a piezoelectric transducer (PZT) to stretch the microresonator is also described, along with the lock-in mechanism for locking a WGM to a scanning laser.

Chapter IV experimentally investigates the ability to detect nano-molar concentrations of absorbing analytes in a liquid solution using microsphere WGM resonances. Effective absorption pathlengths on the order of meters are obtained for the first time in a highly absorbing solvent. Also, a new experimental method for determining the evanescent fraction of a WGM resonance is presented. Our method, much simpler than previous proposed methods [52-54] produces results in good agreement with the theoretical predictions.

Surface functionalization of WGM microresonators for selective detection of analytes in solution is investigated in Chapter V and introduces a new analyte-functionalization layer pair.

Chapter VI concludes this work, describing a few perspectives and possible directions towards improving our sensors.

2. Microresonator fabrication

Two types of microresonators were used in this work: spherical and cylindrical depending on their use. For all the gas sensing experiments the cylindrical microresonators were used mainly because they could be easily mounted across a stretching device intended to tune the WGM resonances excited along their circumference. For the liquid sensing experiments the microspheres were used since the absorption profiles of the dyes investigated cover a wide wavelength range overlapping with many WGMs and, as such, no tuning of the WGM resonances is required.

The microspheres are fabricated by melting an end of an optical fiber in a hydrogen-oxygen flame. Hydrogen is used for fueling the flame for two main reasons: it burns at a very high temperature suited for melting fused silica and it creates a very clean flame with no solid residues. In principle, even cleaner microspheres can be created by using a CO_2 laser to melt the optical fiber. But besides being a technically difficult task it does not result in significantly improved microresonators. Figure I.1 describes the microsphere fabrication process.

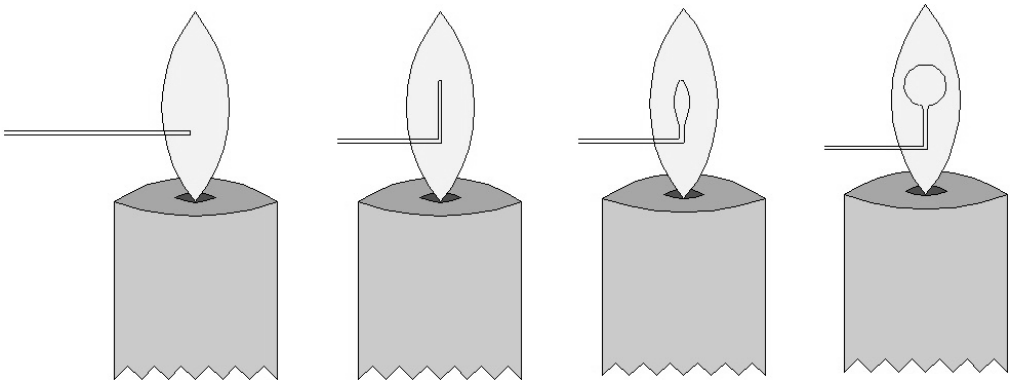

Figure I.1. Microsphere fabrication sequence.

After removing the jacket the fiber is carefully cleaned and then inserted horizontally into the H_2-O_2 flame. As the fiber softens it bends up, pushed by the flame pressure. The end of the fiber reaches the hottest region of the flame and it begins to melt. The surface tension brings the molten fused silica into a spherical shape. Constantly feeding more fiber horizontally inside the flame adds more and more molten fused silica into the microsphere formed increasing its size. When the desired size is obtained the microsphere is removed slowly out of the flame. The rest of the fiber is left attached. It is used for handling the microsphere. Microspheres with diameters ranging from 80 μm to 1000 μm could be fabricated in this manner. For microspheres with the diameter less than 125 μm, the diameter of a standard fiber used in the lab, a previously tapered fiber was used.

The cylindrical microresonators are actually pieces of optical fiber. In order to obtain a clean surface, the jacket is removed by softening it in acetone until it falls off the fiber. The remaining fiber is then carefully cleaned using acetone and methanol repeatedly. If the diameter of the microcylinder has to be smaller than 125 μm the fiber is tapered to a smaller cylindrical waist.

3. Taper fabrication, Adiabaticity

Tapered optical fibers are used in many applications: they can be used as absorption sensors, fiber couplers, splitters, and also as a way of injecting light from an optical fiber into whispering-gallery mode resonators. Although not a necessity, oftentimes it is convenient that the light propagating along the tapered fiber remain in a single mode. Such a taper is called adiabatic.

In this section the investigation focuses on the mode evolution in a step-index tapered fiber (Corning SMF 28), at a wavelength of 1550 nm, and the conditions required for obtaining single mode propagation throughout the entire tapered region. The task addressed is to create a tapered profile that meets the adiabaticity criteria and has the shortest possible length. The mathematical model is solved using *Mathematica* code and can be used for any other kind of step-index optical fiber, at any other wavelength, provided that the geometry of the fiber and the indices of refraction for the core and the cladding are known.

Previous papers [57,58] obtain the adiabaticity criteria by approximating the modes propagating through the taper as LP_{lm} modes that are actually a superposition of the $HE_{l+1,m}$ and $EH_{l-1,m}$, an approximation that simplifies the field components. This is justified in their case by the fact that the degree of tapering is not too large so that the field in the air surrounding the taper is negligibly small. This is not the case when the taper is to be used as a coupler. The very field extending outside the tapered fiber is responsible for coupling the light out. Thus, this section will use the HE_{lm} denomination for the modes along with the appropriate mathematical model.

The HE_{lm} modes

In order to obtain the propagation constants in a step-index dielectric waveguide one has to solve the following equation [59]:

$$\left(\frac{J'_l(ha)}{haJ_l(ha)}+\frac{K'_l(qa)}{qaK_l(qa)}\right)\left(\frac{n_1^2J'_l(ha)}{haJ_l(ha)}+\frac{n_2^2K'_l(qa)}{qaK_l(qa)}\right)=l^2\left[\left(\frac{1}{qa}\right)^2+\left(\frac{1}{ha}\right)^2\right]^2\left(\frac{\beta}{k_0}\right)^2 . \quad \text{(I.1)}$$

This is the so-called characteristic equation. It is obtained by rewriting the wave equation in cylindrical coordinates and applying the proper boundary conditions. J_l and K_l are the modified Bessel functions of the first and second kind, respectively, of order l. The constants in the equation are: $h^2 = n_1{}^2k_0{}^2 - \beta^2$, $q^2 = \beta^2 - n_2{}^2 k_0{}^2$ where n_1 is the core index of refraction, n_2 is the cladding index of refraction, k_0 is the vacuum wave vector, β is the propagation constant and a is the radius of the waveguide. Depending on the situation a is either the core diameter when the propagation is core-guided, or the radius of the cladding when the propagation is cladding-guided.

Solving Eq. (I.1) for $J'_l(ha)/ha\,J_l(ha)$ gives:

$$\frac{J'_l(ha)}{haJ_l(ha)}=-\left(\frac{n_1^2+n_2^2}{2n_1^2}\right)\frac{K'_l(qa)}{qaK_l(qa)}\pm\left[\left(\frac{n_1^2-n_2^2}{2n_1^2}\right)^2\left(\frac{K'_l(qa)}{qaK_l(qa)}\right)^2+\frac{l^2}{n_1^2}\left(\frac{\beta}{k_0}\right)^2\left(\frac{1}{q^2a^2}+\frac{1}{h^2a^2}\right)^2\right]^{1/2}, \quad \text{(I.2)}$$

which, using Bessel function relations gives the following solutions:

$$\begin{aligned}\frac{J_{l+1}(ha)}{haJ_l(ha)}&=\frac{n_1^2+n_2^2}{2n_1^2}\frac{K'_l(qa)}{qaK_l(qa)}+\left(\frac{1}{(ha)^2}-R\right)\\ \frac{J_{l-1}(ha)}{haJ_l(ha)}&=-\left(\frac{n_1^2+n_2^2}{2n_1^2}\right)\frac{K'_l(qa)}{qaK_l(qa)}+\left(\frac{1}{(ha)^2}-R\right)\end{aligned}, \quad \text{(I.3)}$$

where

$$R = \left[\left(\frac{n_1^2 - n_2^2}{2n_1^2} \right)^2 \left(\frac{K'_l(qa)}{qaK_l(qa)} \right)^2 + \left(\frac{l\beta}{n_1 k_0} \right)^2 \left(\frac{1}{q^2 a^2} + \frac{1}{h^2 a^2} \right)^2 \right]^{1/2} . \qquad \text{(I.4)}$$

The two solutions in Eq. (I.3) correspond to the EH and HE modes respectively. For the particular case in which $l = 0$ the TM and TE modes are obtained. The HE_{lm} denomination refers to the solutions of Eq. (I.3) for values of $l \neq 0$. For $l = 1$ the solutions can be obtained either graphically by looking at the intersection point between the plotted LHS and RHS functions in Eq. (I.3), or numerically.

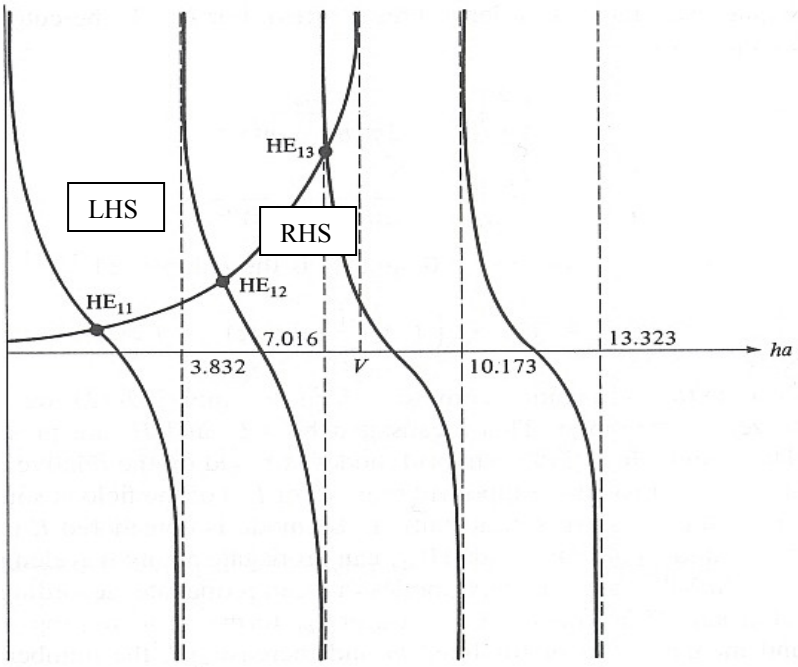

Figure I.2 The first three solutions for the HE_{lm} modes. LHS and RHS of Eq. I.3 are plotted for increasing values of *ha*.
(Reproduced from [59])

It is useful to introduce the following parameters:

$$V = \frac{2\pi a}{\lambda}\sqrt{n_1^2 - n_2^2}\,, \tag{I.5}$$

the normalized frequency, and

$$n_{eff} = \beta / k_0\,, \tag{I.6}$$

the normalized propagation constant or the effective index of refraction. By plotting the normalized propagation constant versus the normalized frequency (Fig. I.3) it can be seen that the HE_{11} mode (often called the fundamental mode) does not have a cutoff, and it is still a guided mode for even the smallest core radius. That is true for a core surrounded by an infinite cladding. In the real case of an optical fiber with a finite cladding diameter, there is a certain cladding diameter at which the core-guided mode extends so far out of the core that it reaches the boundary between the cladding and the surrounding air and starts being guided more strongly by the cladding-air interface. Often referred to as the "core-mode cutoff" it is not a real cutoff since the mode does not cease to be bound but continues to propagate in the cladding.

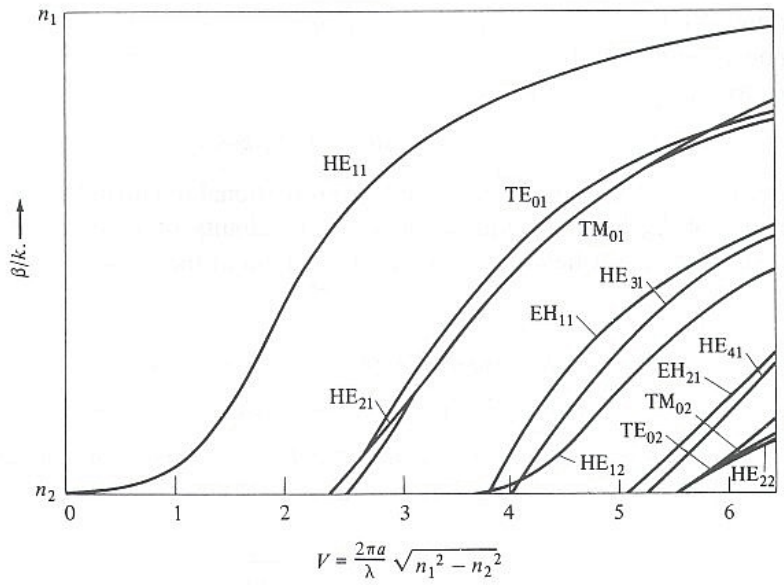

Figure I.3 Normalized propagation constant as a function of the normalized frequency. (Reproduced from [59])

In Figure I.3 it can be seen that in between the cutoff conditions for HE_{11} and HE_{12} there are other modes that can also propagate through the tapered region of the fiber. Since the taper is assumed to be axially symmetric, light from the fundamental mode can only couple to modes that have the same azimuthal symmetry (Figure I.4). The next section only concentrates on the conditions required to avoid coupling from HE_{11} into the HE_{12} mode of the cladding.

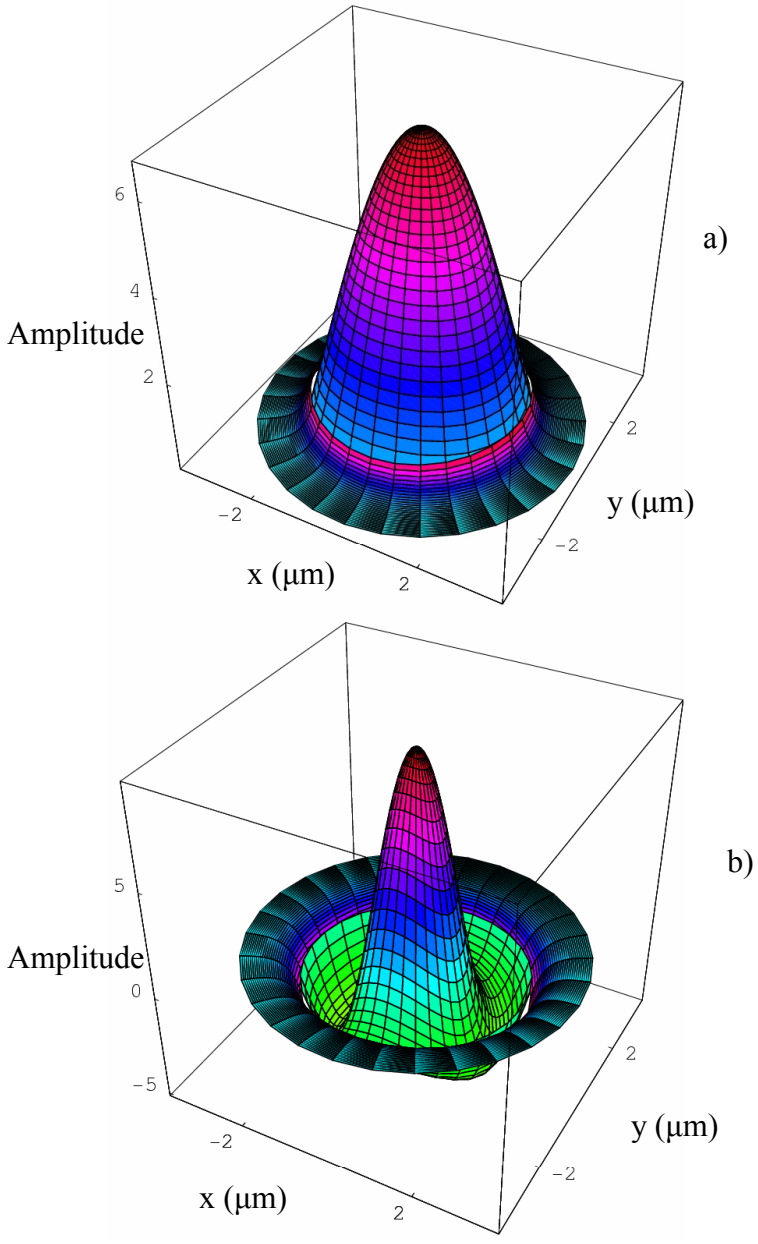

Figure I.4 a) HE_{11} mode of the cladding; b) HE_{12} mode of the cladding. (Reproduced from [60])

The Tapering Process

In order to prepare a bi-conical tapered optical fiber the best choice is to use the "flame brush" technique [61]. The fiber is attached on two motorized translation stages and the jacket is removed in between the stages over a length of approximately 15 mm. Underneath the stripped area of the fiber a hydrogen torch is installed, again on a motorized translation stage. As the two stages move away from each other at a relatively low speed (2 mm/min.), the hydrogen flame continuously "brushes" the stripped fiber along its length, back and forth, at a considerably higher constant speed (120 mm/min.) over a distance that can be changed in time.

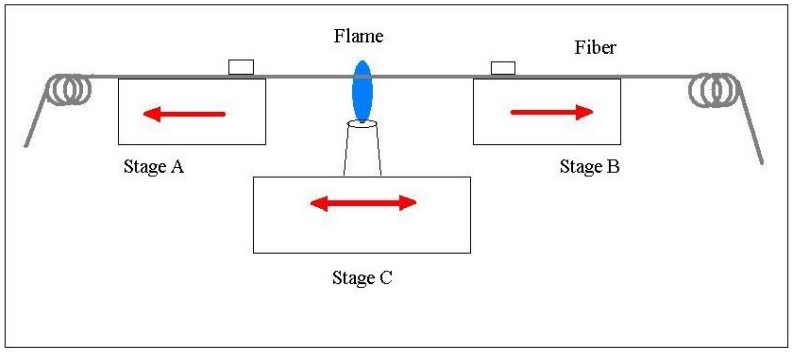

Figure I.5 Device for tapering optical fibers.

Brushing with the hydrogen flame creates a uniformly heated length along the fiber. The uniformly heated length can then be modified in order to obtain the desired shape of the taper [62]. The temperature on the uniformly heated length is carefully chosen by adjusting both the position of the flame with respect to the fiber and by controlling the hydrogen flow. The uniformly heated length should reach the "softening point", a temperature at which the fiber becomes soft enough to be pulled into a taper and stiff enough not to break.

As mentioned earlier, at a certain taper diameter the HE_{11} mode of the un-tapered fiber starts being guided more strongly by the cladding-air interface than by the core-cladding interface. This happens when the effective index of refraction ($n_{eff} = \beta/k_0$) of the core-clad guided mode reaches the value of the index of refraction of the cladding. For values of n_{eff} higher than the index of refraction of the cladding n_2 the mode is guided by the core-cladding interface whereas for values of n_{eff} lower than n_2 the mode is guided by the cladding-air interface.

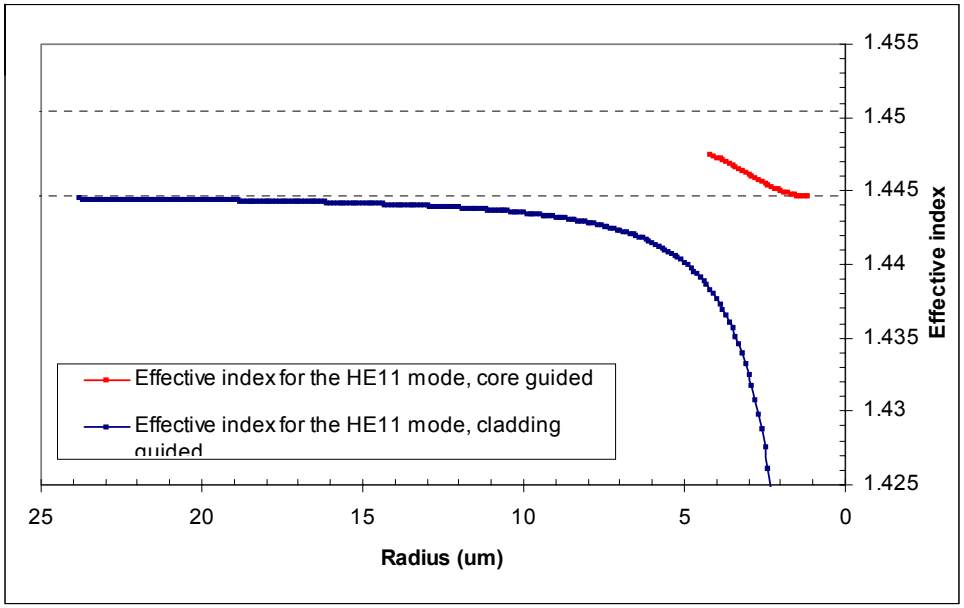

Figure I.6 Plot of the HE_{11} mode, core-guided (red curve) and cladding guided (blue curve). At a core radius of 1.6 μm that corresponds to a cladding radius of 23.8 μm the HE_{11} mode starts being guided by the cladding-air interface. The two horizontal lines indicate the index of refraction of the core (1.4505) and of the cladding (1.4447). The horizontal axis represents the radius of the core for the red curve and the radius of the cladding for the blue curve.

Once the fundamental mode starts being guided by the cladding-air interface, the waveguide is now multimode and the difference between the propagation constant of the fundamental mode and the next mode with the same symmetry is at its minimum

(Figure I.7). This is because of the large diameter of the waveguide at that point and the higher index contrast at its boundary. This means that the angle of the taper at the transition point from core-guidance to cladding-guidance has to be small enough both to accommodate the new boundary conditions and to prevent mode coupling between the fundamental mode (HE_{11}) and the next available mode with similar symmetry (HE_{12}).

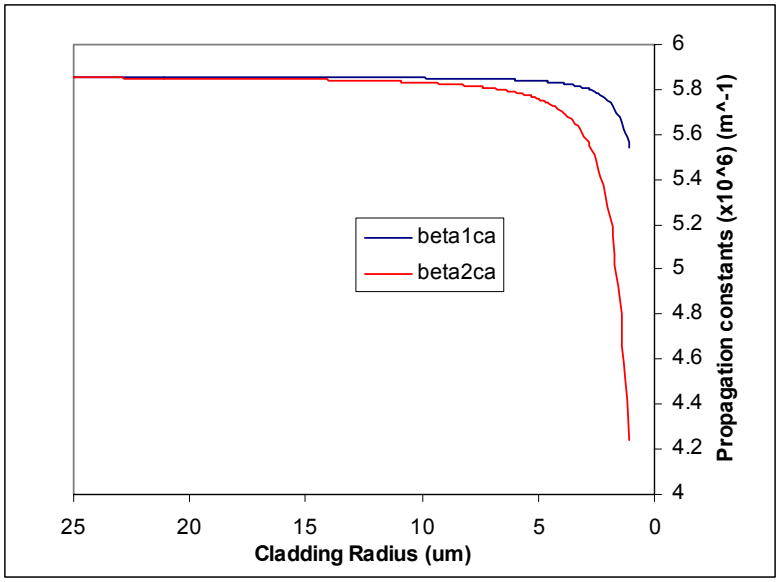

Figure I.7 Plot of the HE_{11} (blue curve) and HE_{12} (red curve) mode propagation constants for the cladding-air guided part of the taper as a function of the cladding radius. The separation between propagation constants increases as the taper radius is decreased.

The difference between the HE_{11} and the HE_{12} propagation constants versus the cladding radius a can be calculated for the entire range of diameters during the tapering. For the region where the guidance is mainly due to the core-cladding interface and all the higher order modes are cutoff, the propagation constant for the HE_{12} mode is calculated simply as $k_0 n_2$.

Optimal Tapering

A useful measurement in investigating the condition for adiabatic tapering is the local taper angle defined as the angle Ω between the fiber axis and the tangent to the taper profile at the point of interest. The tangents to the taper profile form a cone whose height can be approximated as:

$$z_t \approx a / \Omega \tag{I.7}$$

where a is the radius of the taper at that particular point.

The coupling length between the two modes is then taken to be the beat length between the fundamental and the next available mode:

$$z_b = \frac{2\pi}{\beta_1 - \beta_2} \tag{I.8}$$

Having defined the transition length z_t and the beat length z_b between the fundamental mode and HE_{12}, the delineation between lossy and adiabatic tapers can be drawn at $z_t = z_b$. For $z_t >> z_b$ the taper can be considered adiabatic whereas for $z_t << z_b$ there will be a significant loss due to coupling to the second mode. The delineation between lossy and adiabatic tapers is then written:

$$\Omega = \frac{a(\beta_1 - \beta_2)}{2\pi} \tag{I.9}$$

The value of the waveguide radius a is taken to be the radius of the core for the core-guided mode and respectively the radius of the cladding for the cladding guided modes. For core-guided propagation β_1 is the propagation constant of the HE_{11} mode and β_2 is the propagation constant of a hypothetical HE_{12} mode having the effective index of

refraction $n_{eff} = n_2$, the index of refraction of the cladding. For the case of the cladding-guided propagation β_1 and β_2 are the propagation constants of the HE_{11} and HE_{12} modes respectively. To facilitate the comparison with an actual taper, the cladding angle Ω_{cl} is plotted in Fig. I.8. For cladding guidance, Ω_{cl} is given by Eq. (I.9), and for core guidance, Ω_{cl} is Eq. (I.9) multiplied by the ratio of cladding radius to core radius.

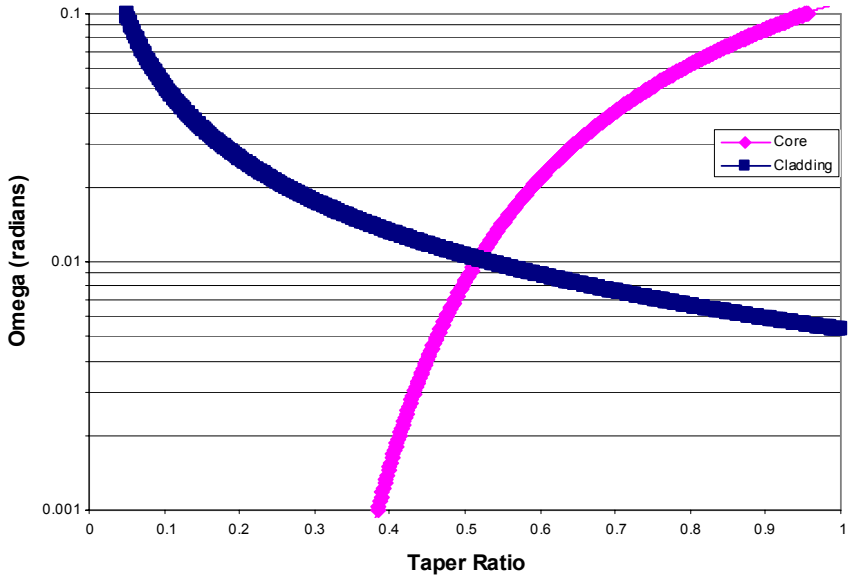

Figure I.8 Plot of the cladding taper angle Ω_{cl} as a function of the taper ratio a/a_0. (a_0 is the un-tapered radius of the fiber.) The pink curve represents the variation of Ω for the core-guiding part of the taper while the blue curve is for the cladding-guiding part. The curve crossing marks the radius of the taper around which the transition from core-guidance to cladding-guidance occurs. The values are calculated for Corning SMF-28 fiber and a wavelength of 1550 nm.

It can be seen that in order to obtain an adiabatic taper the values of the taper angle have to be always below the upper parts of the curves in Figure I.8. The next task is to obtain the taper profile for which the taper angle is close to the maximum admissible value. That will bring the length of the taper to a minimum.

The desired shape of the taper that has the shortest length while still being adiabatic is typically accomplished with an apparatus similar to the one drawn in Figure I.5 for which the distance over which the flame "brushes" the stripped fiber can be varied. Also, for a better control of the size of the heated area of the fiber, a CO_2 laser can be used instead of a hydrogen torch [63]. The only drawback of the CO_2 laser is the requirement of quite precise alignment so that the fiber is heated uniformly as it is scanned by the focused beam.

The function describing the variation of the heated length can be found either by following the so-called "reverse problem" in [62] or by investigation. The problem with the procedure described in [62] is that it involves extremely intensive numerical calculations making it impossible to obtain an analytical form for $L(x)$, the heated length as a function of the taper extension x, which is the sum of the distances traveled by stages A and B in Fig. I.5. The method that is proposed significantly decreases the amount of computation while still resulting in nearly optimal single-mode tapers. It is based solely on the investigation of the delineation curve given in Figure I.8. It can be seen that around the transition region the value of Ω cannot exceed 10^{-2}. It is also preferable that around this region the variation of Ω is minimal in order to accommodate the transition from the core-guided to cladding-guided wave. It is also known that the taper is more "gentle" for larger heated areas or flame-brush lengths. This can be deduced from imposing a conservation law for the mass of fused silica contained in the heated area. Finally, the heated area cannot be smaller than 2 mm for a system based on a traveling burner as illustrated in Figure I.5 simply because the flame itself has a certain width (~2

mm for a torch tip # 3, jewelers standard). Thus, $L(x)$ should resemble a function of the form

$$L(x) = c_1 x^2 + c_2 x + c_3 \tag{I.10}$$

with negative c_1 so that it has a maximum where the transition from core- to cladding-guidance occurs followed by a constant value (set at 2 mm) for the case of a typical burner (see Figure I.9).

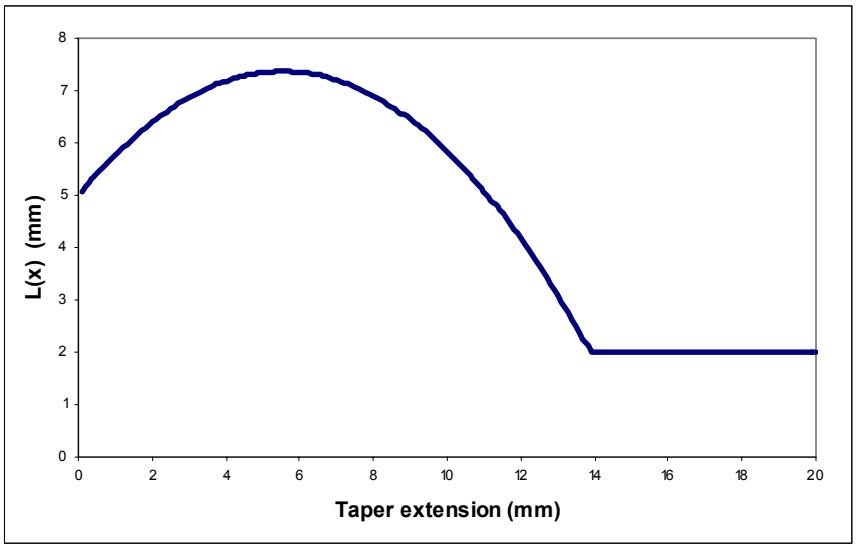

Figure I.9 Suggested profile for $L(x)$.

For the fiber chosen in this calculation (Corning SMF28), and for the operating wavelength of 1550 nm the coefficients in $L(x)$ are: c_1 = -0.0768311 mm^{-1}, c_2 = 0.852467 and c_3 = 5 mm. This results in the fiber profile plotted in Figure I.10.

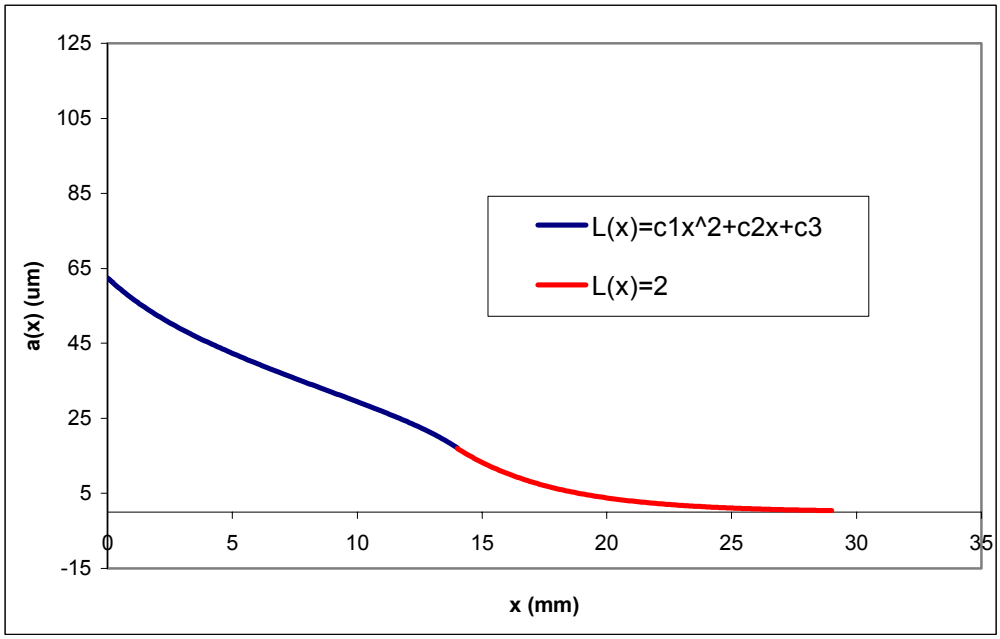

Figure I.10 The cladding radius as a function of the suggested $L(x)$ profile. The blue part of the curve corresponds to $L(x) = c_1x^2+c_2x+c_3$ and the red part is an exponential decay in radius due to the constant $L(x)$.

Using the above $L(x)$ the total length of the bi-conical taper with a waist of 2 μm in diameter can be less than 2.5 cm. Previous single-mode bi-conical tapers prepared with a fixed heated length of 6.5 mm had a length of more than 5 cm. Also since the form of $L(x)$ is rather simple it can be easily implemented in the *LabView* code that controls the fiber puller.

The local taper angle is plotted in Figure I.11. In Figure I.12 the taper angle is plotted together with the adiabaticity delineation curves in Figure I.8. It can be seen that the taper angle remains below the delineation curves for adiabaticity.

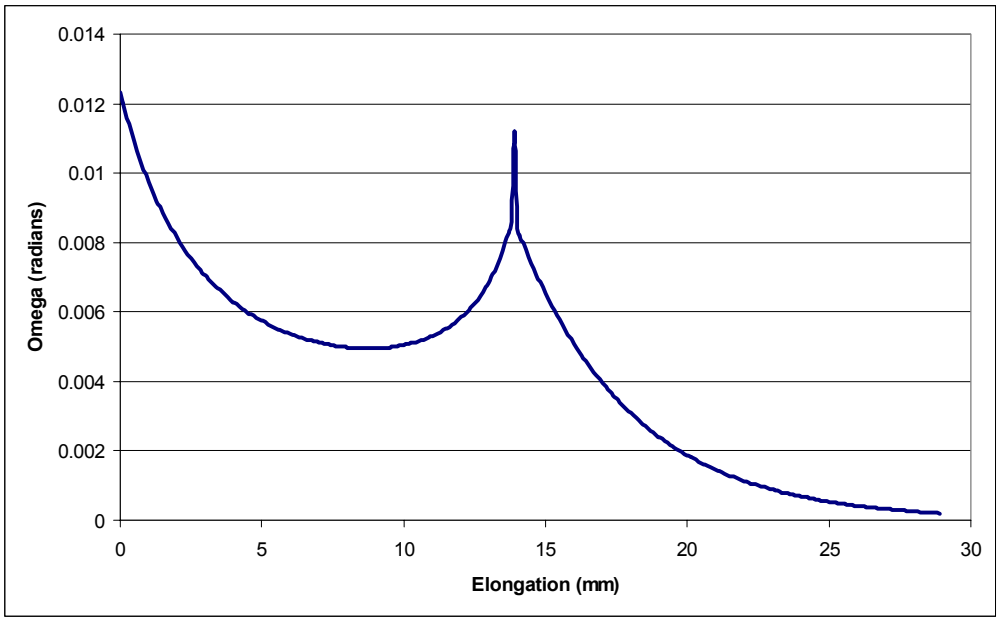

Figure I.11 The taper angle, Ω_{cl} as a function of the taper extension *x*.

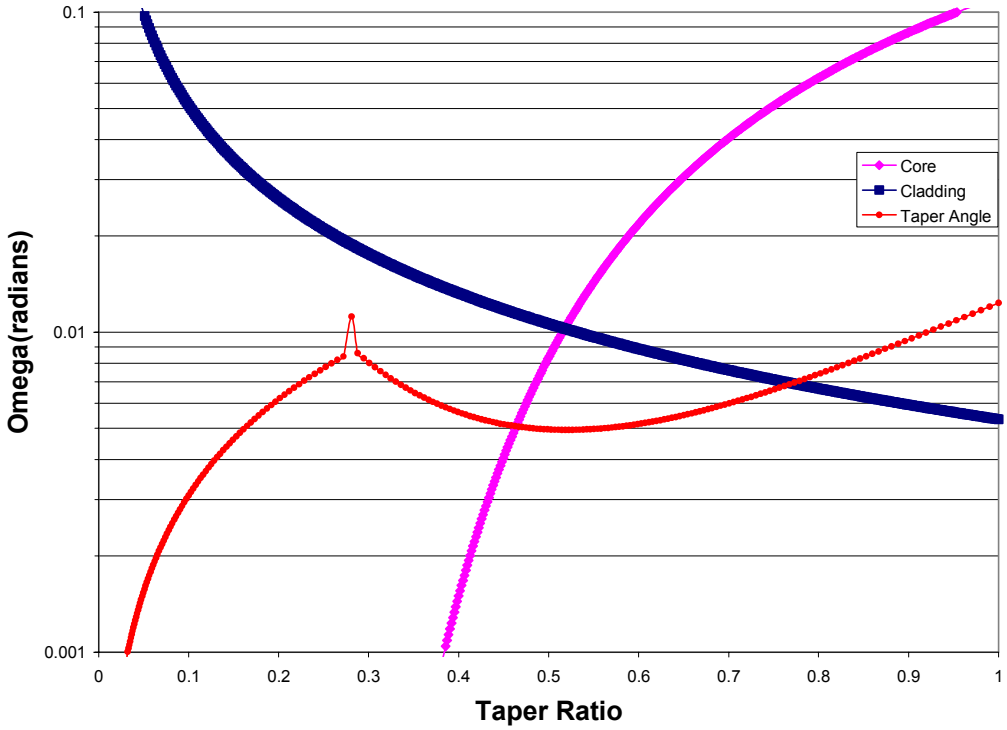

Figure I.12 The taper angle of the optimal profile against the adiabaticity delineation curve. The red curve represents the angle of the profile depicted in Figure I.10.

CHAPTER II

THEORETICAL ASPECTS

1. Whispering-gallery mode equations

The WGM fields of a microresonator, be it a microsphere or a cylinder, can be described using electromagnetic theory in spherical and cylindrical coordinates respectively, plus the proper dielectric boundary conditions. Figure II.1 illustrates the coordinate system used. Also, the figure depicts the two orthogonal polarizations for the electromagnetic field inside the resonators. For the microsphere case the polarization

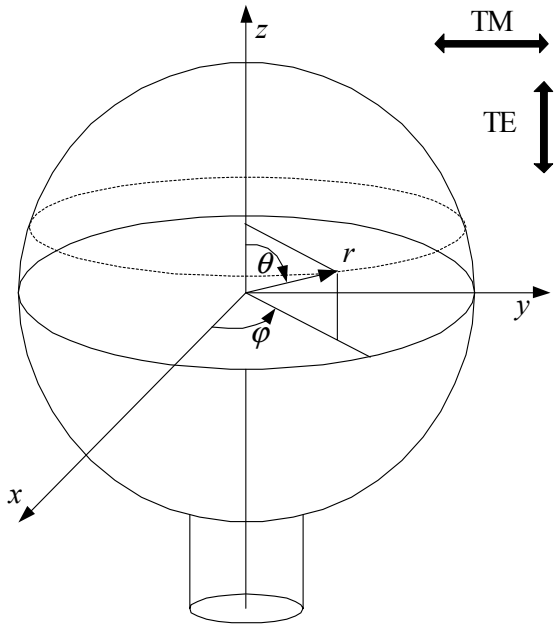

Figure II.1. Microsphere and the associated spherical coordinate system. The arrows indicate the approximate orientation of the electric field at the point where the y-axis intersects the sphere for the TE and TM polarizations.

direction for Transverse Electric (TE) and Transverse Magnetic (TM) is the obvious choice given that WGMs propagate in the φ direction at the equator of the sphere of radius a.

For the spherical case the solutions to Maxwell's equations for the internal ($r < a$) electric and magnetic field components are given in SI units by [64] for the two polarizations:

For the TE case the electric field components are

$$\begin{aligned} E_r(r,\theta,\phi,t) &= 0 \\ E_\theta(r,\theta,\phi,t) &= -E_0 \frac{im}{\sin\theta} \mathrm{P}_\ell^m(\cos\theta)\, j_\ell(k_{q\ell m}^{TE} r) e^{im\phi} e^{-i\omega_{qlm}^{TE} t} \\ E_\phi(r,\theta,\phi,t) &= E_0 \frac{\partial \mathrm{P}_\ell^m(\cos\theta)}{\partial\theta} j_\ell(k_{q\ell m}^{TE} r) e^{im\phi} e^{-i\omega_{qlm}^{TE} t} \end{aligned} \tag{II.1}$$

and the magnetic field components are described by

$$\begin{aligned} H_r(r,\theta,\phi,t) &= -E_0 \frac{\ell(\ell+1)}{i\omega_{qlm}^{TE}\mu_s} \mathrm{P}_\ell^m(\cos\theta) \frac{1}{r} j_\ell(k_{q\ell m}^{TE} r) e^{im\phi} e^{-i\omega_{qlm}^{TE} t} \\ H_\theta(r,\theta,\phi,t) &= -E_0 \frac{1}{i\omega_{qlm}^{TE}\mu_s} \frac{\partial \mathrm{P}_\ell^m(\cos\theta)}{\partial\theta} \frac{1}{r} [k_{q\ell m}^{TE} r j_l(k_{q\ell m}^{TE} r)]' e^{im\phi} e^{-i\omega_{qlm}^{TE} t} \\ H_\phi(r,\theta,\phi,t) &= -E_0 \frac{m}{\omega_{qlm}^{TE}\mu_s} \frac{\mathrm{P}_\ell^m(\cos\theta)}{\sin\theta} \frac{1}{r} [k_{q\ell m}^{TE} r j_\ell(k_{q\ell m}^{TE} r)]' e^{im\phi} e^{-i\omega_{qlm}^{TE} t} \end{aligned} \tag{II.2}$$

For the TM polarization case the electric field is given by

$$\begin{aligned} E_r(r,\theta,\phi,t) &= -E_0 \ell(\ell+1) \mathrm{P}_\ell^m(\cos\theta) \frac{j_\ell(k_{q\ell m}^{TM} r)}{k_{q\ell m}^{TM} r} e^{im\phi} e^{-i\omega_{qlm}^{TM} t} \\ E_\theta(r,\theta,\phi,t) &= -E_0 \frac{\partial \mathrm{P}_\ell^m(\cos\theta)}{\partial\theta} \frac{1}{k_{q\ell m}^{TM} r} [k_{q\ell m}^{TM} r j_\ell(k_{q\ell m}^{TM} r)]' e^{im\phi} e^{-i\omega_{qlm}^{TM} t} \\ E_\phi(r,\theta,\phi,t) &= -E_0 \frac{im\mathrm{P}_\ell^m(\cos\theta)}{\sin\theta} \frac{1}{k_{q\ell m}^{TM} r} [k_{q\ell m}^{TM} r j_\ell(k_{q\ell m}^{TM} r)]' e^{im\phi} e^{-i\omega_{qlm}^{TM} t} \end{aligned} \tag{II.3}$$

whereas the magnetic field components are described by

$$
\begin{aligned}
H_r(r,\theta,\phi,t) &= 0 \\
H_\theta(r,\theta,\phi,t) &= -E_0 \frac{k_{q\ell m}^{TM}}{\omega_{qlm}^{TM}\mu_s} \frac{m\mathrm{P}_\ell^m(\cos\theta)}{\sin\theta} j_\ell(k_{q\ell m}^{TM} r) e^{im\phi} e^{-i\omega_{qlm}^{TM} t} \\
H_\phi(r,\theta,\phi,t) &= E_0 \frac{k_{q\ell m}^{TM}}{i\omega_{qlm}^{TM}\mu_s} \frac{\partial \mathrm{P}_\ell^m(\cos\theta)}{\partial\theta} j_\ell(k_{q\ell m}^{TM} r) e^{im\phi} e^{-i\omega_{qlm}^{TM} t}
\end{aligned}
\tag{II.4}
$$

where E_0 is the electric field amplitude, the P_ℓ^m are the associated Legendre polynomials, j_ℓ are the spherical Bessel functions of the first kind, $k_{q\ell m}^{TE(M)} = n_s \omega_{q\ell m}^{TE(M)} / c$, μ_s is the permeability of the microsphere, n_s is the microsphere's refractive index, $\omega_{qlm}^{TE(M)}$ is the resonance angular frequency for the TE and TM modes respectively, and the prime denotes the derivative with respect to the argument $k_{q\ell m}^{TE(M)} r$.

In the region outside the microsphere ($r > a$) the field components are:

For the TE case the outside electric field components are

$$
\begin{aligned}
E_r(r,\theta,\phi,t) &= 0 \\
E_\theta(r,\theta,\phi,t) &= -E_0 \frac{im}{\sin\theta} \mathrm{P}_\ell^m(\cos\theta) h_\ell^{(1)}(K_{q\ell m}^{TE} r) e^{im\phi} e^{-i\omega_{qlm}^{TE} t} \\
E_\phi(r,\theta,\phi,t) &= E_0 \frac{\partial \mathrm{P}_\ell^m(\cos\theta)}{\partial\theta} h_\ell^{(1)}(K_{q\ell m}^{TE} r) e^{im\phi} e^{-i\omega_{qlm}^{TE} t}
\end{aligned}
\tag{II.5}
$$

and the magnetic field components are described by

$$
\begin{aligned}
H_r(r,\theta,\phi,t) &= -E_0 \frac{\ell(\ell+1)}{i\omega_{qlm}^{TE}\mu_a} \mathrm{P}_\ell^m(\cos\theta) \frac{1}{r} h_\ell^{(1)}(K_{q\ell m}^{TE} r) e^{im\phi} e^{-i\omega_{qlm}^{TE} t} \\
H_\theta(r,\theta,\phi,t) &= -E_0 \frac{1}{i\omega_{qlm}^{TE}\mu_a} \frac{\partial \mathrm{P}_\ell^m(\cos\theta)}{\partial\theta} \frac{1}{r} [K_{q\ell m}^{TE} r h_\ell^{(1)}(K_{q\ell m}^{TE} r)]' e^{im\phi} e^{-i\omega_{qlm}^{TE} t} \\
H_\phi(r,\theta,\phi,t) &= -E_0 \frac{m}{\omega_{qlm}^{TE}\mu_a} \frac{\mathrm{P}_\ell^m(\cos\theta)}{\sin\theta} \frac{1}{r} [K_{q\ell m}^{TE} r h_\ell^{(1)}(K_{q\ell m}^{TE} r)]' e^{im\phi} e^{-i\omega_{qlm}^{TE} t}
\end{aligned}
\tag{II.6}
$$

For the TM polarization case the electric field is given by

$$E_r(r,\theta,\phi,t) = -E_0\ell(\ell+1)\mathrm{P}_\ell^m(\cos\theta)\frac{h_\ell^{(1)}(K_{q\ell m}^{TM}r)}{K_{q\ell m}^{TM}r}e^{im\phi}e^{-i\omega_{q\ell m}^{TM}t}$$

$$E_\theta(r,\theta,\phi,t) = -E_0\frac{\partial\mathrm{P}_\ell^m(\cos\theta)}{\partial\theta}\frac{1}{K_{q\ell m}^{TM}r}[K_{q\ell m}^{TM}rh_\ell^{(1)}(K_{q\ell m}^{TM}r)]'e^{im\phi}e^{-i\omega_{q\ell m}^{TM}t} \qquad \text{(II.7)}$$

$$E_\phi(r,\theta,\phi,t) = -E_0\frac{im\mathrm{P}_\ell^m(\cos\theta)}{\sin\theta}\frac{1}{K_{q\ell m}^{TM}r}[K_{q\ell m}^{TM}rh_\ell^{(1)}(K_{q\ell m}^{TM}r)]'e^{im\phi}e^{-i\omega_{q\ell m}^{TM}t}$$

whereas the magnetic field components for the TM polarization are described by

$$H_r(r,\theta,\phi,t) = 0$$

$$H_\theta(r,\theta,\phi,t) = -E_0\frac{K_{q\ell m}^{TM}}{\omega_{qlm}^{TM}\mu_a}\frac{m\mathrm{P}_\ell^m(\cos\theta)}{\sin\theta}h_\ell^{(1)}(K_{q\ell m}^{TM}r)e^{im\phi}e^{-i\omega_{q\ell m}^{TM}t} \qquad \text{(II.8)}$$

$$H_\phi(r,\theta,\phi,t) = E_0\frac{K_{q\ell m}^{TM}}{i\omega_{qlm}^{TM}\mu_a}\frac{\partial\mathrm{P}_\ell^m(\cos\theta)}{\partial\theta}h_\ell^{(1)}(K_{q\ell m}^{TM}r)e^{im\phi}e^{-i\omega_{q\ell m}^{TM}t}$$

where $h_\ell^{(1)}(K_{q\ell m}^{TE(M)}r)$ are the spherical Hankel functions, $K_{q\ell m}^{TE(M)} = k_{q\ell m}^{TE(M)}/n$, μ_a is the permeability of the outside medium, n_a is the refractive index of the surrounding medium $n = n_s/n_a$, and the prime denotes the derivative with respect to the argument $K_{q\ell m}^{TE(M)}r$.

The WGM resonance frequencies are

$$\nu_{q\ell m}^{TE(M)} = \frac{\omega_{q\ell m}^{TE(M)}}{2\pi} = \delta\left(\ell+1/2+a_q\left(\frac{\ell+1/2}{2}\right)^{1/3} - \Delta^{TE(M)}\boxed{\pm\varepsilon^2\left(\frac{\ell-|m|}{2}\right)} + \frac{3a_q^2}{2^{2/3}10(\ell+1/2)^{1/3}}\right), \qquad \text{(II.9)}$$

in which $\delta = c/2\pi an_s$ is the microsphere's free spectral range, a_q is the q^{th} zero of the Airy function, and $\Delta^{TE} = n/\sqrt{n^2-1}$ and $\Delta^{TM} = \left(n\sqrt{n^2-1}\right)^{-1}$ is the polarization dependent frequency shift. The boxed term accounts for sphere's eccentricity, the upper sign being used for oblate spheres and the lower sign for prolate spheres.

Figures II.2 and II.3 depict the radial and azimuthal microsphere WGM structure. For both cases the TE polarization is presented.

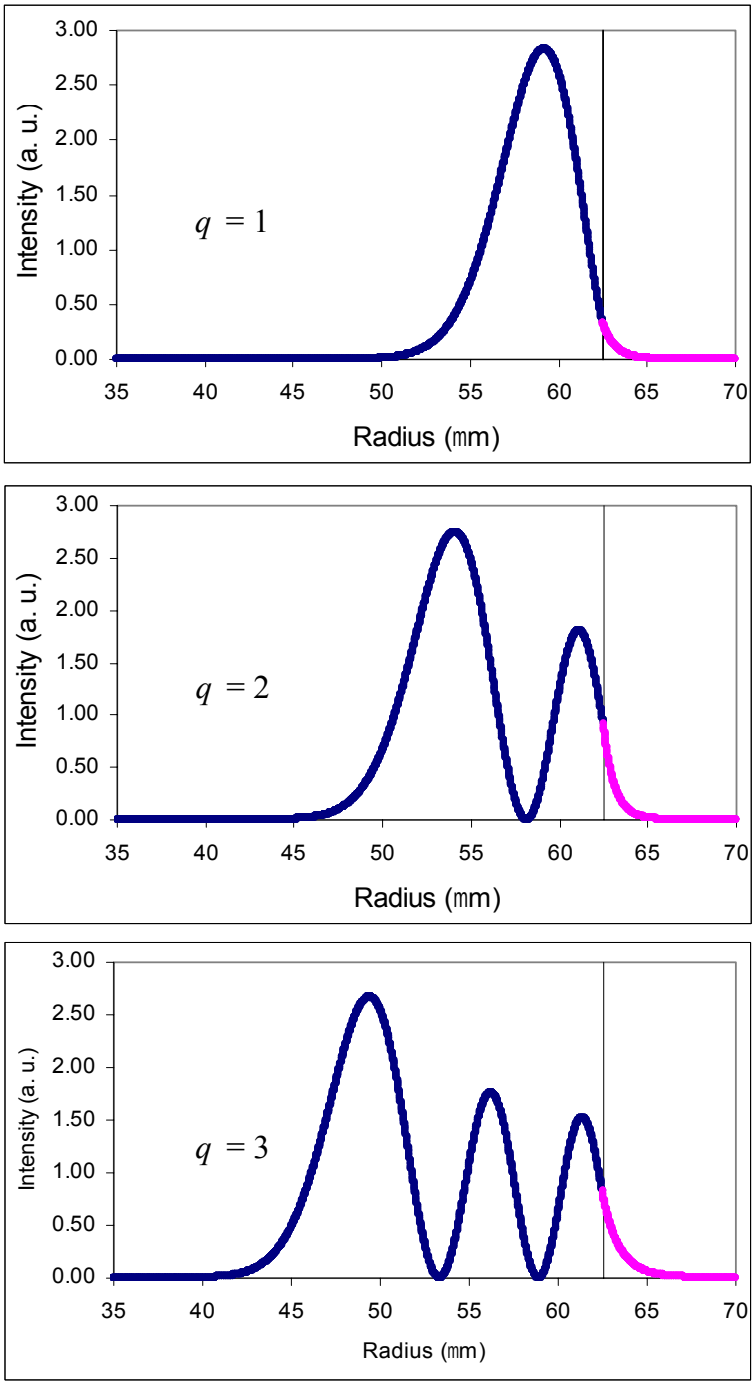

Figure II.2. The first three radial order modes.

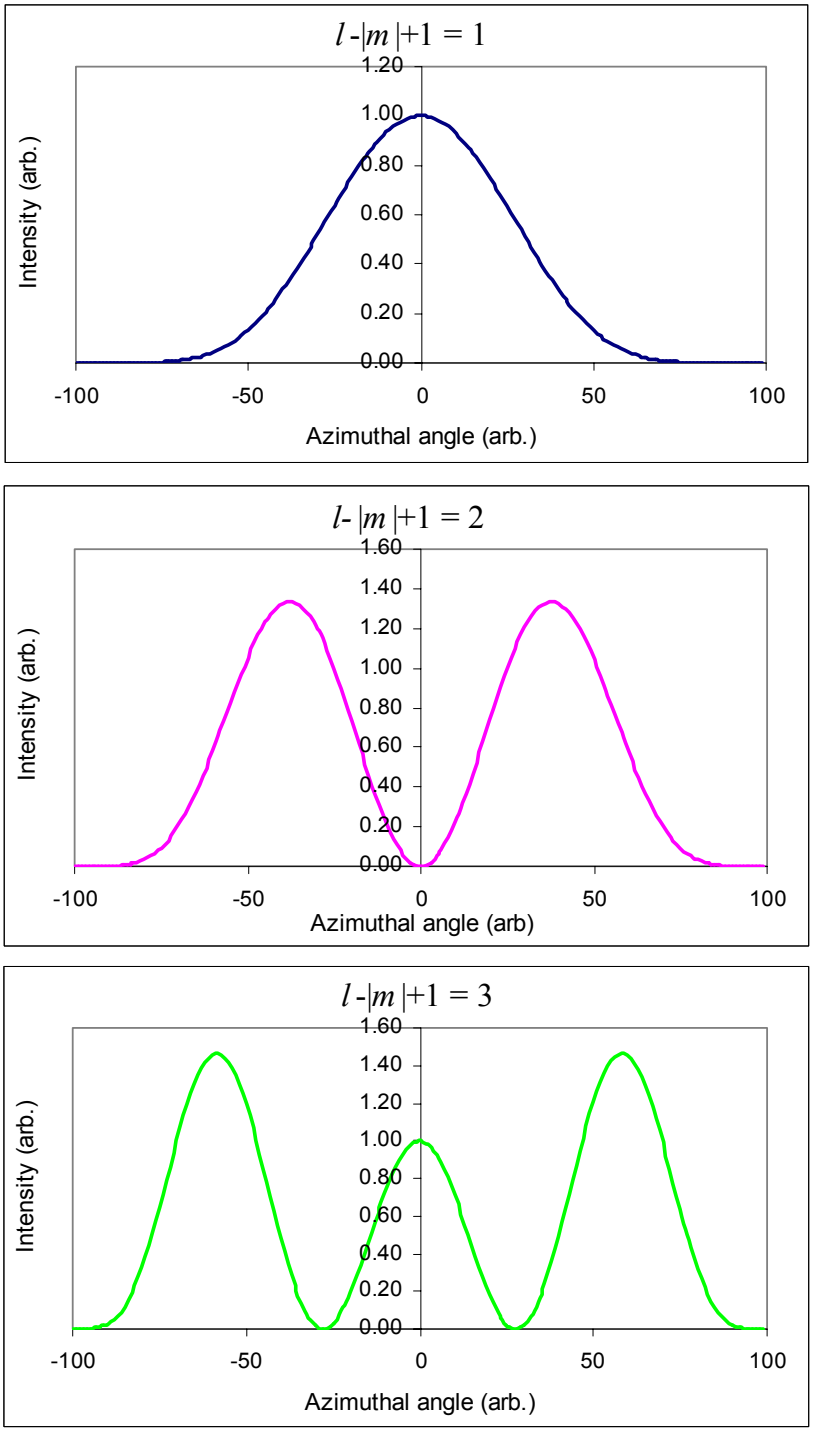

Figure II.3. The first three angular order modes.

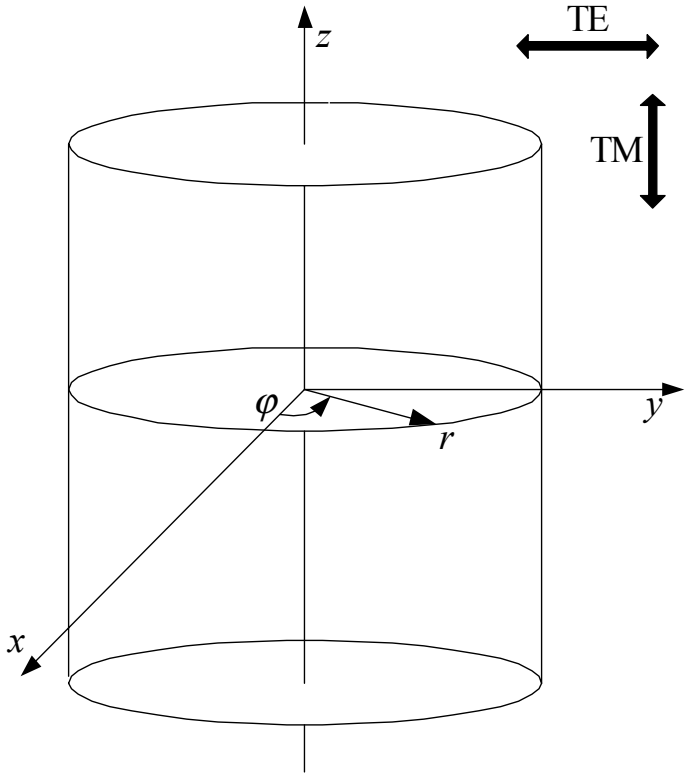

Figure II.4. Microcylinder and the associated cylindrical coordinate system. The arrows indicate the approximate orientation of the electric field at the point where the *y*-axis intersects the cylinder for the TE and TM polarizations.

In the case of a cylindrical microresonator of radius a the WGMs propagate around the surface in the φ direction in the y-x plane, and the electric and magnetic field components inside and outside the resonator can be expressed as follows [65]:

The TE polarization field components inside ($r < a$) the microresonator are

$$E_r(r,\phi,z,t) = -H_0 \frac{l\mu_s \omega_{ql}^{TE}}{k_{ql}^{TE2} r} J_l(k_{ql}^{TE} r) e^{il\phi} e^{-i\omega_{ql}^{TE} t}$$

$$E_\varphi(r,\phi,z,t) = -H_0 \frac{i\mu_s \omega_{ql}^{TE}}{k_{ql}^{TE}} J'_l(k_{ql}^{TE} r) e^{il\phi} e^{-i\omega_{ql}^{TE} t} \qquad \text{(II.10)}$$

$$H_z(r,\phi,z,t) = H_0 J_l(k_{ql}^{TE} r) e^{il\phi} e^{-i\omega_{ql}^{TE} t}$$

and outside ($r > a$)

$$E_r(r,\phi,z,t) = -H_0 \frac{l\mu_a \omega_{ql}^{TE}}{k_{ql}^{TE2} r} H_l^{(1)}(k_{ql}^{TE} r) e^{il\phi} e^{-i\omega_{ql}^{TE} t}$$

$$E_\varphi(r,\phi,z,t) = -H_0 \frac{i\mu_a \omega_{ql}^{TE}}{k_{ql}^{TE}} H_l^{(1)}{}'(k_{ql}^{TE} r) e^{il\phi} e^{-i\omega_{ql}^{TE} t} \qquad \text{(II.11)}$$

$$H_z(r,\phi,z,t) = H_0 H_l^{(1)}(k_{ql}^{TE} r) e^{il\phi} e^{-i\omega_{ql}^{TE} t}$$

The TM polarization field components inside ($r < a$) the microresonator are

$$H_r(r,\phi,z,t) = E_0 \frac{l}{\mu_s \omega_{ql}^{TM} r} J_l(k_{ql}^{TM} r) e^{il\phi} e^{-i\omega_{ql}^{TM} t}$$

$$H_\varphi(r,\phi,z,t) = E_0 \frac{ik_{ql}^{TM}}{\mu_s \omega_{ql}^{TM}} J_l{}'(k_{ql}^{TM} r) e^{il\phi} e^{-i\omega_{ql}^{TM} t} \qquad \text{(II.12)}$$

$$E_z(r,\phi,z,t) = E_0 J_l(k_{ql}^{TM} r) e^{il\phi} e^{-i\omega_{ql}^{TM} t}$$

and outside ($r > a$)

$$H_r(r,\phi,z,t) = E_0 \frac{l}{\mu_a \omega_{ql}^{TM} r} H_l^{(1)}(k_{ql}^{TM} r) e^{il\phi} e^{-i\omega_{ql}^{TM} t}$$

$$H_\varphi(r,\phi,z,t) = E_0 \frac{ik_{ql}^{TM}}{\mu_a \omega} H_l^{(1)}{}'(k_{ql}^{TM} r) e^{il\phi} e^{-i\omega_{ql}^{TM} t} \qquad \text{(II.13)}$$

$$E_z(r,\phi,z,t) = E_0 H_l^{(1)}(k_{ql}^{TM} r) e^{il\phi} e^{-i\omega_{ql}^{TM} t}$$

where

$$l = \frac{2\pi n_{eff}}{\lambda}. \qquad \text{(II.14)}$$

The resonance frequencies are given by

$$\nu_{q\ell}^{TE(M)} = \frac{\omega_{q\ell}^{TE(M)}}{2\pi} = \delta\left(\ell + a_q \left(\frac{\ell}{2} \right)^{1/3} - \Delta^{TE(M)} + \frac{3a_q^2}{2^{2/3} 10 \ell^{1/3}} \right), \qquad \text{(II.15)}$$

and are similar to the spherical case, the differences being that $\ell + 1/2$ becomes ℓ as a result of using cylindrical rather than spherical Bessel functions, and no m degeneracy.

2. Ring cavity model

Although describing in a precise manner the WGM modes inside a spherical or cylindrical microcavity, the exact model proves to be very difficult to use and it consumes vast computational resources. Combining this exact description of WGMs with the exact description of fiber modes, as given in Chapter I, for the analysis of fiber-microresonator coupling and frequency response is impractical. The detail is not needed for an understanding of microresonator behavior.

As a result, a more simplified model was developed [66]. It is based on a 4-mirror ring cavity in which one of the mirrors is a partially transmitting mirror while all the others are assumed to be perfectly reflective. A round-trip intensity loss αl is assumed; it models the intrinsic loss of a WGM microresonator. The transmission coefficient T of the partially transmitting mirror will take the role of the square of the coupling coefficient between the microresonator and the tapered fiber. Figure II.5 a) depicts a typical experimental setup with a microresonator in contact with a tapered fiber while Figure II.5 b) shows the analogous 4-mirror ring cavity.

The ring cavity model is a valid analog to a fiber-coupled microresonator when only a single fiber mode is excited. For light incident on a microresonator this is accomplished by making the fiber taper adiabatic, as described in Chapter I. However, light coupling out of the microresonator can couple into many fiber modes, and any light coupled into modes other than HE_{11} will be lost if the second taper transition is also adiabatic. Fortunately, it is possible to make this lossy coupling into higher-order fiber modes negligibly small by properly choosing the diameter of the tapered fiber [60]. Thus the ring cavity model can be applied.

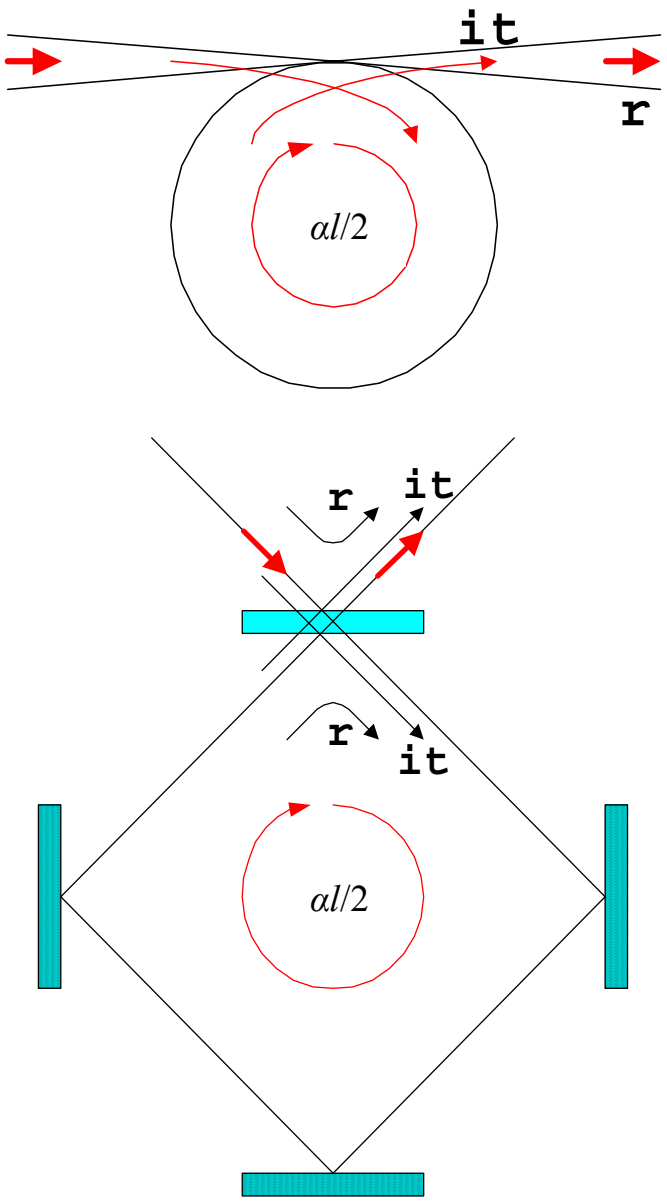

Figure II.5. 4-Mirror ring cavity model. a) Microcavity and tapered fiber in contact. Light can couple from the fiber into the resonator and vice versa. b) The 4-mirror ring cavity equivalent. The top mirror is partially transmitting; all others have 100% reflectivity.

The electric field reflected from the top mirror of the ring cavity, relative to the incident field, can be expressed as

$$\frac{E_r}{E_i} = r - t^2 e^{-\frac{\alpha l}{2}} e^{i\delta}\left[1 + re^{-\frac{\alpha l}{2}} e^{i\delta} + (re^{-\frac{\alpha l}{2}} e^{i\delta})^2 + \ldots\right], \tag{II.16}$$

where E_r is the reflected electric field, E_i is the incident electric field; r is the reflection coefficient and Åt is the transmission coefficient of the top mirror. δ is the phase detuning and αl is the round-trip loss. This can be rewritten as

$$\frac{E_r}{E_i} = r - \frac{t^2 e^{-\frac{\alpha l}{2}} e^{i\delta}}{1 - re^{-\frac{\alpha l}{2}} e^{i\delta}} = \frac{r - e^{-\frac{\alpha l}{2}} e^{i\delta}}{1 - re^{-\frac{\alpha l}{2}} e^{i\delta}}. \tag{II.17}$$

Assuming that both the round-trip loss αl and the transmittance $T = t^2$ are << 1, Eq. (II.17) takes the form

$$\frac{E_r}{E_i} = \frac{r - 1 + \frac{\alpha l}{2} - i\delta}{1 - r + \frac{\alpha l}{2} - i\delta} = \frac{\frac{-T + \alpha l}{2} - i\delta}{\frac{T + \alpha l}{2} - i\delta}, \tag{II.18}$$

where for a small T

$$T = t^2 = 1 - r^2 \cong 2(1 - r). \tag{II.19}$$

Defining x as the loss ratio

$$x = \frac{T}{\alpha l} \tag{II.20}$$

and identifying the cavity detuning in units of resonance half-linewidth

$$\theta \equiv -\frac{2\delta}{(T + \alpha l)}, \tag{II.21}$$

Eq. (II.18) can be expressed as

$$\frac{E_r}{E_i} = \frac{\frac{1-x}{1+x} + i\theta}{1 + i\theta}. \tag{II.22}$$

A detector positioned at the output of the tapered fiber in contact with the microresonator or collecting the light reflected off the ring cavity will measure a signal proportional to the square of the electric field:

$$R = \left|\frac{E_r}{E_i}\right|^2 = \frac{\left(\frac{1-x}{1+x}\right)^2 + \theta^2}{1+\theta^2}. \tag{II.23}$$

The electric field that exits the cavity is out of phase with the field reflected off the input mirror. As the input light is scanned in frequency, a sharp Lorentzian dip (e. g. Fig. III.2) is observed whenever a resonance condition is met (the cavity optical round-trip path is an integer multiple of the wavelength) and a round-trip loss is present. It can be seen in Eq. (II.22) that on resonance ($\theta = 0$), for a value of x = 1 (or $T = \alpha l$) there is 100% extinction in the reflected signal. The Lorentzian WGM dip extends in this case all the way down to zero. Such a regime in which the coupling loss equals the intrinsic loss is called critical coupling. When $T < \alpha l$ the resonator operates in an undercoupled regime while for $T > \alpha l$ the WGM is said to be in the overcoupled regime.

For practical purposes it is also useful to define the dip depth M as

$$M(\theta) = 1 - R = \frac{\frac{4x}{(1+x)^2}}{1+\theta^2} = \frac{M_0}{1+\theta^2}, \tag{II.24}$$

where

$$M_0 = \frac{4x}{(1+x)^2} \tag{II.25}$$

reaches a maximum value of 1 or 100% at critical coupling. Varying the loss ratio x

either by changing T (the coupling loss) or αl (the round trip loss) would result in changes in the WGM dip depth M_0. The variation of the dip depth M_0 with x is illustrated in Figure II.6.

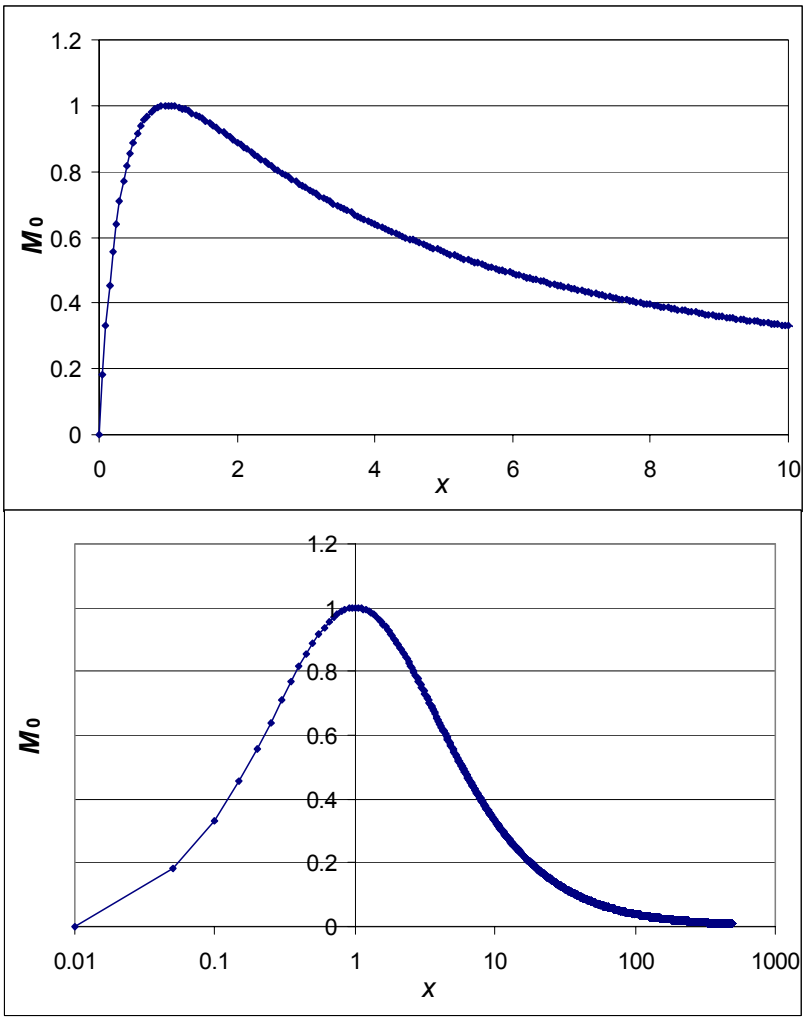

Figure II.6. Top: Dip depth variation with the coupling regime x.
Bottom: Same, but with logarithmic horizontal axis.

It can be seen that the dip depth reaches its maximum value 1 (or 100%) for $x = 1$. Nevertheless, for a dip depth different from 100% there is an ambiguity in determining the coupling regime. For every given dip depth there are two solutions for the coupling

regime: x and $1/x$. In other words both x and $1/x$ result in the same value of the dip depth as given by Eq. (II.25).

The majority of the sensing experiments described in this dissertation take advantage of the dependence of the resonance dip depth variation with the round-trip loss variation in the presence of the analyte. The most general expression for the round trip loss can be written as

$$\alpha l = \alpha_i l + f\alpha_s l + f\alpha_m l\,, \tag{II.26}$$

where α_i is the intrinsic absorption coefficient of the microresonator. It takes into account all the losses of the isolated resonator such as absorption, radiation and scattering. α_s is the absorption coefficient of the solvent containing the analyte in a typical sensing experiment for liquids and α_m is the absorption coefficient of the analyte. The evanescent fraction f accounts for the fact that only 0.3-3.0% of the WGM interacts with the surrounding medium, depending on the WGM's radial mode order number.

The loss ratio x can be rewritten as

$$x = \frac{T}{\alpha_i l + f\alpha_s l + f\alpha_m l}\,, \tag{II.27}$$

and since a given value of M_0 is obtained either for x or for $y = 1/x$, M_0 can be also expressed as

$$M_0 = \frac{4y}{(1+y)^2}\,; \tag{II.28}$$

it follows that

$$\frac{dM_0}{dy} = \frac{4(1-y)}{(1+y)^3} = \left(\frac{1-y}{1+y}\right)\frac{M_0}{y}\,, \tag{II.29}$$

and since, when the concentration of the analyte is varied,

$$dy = \frac{fld\alpha_m}{T}, \tag{II.30}$$

we get

$$\frac{dM_0}{M_0} = \left(\frac{1-y}{1+y}\right)\frac{f}{\alpha_i + f\alpha_s + f\alpha_m}d\alpha_m . \tag{II.31}$$

Equation (II.31) can be now expressed again in terms of x. Also, $f\alpha_m$ is typically much smaller than $\alpha_i + f\alpha_s$ and it can be neglected. Finally,

$$\frac{dM_0}{M_0} = -\underbrace{\left(\frac{1-x}{1+x}\right)\frac{f}{\alpha_i + f\alpha_s}}_{L^t_{eff}}d\alpha_m , \tag{II.32}$$

where L^t_{eff} is the theoretical effective absorption pathlength defined in analogy with Beer's Law (but valid here only in the limit $dM_0 << M_0$):

$$\frac{dI}{I} = -L_{eff}d\alpha . \tag{II.33}$$

In conclusion, the effective absorption pathlength is defined as

$$L^t_{eff} = \left(\frac{1-x}{1+x}\right)\frac{f}{\alpha_i + f\alpha_s}. \tag{II.34}$$

A negative value of L^t_{eff} means that the mode is overcoupled whereas a positive value is obtained for undercoupled WGMs. However, the theoretical effective absorption pathlength is zero for the critically coupled modes making the use such WGMs an inappropriate option for a sensing experiment, since $dM_0 << M_0$ is violated. The fact that the critically coupled modes have zero effective absorption pathlength and consequently zero sensitivity can be also observed in Figure II.6. The slope of the curve representing

the variation of the WGM resonance dip depth with changing x, (or with changing round-trip loss) is zero when x equals 1.

For the gas sensing experiments described in Chapter III the value of α_s is zero and relation (II.34) simplifies to

$$L^t_{eff} = \left(\frac{1-x}{1+x}\right)\frac{f}{\alpha_i}. \tag{II.35}$$

In the liquid sensing experiments, in the case of strong solvent absorption, the value of $f\alpha_s >> \alpha_i + f\alpha_m$ and the theoretical effective absorption pathlength takes the form

$$L^t_{eff} = \left(\frac{1-x}{1+x}\right)\frac{1}{\alpha_s}. \tag{II.36}$$

In the case of moderate solvent absorption coefficient the general expression in Eq. (II.34) is used.

In all cases, when α_m is known and M_0 and $M_0 + \Delta M_0$ are measured, L^t_{eff} can be compared to the experimental absorption pathlength found from

$$L^e_{eff} = \frac{1}{\alpha_m}\ln\frac{M_0}{M_0 + \Delta M_0} \tag{II.37}$$

3. Coupling regime investigation

In the previous section it was observed that for a given WGM dip depth there is an ambiguity in determining the exact coupling regime, each WGM having the possibility to be either undercoupled or overcoupled.

There are experimental means to determine the coupling regime. The coupling constant between the tapered fiber and the microresonator can be changed by moving the tapered fiber closer to or farther away from the microresonator and recording the WGM dip depth change. Moving the tapered fiber away from the microresonator results in a decrease of the coupling constant. If the WGM dip becomes shallower it means that the microresonator is undercoupled. Reducing the coupling constant T will drive the microresonator into an even more undercoupled regime, reducing the strength of the WGM resonance. If the WGM resonance dip becomes deeper it means that the microresonator was initially overcoupled. The decrease in coupling constant results in driving the microresonator more towards the critical coupling regime where the dip depth is maximum.

Another way to investigate the coupling regime is by keeping the coupling strength constant and varying the round-trip loss by bringing an object in close proximity to the surface of the microresonator where the WGM is excited. The object's presence within the evanescent fraction of the microresonator results in an increase in the round-trip loss. If the microresonator was initially overcoupled the WGM resonance dip becomes deeper; an initially undercoupled mode would become shallower.

The two methods described above are not convenient for determining the coupling regime since they require invasive probing of each microresonator produced.

This could constitute a drawback for some applications where large scale integration is used in producing the microresonators and a priori knowledge of each resonator's coupling regime is needed for predicting individual microresonator responses.

A non-invasive method for determining the coupling regime was developed. The microresonator is permanently in contact with the tapered fiber and no loss is added by any artificial means. Instead, the light from the tunable diode laser (TDL) is modulated in a square wave fashion as it scans in frequency over a WGM resonance. Figure II.7 illustrates the experimental setup.

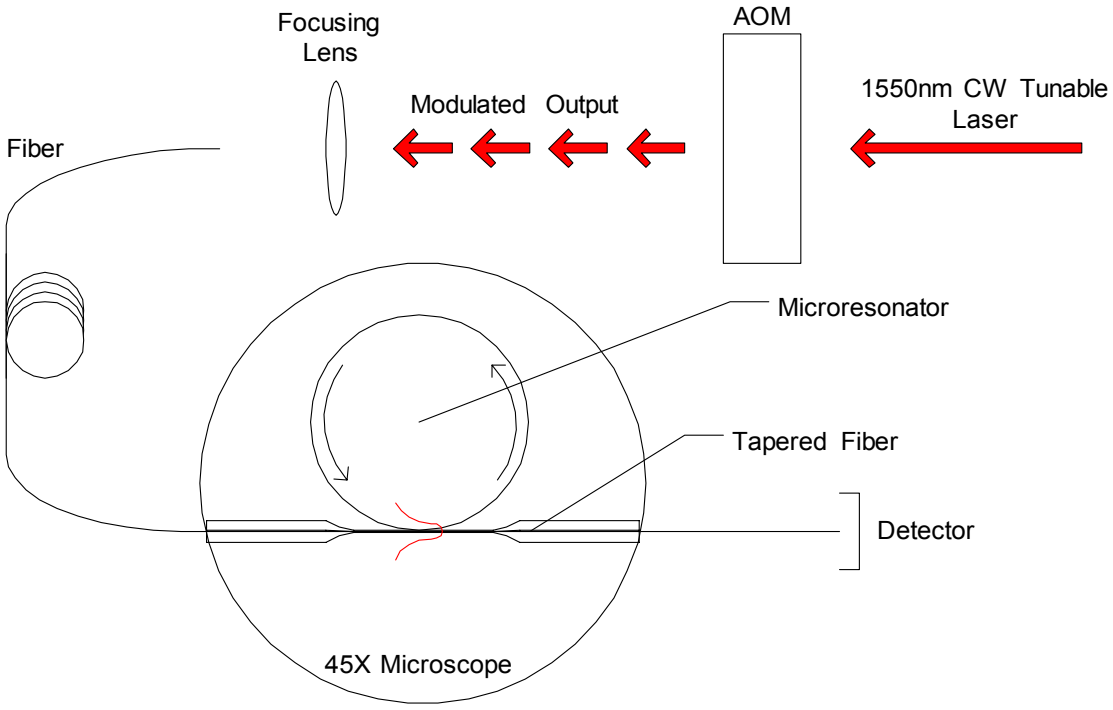

Figure II.7. Experimental setup for coupling regime investigation. Light from the TDL is modulated in a square wave fashion by the Acousto-Optic Modulator (AOM). It is then coupled into single-mode optical fiber, adiabatically tapered. The output at the detector is monitored.

In Figure II.8 the input light modulation versus the bottom of a WGM dip is sketched.

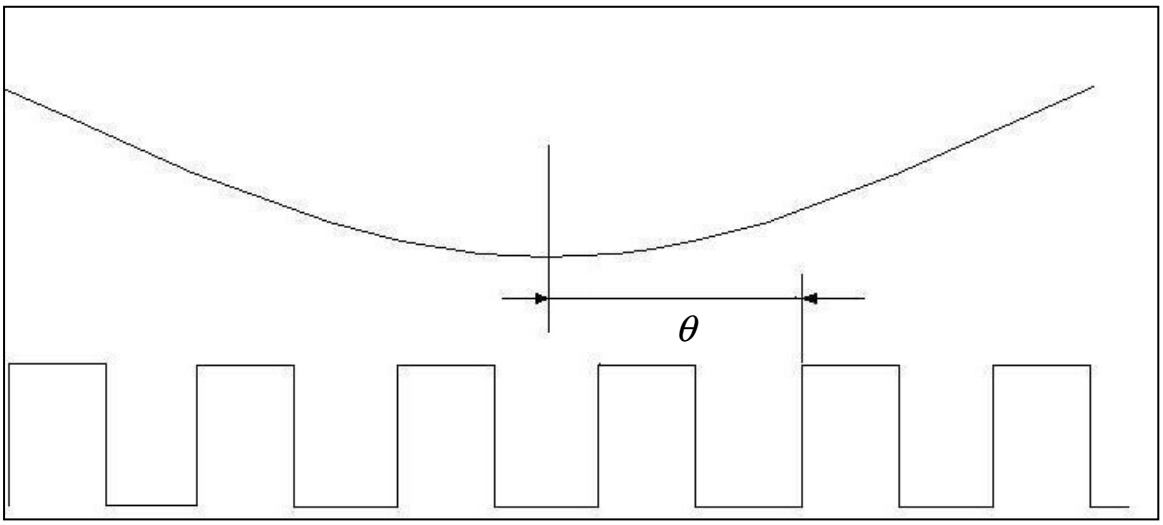

Figure II.8. Sketch of the square wave modulated light from the TDL as it scans in frequency over a WGM dip bottom (not to scale).

Also visible in Figure II.8 is θ, the detuning of a square wave cycle from the WGM resonance in units of WGM half linewidths.

Using the 4-mirror ring cavity model the field reflected off the input mirror for detuned incident light with a time-varying amplitude is found from

$$\frac{dE_r(t)}{dt} = -\frac{dE_i(t)}{dt} - k(1+i\theta)E_r + k[(x-1)/(x+1) - i\theta]E_i, \qquad \text{(II.38)}$$

where k is the field decay rate or WGM half linewidth. All other variables have the same meaning as in section II.2.

Experimental data is in perfect agreement with the resonator response predicted by the theoretical model. Figures II.9, II.10 and II.11 depict the resonator response for undercoupled, overcoupled and critically coupled WGM resonances.

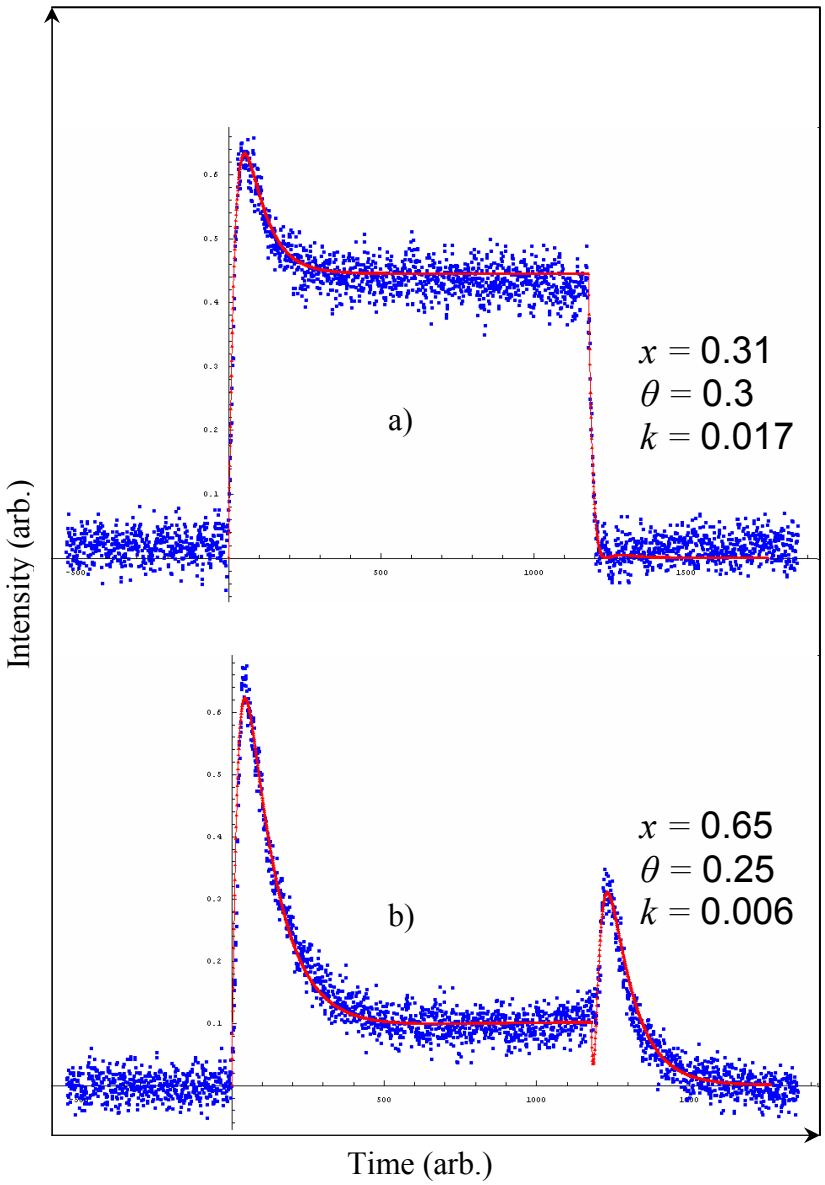

Figure II.9. Undercoupled WGM time response to a square wave amplitude modulated input. Blue dots represent the experimental data; the red line is the theoretical fit using the corresponding fit parameters.
a) $x < 1/3$.
b) $1/3 < x < 1$

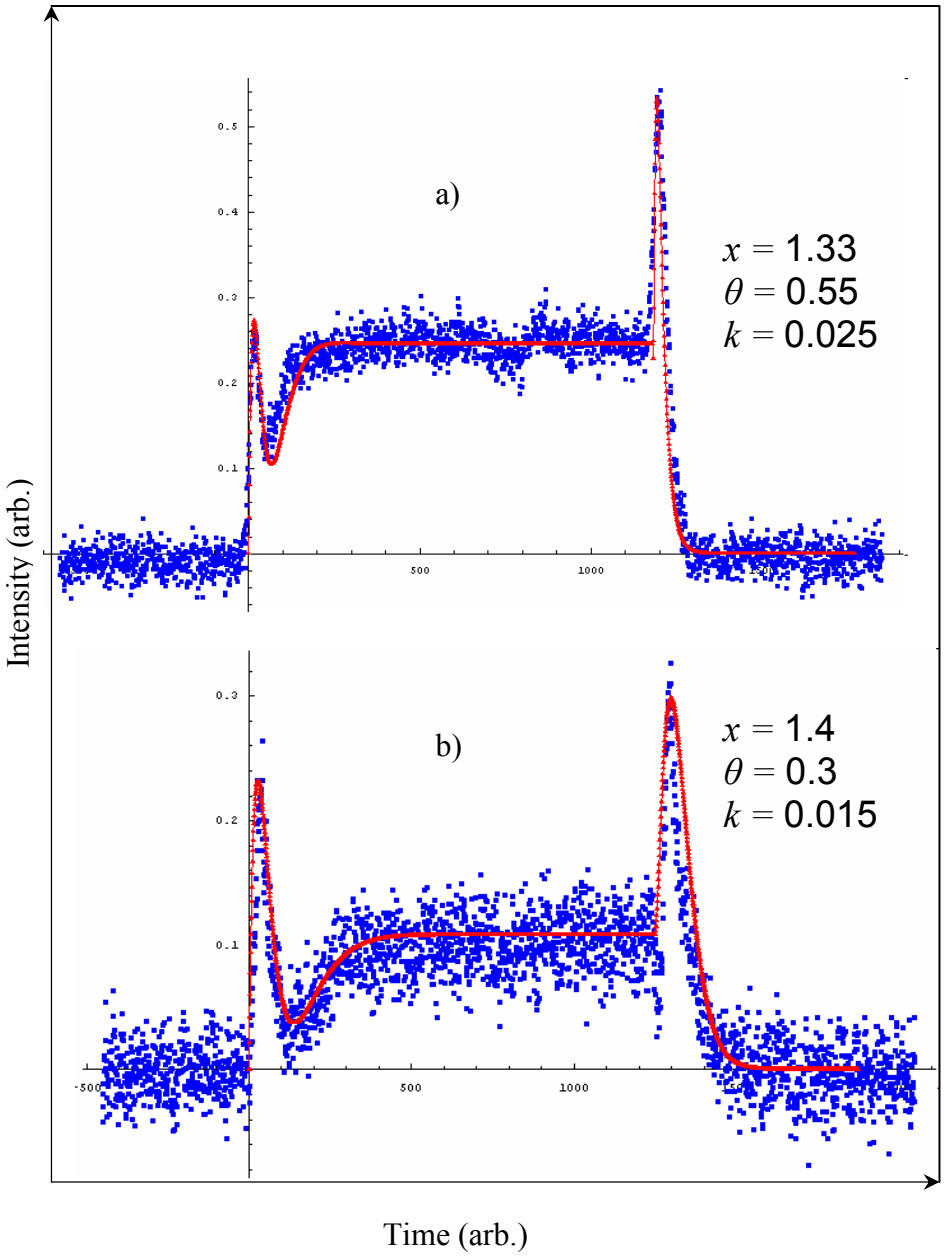

Figure II.10. Overcoupled WGM time response to a square wave amplitude modulated input. Blue dots represent the experimental data; the red line is the theoretical fit using the corresponding fit parameters.
a) More detuned square wave cycle.
b) Less detuned square wave cycle.

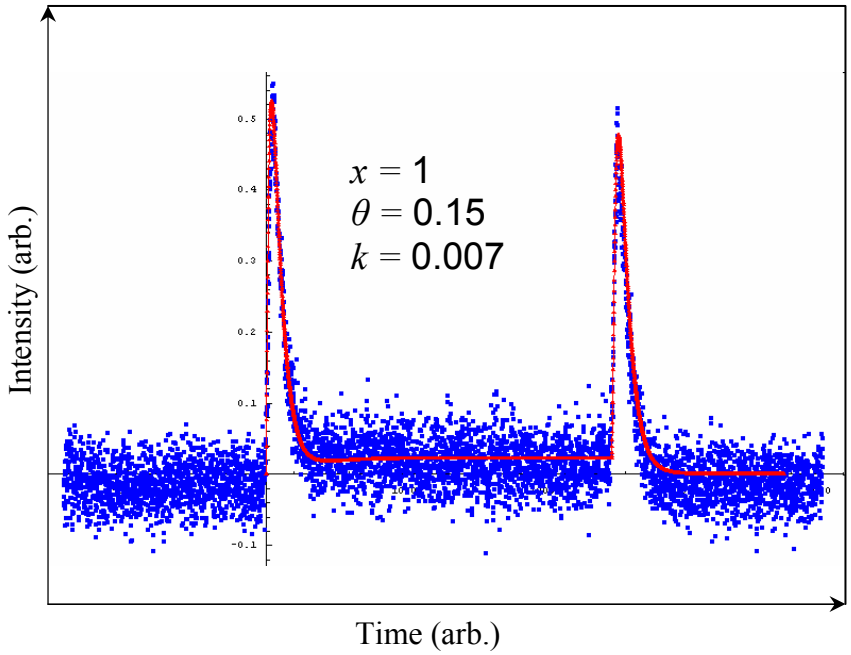

Figure II.11. Critically coupled WGM time response to a square wave amplitude modulated input. Blue dots represent the experimental data; the red line is the theoretical fit using the corresponding fit parameters.

Figures II.9 and II.10 show a qualitative difference between the undercoupled and overcoupled WGM response to the modulated input. For the undercoupled modes, after the initial spike the signal reaches steady state in a monotonic manner. The overcoupled modes have a response that goes through a lower value (zero for $\theta = 0$) before reaching steady state.

In the theoretical fit a 7 ns rise and fall time of the exponential turn on and off of the input square wave signal is used to match the rise and fall time of the function generator that drives the AOM.

CHAPTER III

GAS SENSING

1. Experimental Setup

For gas detection a vacuum chamber has been designed equipped with mechanical, electrical, and fiber optic feedthroughs. Figure III.1 is a schematic of a typical experimental setup.

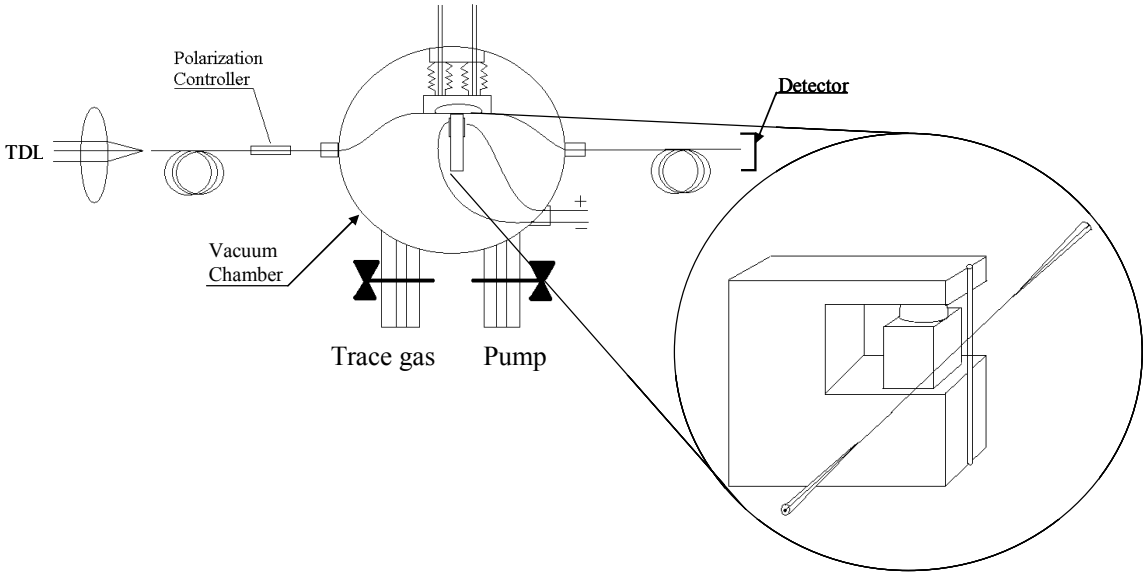

Figure III.1. Gas sensing experimental setup. Laser light from a 1650 nm CW TDL is launched into the optical fiber. After passing through a polarization controller the fiber is fed into the vacuum chamber. The tapered fiber is in contact with the cylindrical microresonator. The fiber exits the chamber and the output is collected onto a detector.

The inset in Figure III.1 depicts the tapered fiber in contact with a vertically mounted cylindrical WGM microcavity. The microcylinder is usually obtained by carefully removing the jacket from a standard optical fiber. A piece of about 15 cm of jacketed fiber is immersed in acetone for up to 20 minutes. The acetone softens the jacket until it falls off the fiber. If the jacket is still attached after 20 minutes it can be easily removed by sliding it off gently. The remaining un-jacketed fiber is then vigorously wiped with lint-free tissue impregnated first with acetone and then with methanol. The fiber is then rinsed with methanol. All these cleaning steps are made to ensure a microresonator surface as clean as possible. Oftentimes the fiber is mounted over a low temperature hydrogen flame that swipes the fiber lengthwise to further clean and possibly smooth the microresonator surface. The hydrogen flame has to be sufficiently cold to ensure that the microresonator does not melt and maintains a perfect cylindrical symmetry.

After successfully cleaning the microcylinder's surface, a 2-cm length is placed across the piezoelectric transducer (PZT) fixture also depicted in Figure III.1 inset. A small drop of Super Glue is then applied over the fiber on both mounting points across the PZT. Before the Super Glue cures a small piece of glass cut from a microscope slide is positioned over the adhesive drop such that the microcylinder is sandwiched between the stretching device arm and the glass piece. This is done to ensure that the microresonator is rigidly attached to the stretching arms.

The PZT used expands 7 μm for 150 V applied between its terminals in the absence of any mechanical load. As voltage is applied to the PZT it will stretch the microcylinder changing both its circumference and its index of refraction. As the

microcylinder stretches, its circumference decreases resulting in a shift of the WGM resonances towards shorter wavelengths or higher frequencies. WGM resonance shifts in excess of 120 GHz, mainly due to circumference change rather than refractive index variation, can be obtained depending on the microcylinder's dimensions.

Shifting the WGM resonances of a microcylinder is a condition *sine qua non* for the gas sensing experiment where gas absorption lines are typically narrow and the microcylinder's WGM spectrum is rather sparse with very rare situations in which a resonance occurs at the exact same frequency as the gas absorption line.

In order to make sure that the laser scans over a gas absorption line the vacuum chamber is connected to a 60 cm gas absorption cell (not shown in Figure III.1) probed by the same TDL using a beamsplitter. Whenever gas is inserted into the chamber it will also be present into the absorption cell; a typical Laser Spectroscopy (LS) setup is thus created in parallel with the sensing experiment using WGMs.

2. Results with various pressures

The first type of experiment targeted at gas detection consists of exciting microcylinder WGM resonances by scanning the TDL over the frequency region where a gas absorption line is present, and then varying the gas pressure. As described previously, a WGM is accompanied by an evanescent fraction *f*, a part of radiation that extends outside the boundary of the microresonator. Whenever the microresonator is surrounded by a medium that absorbs light at the operating wavelength, the round-trip loss for a certain WGM can be expressed as

$$\alpha l = \alpha_i l + f \alpha_m l \,, \tag{III.1}$$

where α_i is the intrinsic absorption coefficient, α_m is the molecular absorption coefficient of the medium outside the resonator, f is the evanescent fraction, and l is the circumference of the resonator.

Increasing the pressure of the gas surrounding the microresonator results in an increase in α_m that in turn produces an increase in the total round trip loss. An increase in the round-trip loss results in a decrease in the loss ratio defined as $x = T/\alpha l$. Depending on whether the WGM is initially overcoupled or undercoupled the WGM dip depth will increase or decrease respectively. Figure III.2 illustrates WGM dip depth variation with changing round-trip loss.

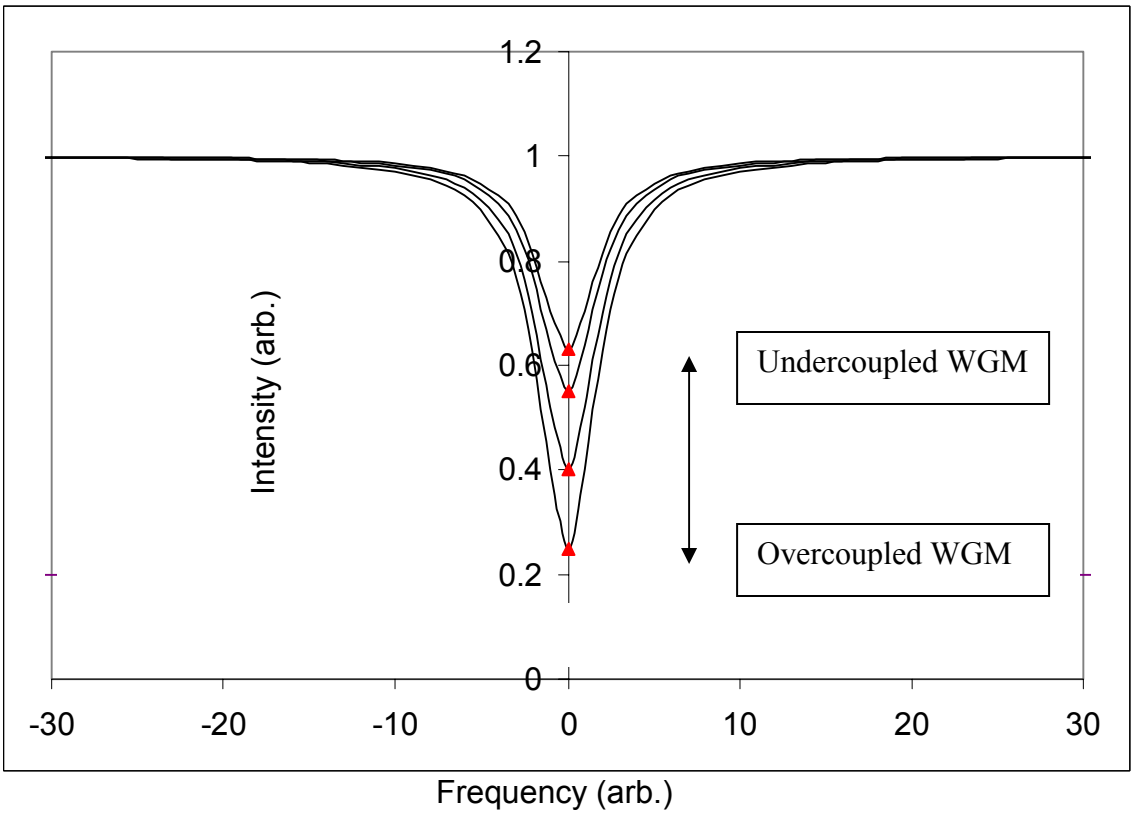

Figure III.2. WGM dip depth variation for overcoupled and undercoupled modes. Increasing the round-trip loss causes the overcoupled WGMs to become deeper; undercoupled WGMs become shallower.

Experimental results displaying a dip depth change with changing the pressure of the gas surrounding the WGM microresonator are presented in Figure III.3. The gas used in this experiment is methane (CH_4). At λ = 1650.96 nm it displays an absorption feature corresponding to a group of four absorption lines (the bottom red trace) in Fig. III. 3; also see Fig. III. 4 [67]. WGMs are excited in an 80 μm diameter microcylinder obtained by tapering a typical 125 μm diameter fiber. WGMs with the highest quality factor Q are then tuned to positions near resonance with the methane absorption feature.

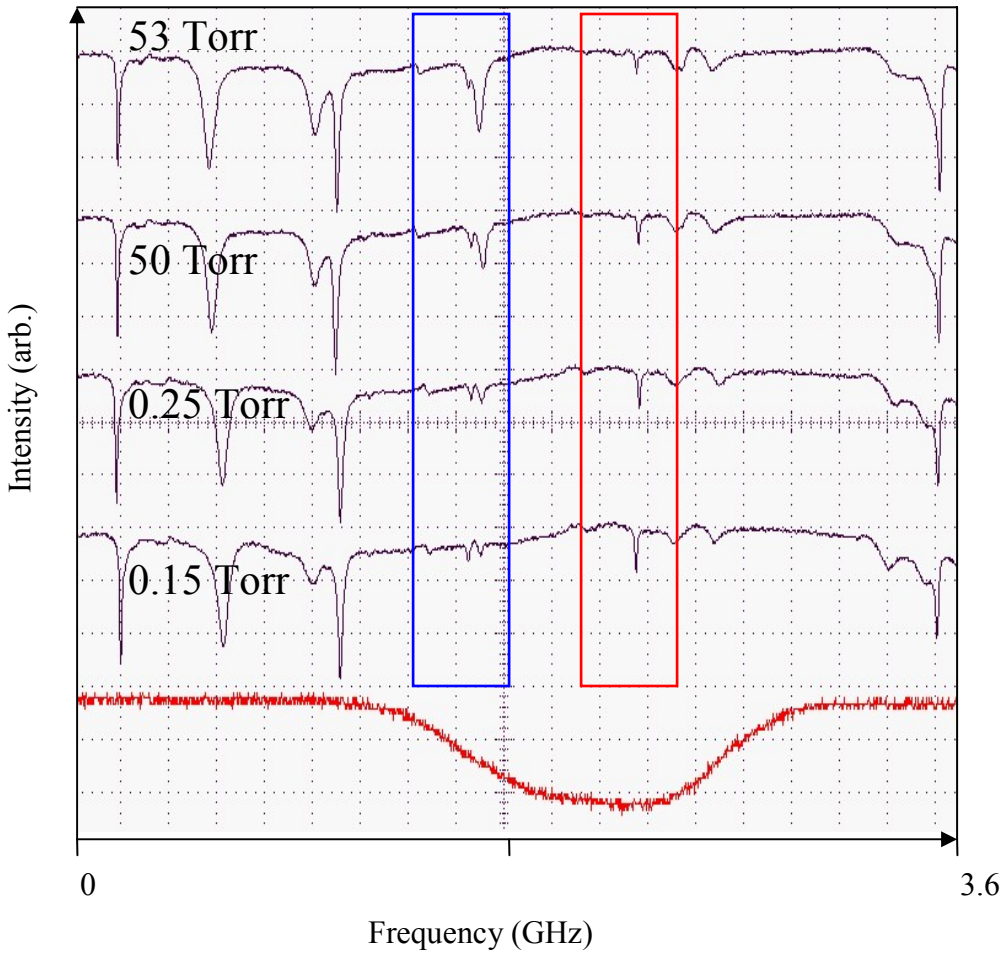

Figure III.3. Experimental results at various pressures. As the methane pressure is increased the undercoupled WGM resonances become shallower (red rectangle) while the overcoupled WGMs become deeper (blue rectangle). The bottom red trace represents the methane absorption feature at a pressure of 2 Torr.

It can be observed that the undercoupled WGM resonance highlighted in the red rectangle becomes shallower as the pressure and hence the absorption of the methane is increased. This particular WGM has a quality factor $Q = 10^7$. The relatively large changes in dip depth corresponding to changes in gas absorption coefficient correspond to an effective absorption pathlength $L^e_{eff} = 30$ cm.

The WGM in the red rectangle in Figure III.3 is tuned to be resonant with the strongest part of the methane absorption feature while the modes in the blue rectangle are initially not resonant with the absorption feature. It can be seen that as soon as the absorption feature broadens due to the increase in pressure the overcoupled mode in the blue rectangle starts displaying a change in its dip depth as it starts overlapping with methane's absorption feature.

Figure III.3 also reveals that even for large changes in the absorption coefficient in the environment surrounding the microresonator there is an extremely small change in the Full Width at Half-Maximum (FWHM) of the affected WGMs. Measuring the changes in dip depth is thus demonstrated once again as the best approach in using the microresonator WGMs as a trace gas sensor.

The four absorption lines in Fig. III.4 occur at 6057.077800 cm^{-1}, 6057.086100 cm^{-1}, 6057.099800 cm^{-1}, and 6057.127300 cm^{-1} [67]; the line centers span a frequency range of 1.50 GHz. They belong to the vibrational overtone ($2\nu_3$) band of the C-H asymmetric stretching mode. Their order is reversed relative to Fig. III.3 in which the scan direction is opposite. The FWHM Doppler-broadened linewidth is 565 MHz, and (self) pressure broadening makes the linewidth (FWHM) 6.5 MHz/Torr.

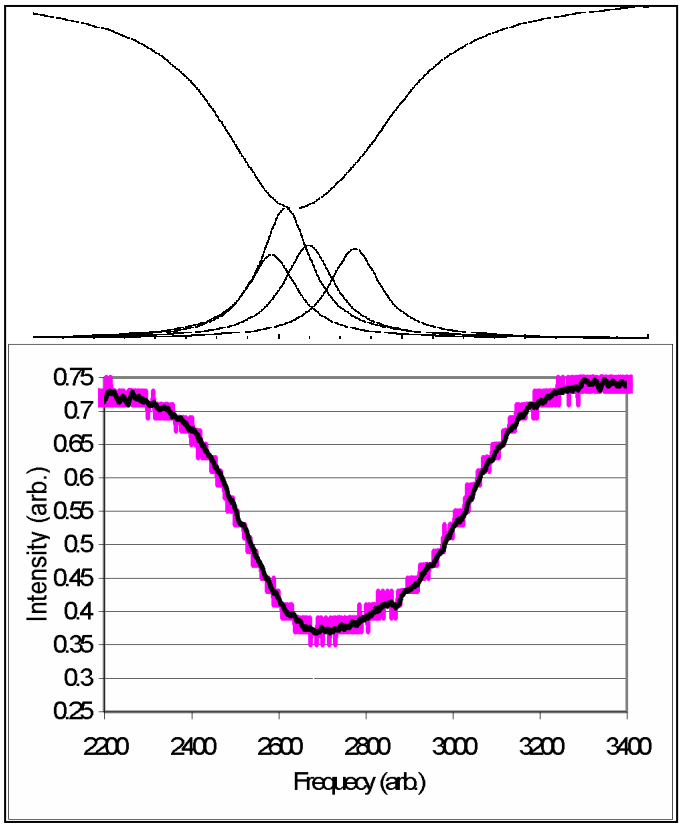

Figure III.4. Methane absorption profile at 1650.96 nm. The top trace is obtained using HITRAN data [67] assuming a pressure of 2 Torr. As the pressure increases beyond ~ 30 torr all the absorption lines become noticeably broader.

3. Results for tuning the modes across absorption lines

The results in section III.2 and in Figure III.3 suggest that WGM resonances are sensitive enough to probe minute changes in the absorption coefficient in the surrounding medium. The WGM resonance dips do not necessarily need to be tuned where the absorption feature of the gas is the strongest. The WGM highlighted in the blue rectangle in Figure III.3 demonstrates that the microresonator sensitivity is large enough to probe the entire profile of a gas absorption line.

The experimental setup for probing the absorption profile of the gas surrounding the microresonator is similar to the setup used in the previous section. But instead of tuning the WGM resonances to the frequency where the gas absorption profile is strongest and then investigating the changes in dip depth as the gas pressure is increased, in this setup the pressure of the gas is maintained constant and a WGM is tuned to various points on the gas absorption profile and the dip depth is recorded for each position. Figure III.5 illustrates this concept; it simulates tuning a WGM over the frequency region where a gas absorption feature is present.

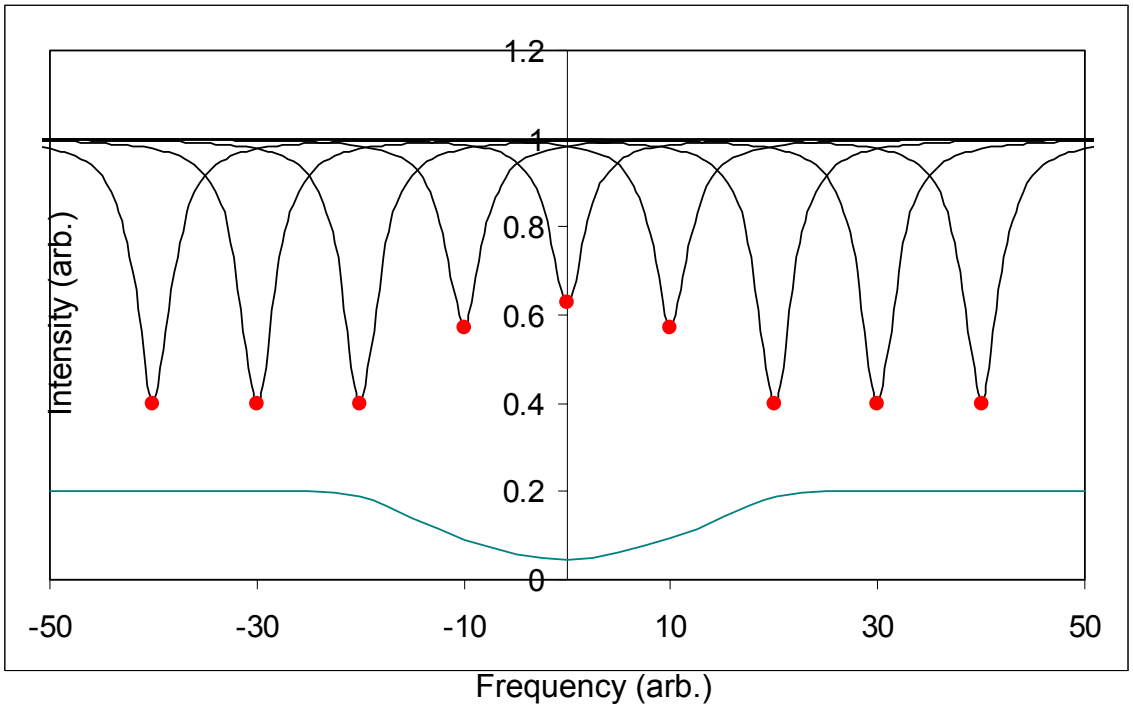

Figure III.5. Simulation of a WGM scanning over a gas absorption feature (blue, bottom trace). The vertical position of the dip (red dot) is recorded for each frequency position at which the WGM is tuned.

For this experiment the microresonator used was a 125 μm diameter microcylinder mounted as usual in a PZT stretching device. This diameter microresonator was chosen in order to assure a perfect cylindrical symmetry of the microcylinder. It is in fact a piece of very clean, unjacketed optical fiber. As the microresonator is tuned by stretching, it is crucial to maintain cylindrical symmetry in the event that while tuning the microcylinder might slide over the tapered fiber. An extremely small variation in the cylinder's diameter would result in such an instance in a rapid shift of the WGM observed. Even worse, with changing symmetry other unwanted modes could be excited and overlap with the one monitored.

A typical experimental result is presented in Figure III.6. Once again the gas investigated is methane. Inside the chamber that contains the tapered fiber and the

microresonator an atmosphere of pure methane at 200 Torr is created. The WGM marked with an arrow at the bottom of the figure is the one being investigated. For each trace corresponding to a different WGM resonance position a vertical offset is added for clarity. It is visible in the center of Figure III.6 that this undercoupled WGM becomes shallower as it scans over the strongest part of the absorption feature.

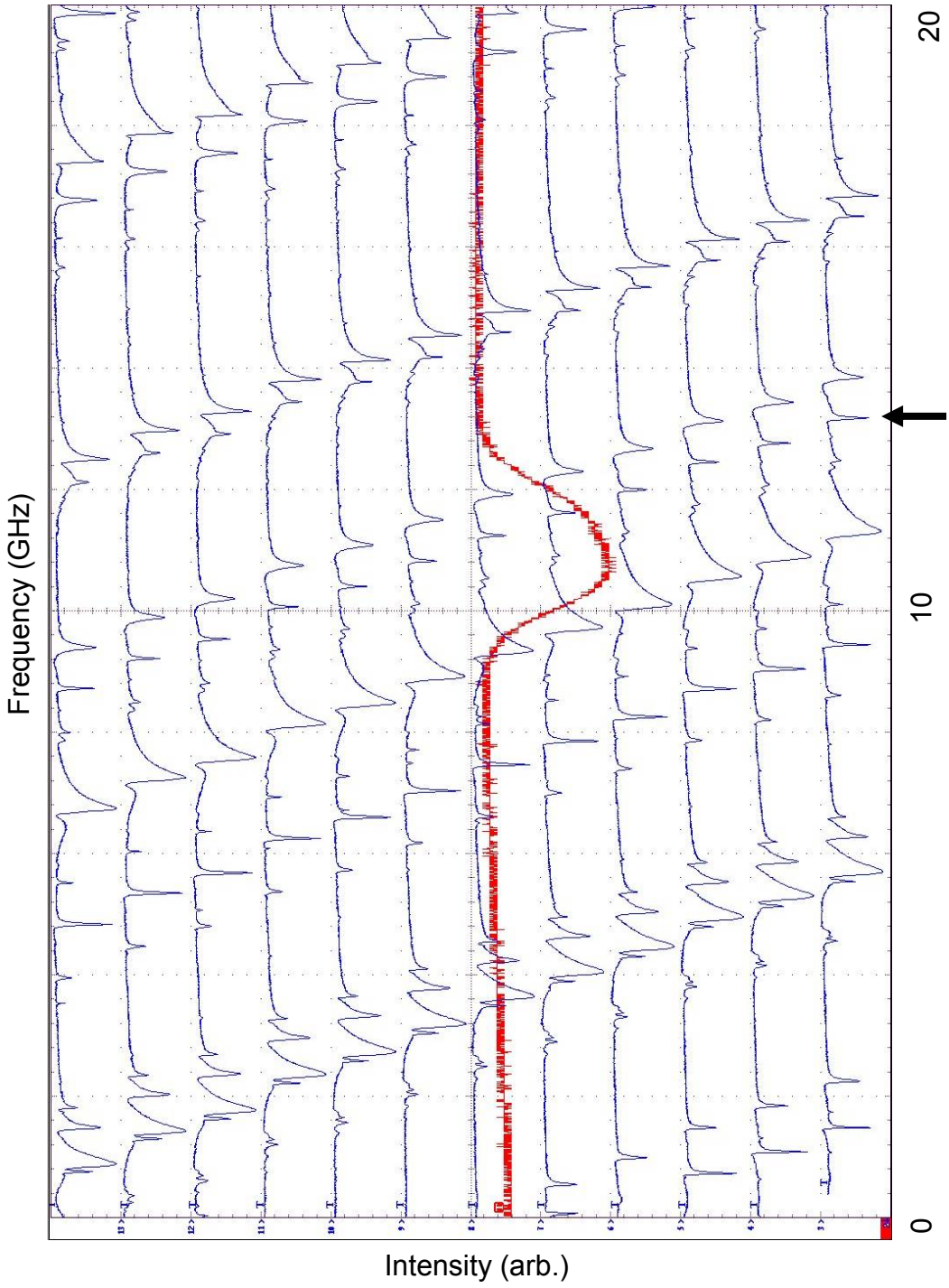

Figure III.6. Experimental results for scanning a WGM over a gas absorption line. From bottom up the WGM marked with an arrow scans over a methane absorption profile at 200 Torr (not shown). The red trace is the same absorption profile at 1650.96 nm but obtained for a pressure of 2 Torr.

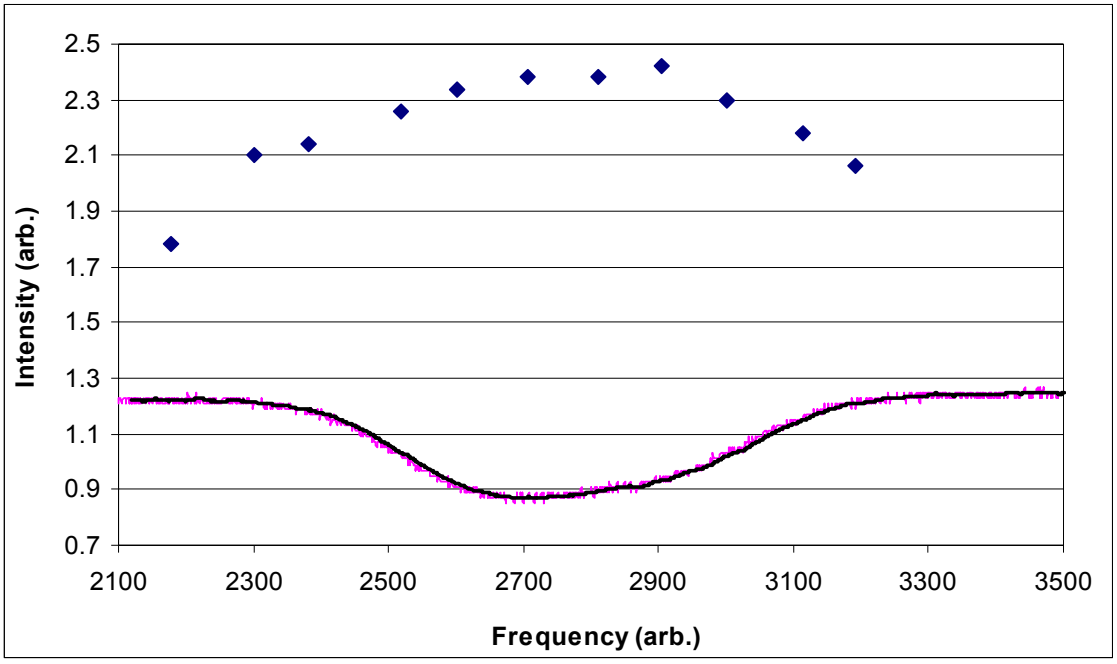

Figure III.7. The bottom of a WGM resonance dip (blue dots) as it is scanned over an absorption feature of methane at 200 Torr. The bottom trace is the methane absorption feature at 2 Torr used for reference.

A plot of the points corresponding to the bottom of the WGM dip observed in Figure III.6 is presented in Figure III.7. The collection of data points corresponding to the WGM's resonance dip bottom recreates the absorption feature of methane at 200 Torr. The quality factor of the WGM resonance used was $Q = 8\times10^7$. The experimental effective absorption pathlength of the WGM resonator can be again calculated and for this experiment L^e_{eff} = 26.8 cm. The same experiment was realized at a much lower methane pressure (1 Torr) and the results are presented in Figure III.8.

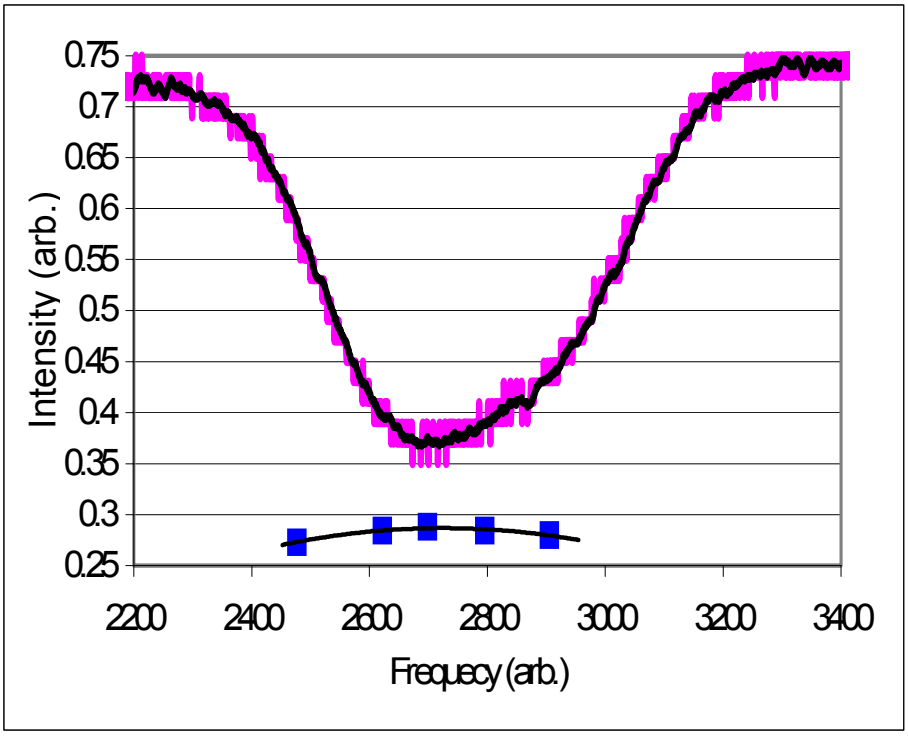

Figure III.8. The position of the bottom of a WGM (blue squares) as it scans over an absorption line of methane at 1 Torr. The top trace is the methane absorption feature recorded at 2 Torr.

4. Results with locked modes

An experiment analogous to cavity enhanced laser spectroscopy (LS) using microresonator whispering-gallery modes (WGMs) is presented in this section. WGMs are excited along the circumference of a cylindrical cavity 125 μm in diameter using an adiabatically tapered fiber. The microresonator is mounted into a PZT fixture that enables locking individual WGMs to a TDL. As the TDL is scanned in frequency over a gas absorption the changes in the dip depth of the locked WGM are recorded.

When a WGM is frequency-locked to the input laser the WGM is always on resonance with the laser and, as the laser scans in frequency, the output of the bi-tapered fiber displays the locus of the bottom of the WGM resonance dip as it follows the laser scan. When an absorption line of the surrounding gas is present within the scan there is a change in the WGM dip depth that traces the contour of the gas absorption line. Since the microresonator is on resonance, light interacting with the gas executes many round-trips around the circumference, giving rise to a long effective interaction path length.

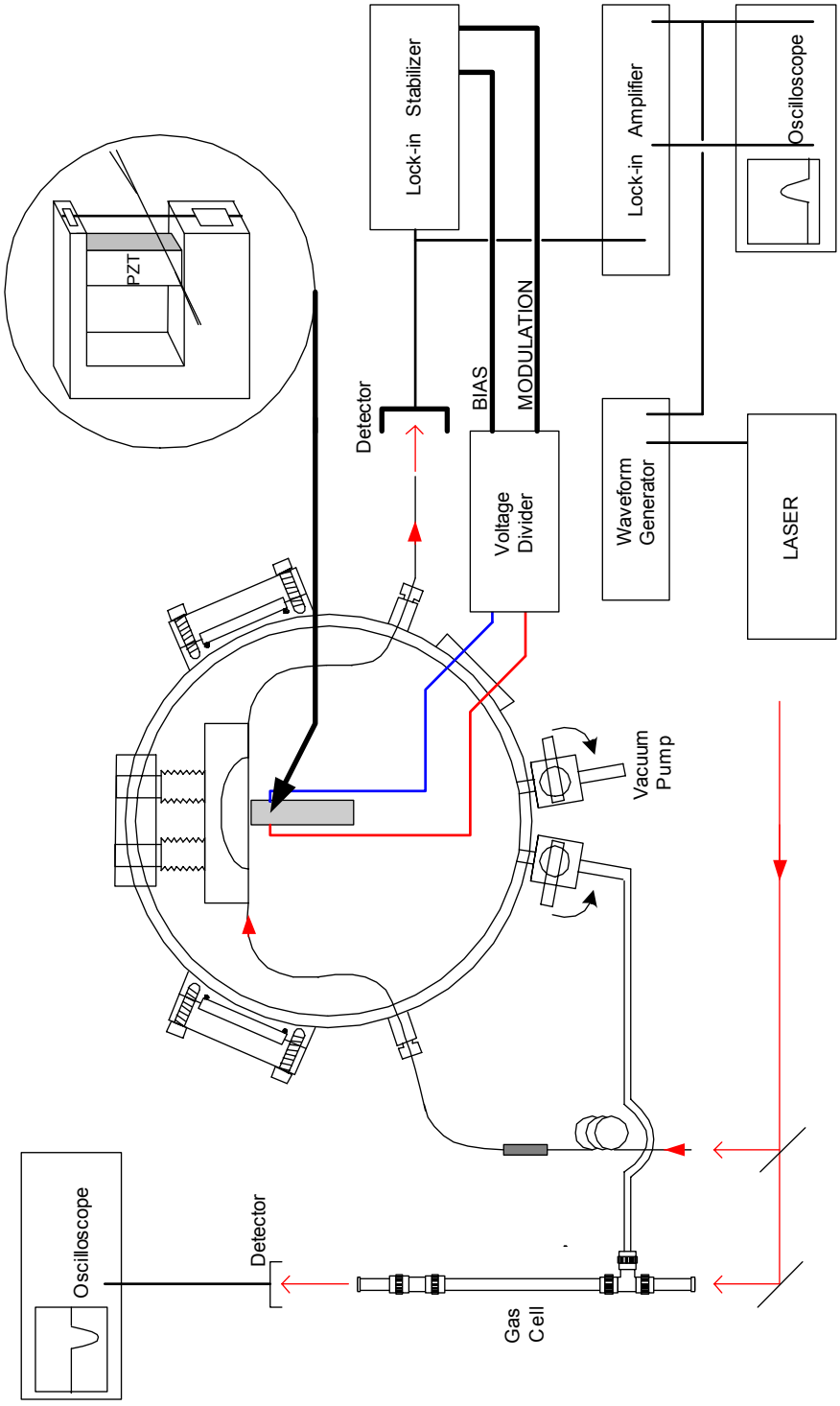

Figure III.9. Experimental setup for locking a WGM to the laser. Light from a frequency-scanned cw TDL (red) is launched into a bi-tapered fiber to excite WGMs of the microresonator. The microresonator is held in a PZT fixture for tuning purposes (inset).

Figure III.9 shows the experimental setup. Laser light is coupled into a single-mode optical fiber. After passing through a polarization controller it is fed into the gas chamber where its adiabatic bi-taper is brought in contact with the microresonator. As it exits the chamber the output of the fiber is collected onto a detector. The microresonator is mounted in the PZT fixture (inset Figure III.9) that allows tuning of the WGMs by stretching the resonator. The signal from the detector is split, part of it being fed into a lock-in stabilizer in order to lock individual WGMs to the laser, and part of it is noise filtered and amplified by a lock-in amplifier. The output of the lock-in amplifier is monitored by an oscilloscope. A reference cell containing the same gas as the chamber is used for calibration purposes.

A typical experimental result is presented in Figure III.10. The bottom trace represents the absorption line(s) of pure methane at 1650.96 nm obtained using the 60 cm long reference cell at 160 Torr. The absorption lines are saturated due to the high pressure and long absorption path length in the cell.

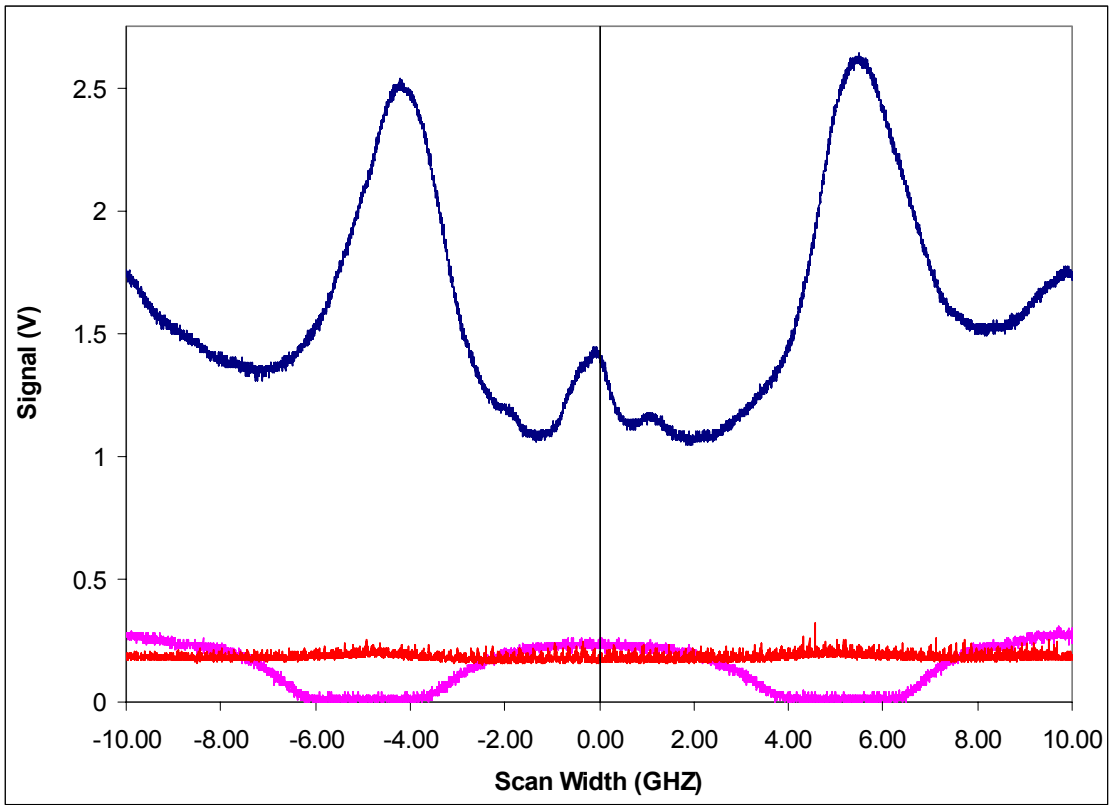

Figure III.10. Typical experimental result with locked WGMs. The bottom (pink) trace represents the absorption line(s) of pure methane obtained using a 60 cm long reference cell at 160 Torr. Right above it is the signal at the output detector representing the bottom of a WGM as it scans, along with the laser, over the absorption line(s) of methane (red). This component of the signal is removed by the lock-in amplifier that also gives a 50X signal amplification (top blue trace).

Right above the saturated reference cell trace in Fig. III. 10 is the signal at the output detector representing the bottom of a WGM as it scans, along with the laser, over the absorption line(s) of methane. A small curvature upwards can already be observed due to the fact that the undercoupled resonance dip becomes shallower as it interacts evanescently with the methane. What appears to be noise is in fact the fast

modulation (512 Hz) applied to the PZT by the lock-in stabilizer. This component of the signal is removed by the lock-in amplifier that also gives a 50X signal amplification (top trace).

The WGM used in this case had a Q of approximately 10^6 and the dip depth was 66% of the off-resonance signal level. An effective absorption pathlength of approximately 3 mm is obtained.

Experimental results like those presented in Figure III.10 were also obtained for various gases as trace gases in one atmosphere of air. The trace gases investigated were methyl chloride [68], ethylene [69], and again methane. These results [70] are presented in Figure III.11 and the data are summarized in Table III. 1.

The experimental effective absorption pathlength was obtained using Eq. (II.37) in which, in the case of methane, $M_0 = 68.4\%$, $\Delta M = 0.7\%$ and using a value of the absorption coefficient extracted from the traces obtained with a 16 cm long absorption cell ($\alpha_m = 0.0058$ cm^{-1}). The theoretical effective absorption pathlength is calculated using Eq. (II.35) using $x = 0.28$, $f = 1.5\%$, and $\alpha_i = 0.0056$ cm^{-1}.

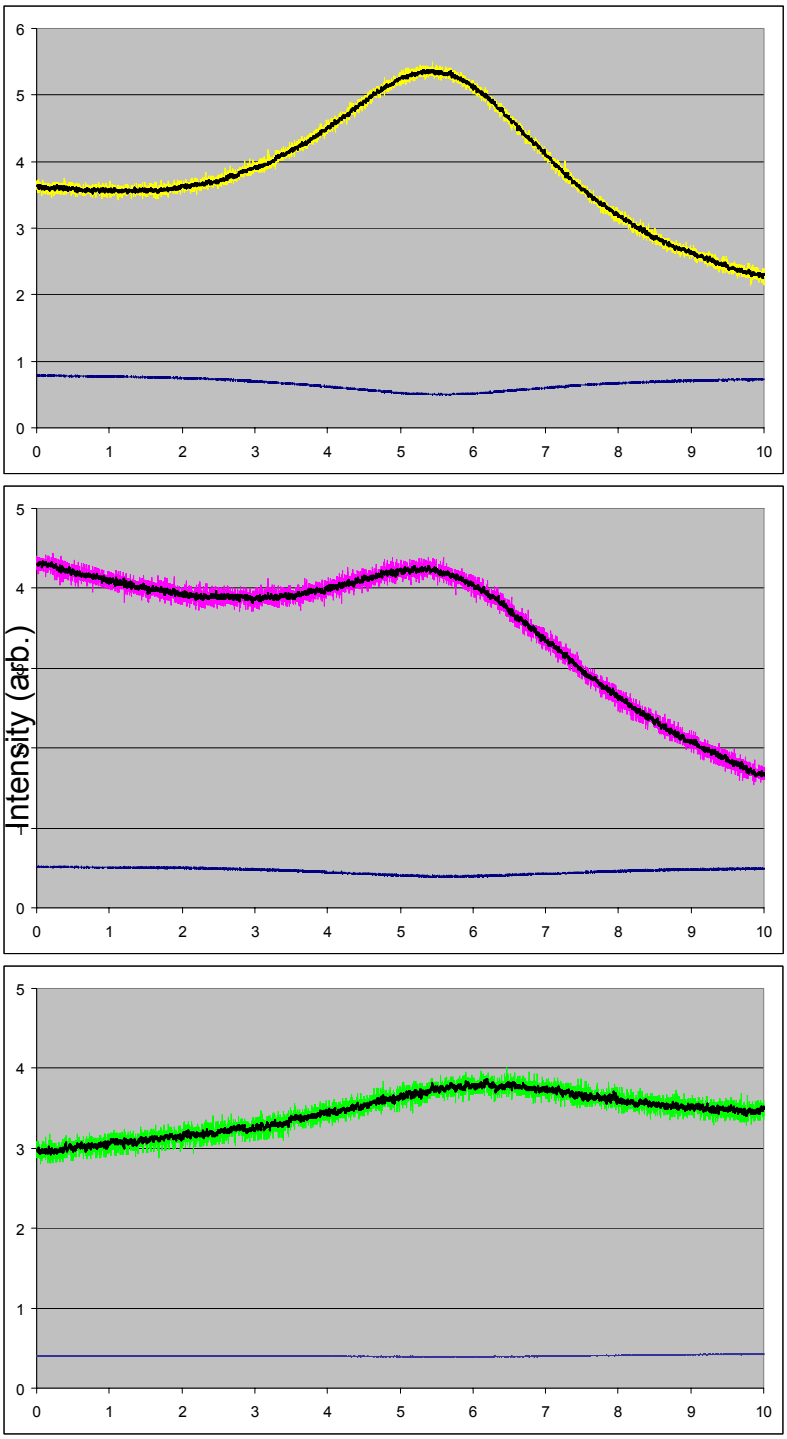

Figure III.11. From top down: The absorption profile of methane, methyl chloride, and ethylene obtained using a WGM locked to the laser. In each graph the bottom trace is the absorption profile of the investigated gas in a 16 cm absorption cell.

Table III.1 summarizes the data for each trace in Figure III.11.

Gas	L^t_{eff} (mm)	L^e_{eff} (mm)	WGM Q	λ (nm)	Trace amount
CH_4	15.0± 3.0	17.7 ± 1.7	7×10^6	1653.722	1%
CH_3Cl	7.2 ± 1.5	6.3 ± 1.1	3×10^6	1651.59	1%
C_2H_4	13.6 ± 2.7	13.2 ± 2.6	5×10^6	1654.23	2%

Table III.1. Summary of data for Figure III.11.

For each trace gas in Table III.1 there is a good agreement between the theoretical and experimental effective absorption path length. For the theoretical values the main source of error is in approximating the evanescent fraction for the WGM used. The measured α_m uncertainty and the noise on the traces corresponding to the locked WGMs are responsible for the error in determining the experimental effective absorption path length.

No accurate details could be found at these wavelengths for the absorption lines of ethylene and methyl chloride. However, general properties of these lines can be found in [68,69]. The HITRAN database [67] describes the absorption lines of methane in this wavelength range and they correspond to the C-H asymmetric stretching vibrational overtone $2\nu_3$. There are three lines of approximately equal strength and approximately equally spaced at intervals of 600 MHz, pressure broadened by air to approximately 4 GHz each.

5. Conclusions

This chapter investigated the feasibility of a gas sensor based on a WGM resonator. Using high Q microresonators enables enhanced sensitivity corresponding to tens of centimeters effective absorption pathlength. This is obtained in an extremely small detection area having the ability to probe small samples. This is particularly useful in many applications. A gas chromatography setup can be envisioned in which the entire section dedicated to gas detection, usually a multipass absorption cell, can be replaced by a small microresonator, much smaller than the separation column. The major limiting factor in the portability of a gas chromatography setup is the massive detection section and the use of this novel gas detection can, in principle, be a step further towards miniaturization.

Locking the WGM resonances to the laser and obtaining a Laser Spectroscopy analogue setup is, to our knowledge, the first demonstration of such an experiment. The major advantage of our setup is again the miniaturization. Although the detection area is micrometric, relatively large effective absorption pathlengths on the order of tens of centimeters were obtained. An analogy can be made with a typical multipass cell in which 50-100 meters of effective absorption pathlength are obtained using multipass cells with dimension on the order of tens of centimeters. However, the price of a modest multipass cell greatly exceeds the price of one inch of standard optical fiber and a PZT element.

The somewhat modest effective absorption pathlength in our LS equivalent experiment is mainly due to the low quality factor of the WGM resonances used; they are typically not much greater than 10^6. WGM resonances with a quality factor as large

as 10^8 are routinely obtained in our cylindrical microresonators but the current equipment cannot lock such sharp modes to the laser. A WGM is locked to the laser using a lock-in stabilizer that supplies the PZT element stretching the microresonator with a DC bias voltage and an AC dither. The DC bias voltage brings the WGM in resonance to the laser and the AC component dithers the mode about the laser line. The higher the quality factor of the resonator, the smaller the amplitude of the dither signal has to be. For the results presented, the dither amplitude is already at the minimum possible dither amplitude provided by the lock-in stabilizer.

Other resonator geometries can also be envisioned for enhancing the sensitivity and stability of the setup. Using a fiber fusion splicer, a microspheroid resonator with two stems can be obtained. Mounting it into the same PZT device would enable tuning the WGMs in the same fashion as the microcylinder. However the curved surfaces of the microspheroid should, in principle, result in higher Q WGMs.

CHAPTER IV

LIQUID SENSING

1. Setup

In addition to gas sensing, WGM microresonators were successfully used for chemical sensing of chemicals dissolved in a liquid. In order to investigate the feasibility of chemical detection the investigation was conducted at two different wavelengths, 800 nm and 1550 nm. The chemicals to be detected were Indocyanine green and SDA2072, each in solution in methanol. Indocyanine green has an absorption profile with the maximum of absorption at around 790 nm [71] while the SDA2072 has its peak absorption at 956 nm with significant absorption in the 1550 nm range [72]. Since the absorption profile of both dyes is extremely broad, extending over hundreds of nanometers, no tunability of the microresonator is necessary. This results in a more simplified experimental setup that eliminates the need for a PZT device. Moreover, spherical microresonators can be used as described in Chapter I. A typical microsphere has a diameter of approximately 500 μm and it is obtained by melting an end of a standard optical fiber. A tapered fiber is brought in contact with the microsphere tangential to its equator as sketched in Figure IV.1 inset.

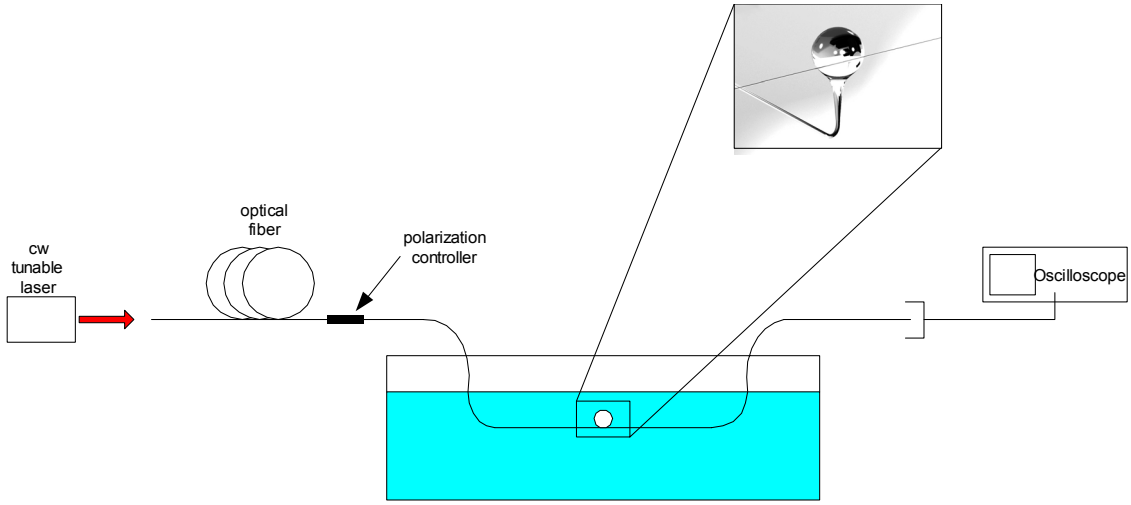

Figure IV.1. Experimental setup for liquid sensing. Light from a cw tunable laser is injected into the optical fiber. The tapered part of the fiber and the microsphere are immersed in the solution to be investigated. Output of the fiber is monitored on an oscilloscope as the laser scans in frequency.

For each wavelength a single mode optical fiber was used. In both cases the taper was adiabatic, single mode propagation being thus ensured throughout the entire length of fiber. A polarization controller was also used before the taper to ensure excitation of WGMs of a single polarization, either TE or TM.

Both the microsphere and the tapered fiber are then immersed into the liquid to be analyzed. As the concentration of the analyte is increased the WGM resonance dips are monitored for changes in dip depth or quality factor. Once again, the changes in dip depth prove to be far easier to observe.

The vessel containing the solution to be analyzed is made entirely out of glass to permit easy alignment of the tapered fiber tangential to the circumference of the microsphere using a 45X microscope. Glass is also ideal to prevent the contamination of

the methanol solution. The clamp that holds the tapered fiber is made of Delrin, a material that also has no reactivity with the methanol.

Two three-dimensional translation stages are used to control the precise position of the microsphere and of the tapered fiber, while a small laboratory jack is used to raise the vessel and thus immerse the microsphere-tapered fiber system.

2. ICG Results

Using the setup described in the previous section, the first trial was done using a cw Ti:Sapphire tunable laser operating at a wavelength of about 800 nm. At this wavelength the methanol used as a solvent for the ICG dye makes a negligible contribution to the absorption. In order to test this a 1 m glass cylinder filled with methanol was inserted in the laser beam path and the attenuation due to methanol's presence proved to be minimal.

A typical experimental result is presented in Figure IV.2.

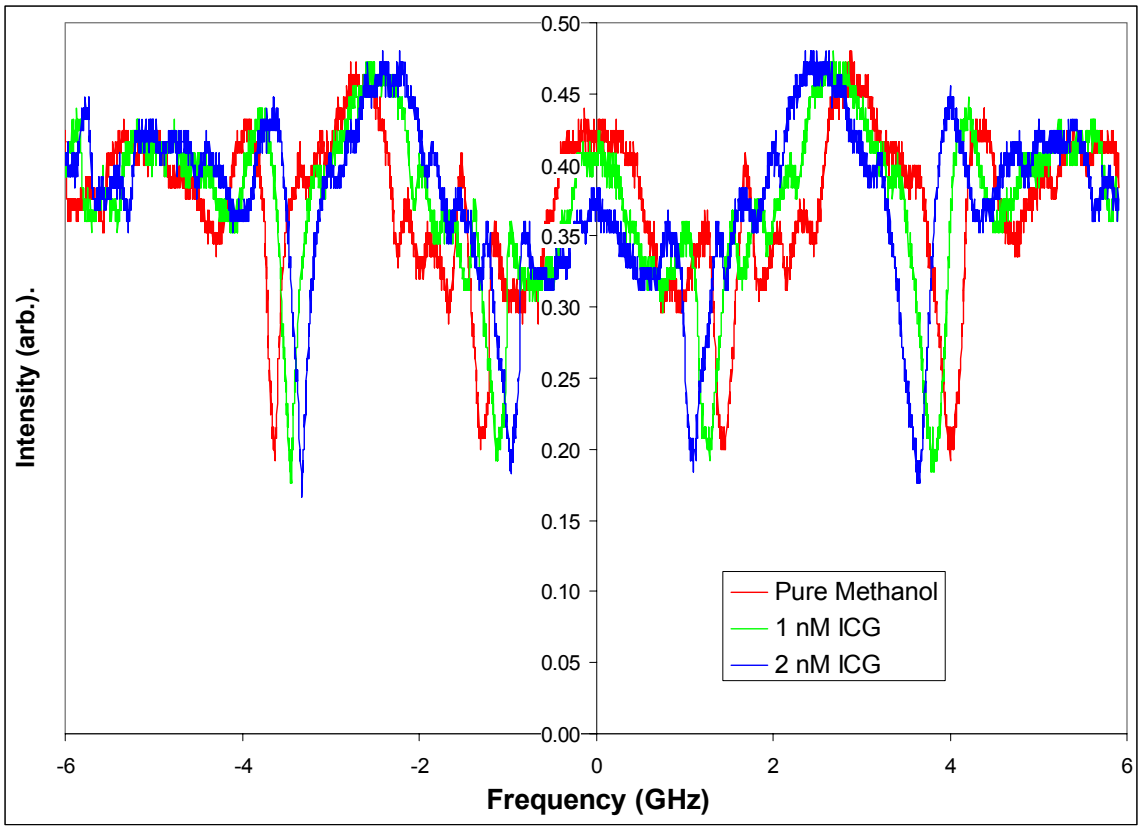

Figure IV.2. Experimental results at 800 nm. Red trace represents a WGM spectrum of a 500 μm microsphere immersed in methanol. Adding ICG in order to create a 1 nM concentration results in a deeper WGM resonance (green trace). As the concentration is further increased to 2 nM the WGM resonance becomes deeper (blue trace).

The two sides of the graph in Figure IV.2 represent a scan over the same frequency range, first up and then down in frequency with the scan turning point being in the middle. Also, WGMs are artificially shifted in order to better observe the resonance dip depth change.

The WGMs investigated have a quality factor Q of approximately 10^6. Such a value for the quality factor is typical for a microsphere immersed in methanol. This is mainly due to the fact that although quite transparent at this wavelength methanol has a larger absorption coefficient than air at the same wavelength. Quality factors exceeding 10^9 have been routinely obtained using the same setup in air. Also, the index of refraction of the methanol plays a role in the decreased quality factor. Since the refractive index contrast between the microsphere and the surrounding medium gives the value of the evanescent fraction of a certain WGM it is obvious that for a smaller refractive index contrast more radiation extends outside the microsphere's boundary resulting in a larger evanescent fraction while immersed. The index of refraction of methanol is 1.33 while the index of refraction for a microsphere is 1.45 at this wavelength.

Changes in the WGM resonance dip depth are relatively large considering the small changes in the solution's absorption coefficient $\alpha_m = 0.026$ m^{-1}/nM. This results in a large experimental effective absorption pathlength $L^e_{eff} = 3.08 \pm 0.3$ m using the deep dip on the left of Fig. IV.2.

A theoretical effective absorption pathlength $L^t_{eff} = 2.83 \pm 0.3$ cm is calculated assuming an evanescent fraction $f = 3\%$ in Eq. (II.35).

3. SDA2072 Results

In the previous section nM changes in dye concentration could easily be detected using WGMs excited in the 800 nm wavelength range where the solvent absorption is not a big factor. In this chapter a similar experiment is presented at wavelengths in the 1550 nm range where the solvent absorption is much stronger. At 1550 nm the laser intensity is attenuated more than 10^3 times after propagating through only 1 cm of solvent. The solvent used in this case is again methanol. At this wavelength methanol has a measured absorption coefficient $\alpha_s = 8.8\ cm^{-1}$. Acetone is slightly more transparent than methanol but the technical difficulties in using acetone as a solvent greatly overcome the benefits of a modestly improved transparency.

The dye used in this experiment is SDA2072 (HW Sands Corp.) [72]. It has an absorption peak at 956 nm but has still significant absorption at 1550 nm as shown in Figure IV.3.

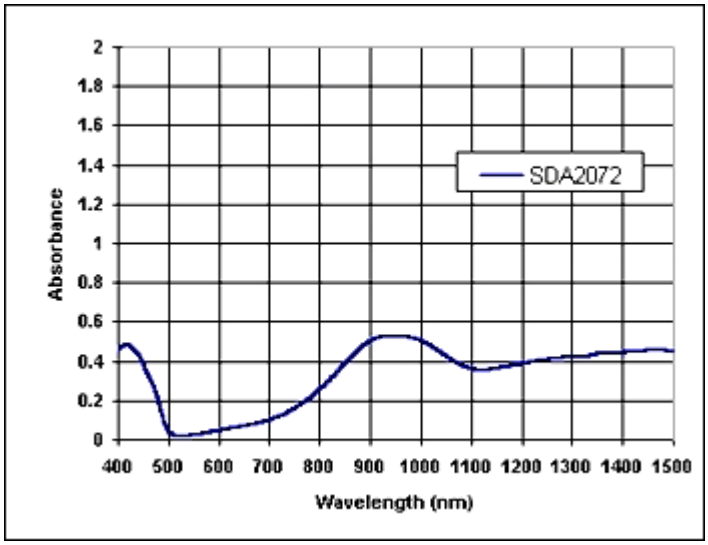

Figure IV.3. SDA2072 dye absorption spectrum [72]. A significant absorption at 1550 nm can be inferred. Solvent used is methanol.

The experimental setup is the same as in the previous section. All the positioning equipment for aligning the tapered fiber to the equator of the microsphere, along with the fiber polarization controller and the solution container are mounted on an optical breadboard that allows easy transportation of the entire setup from one laser to the other.

A typical experimental result is presented in Figure IV.4.

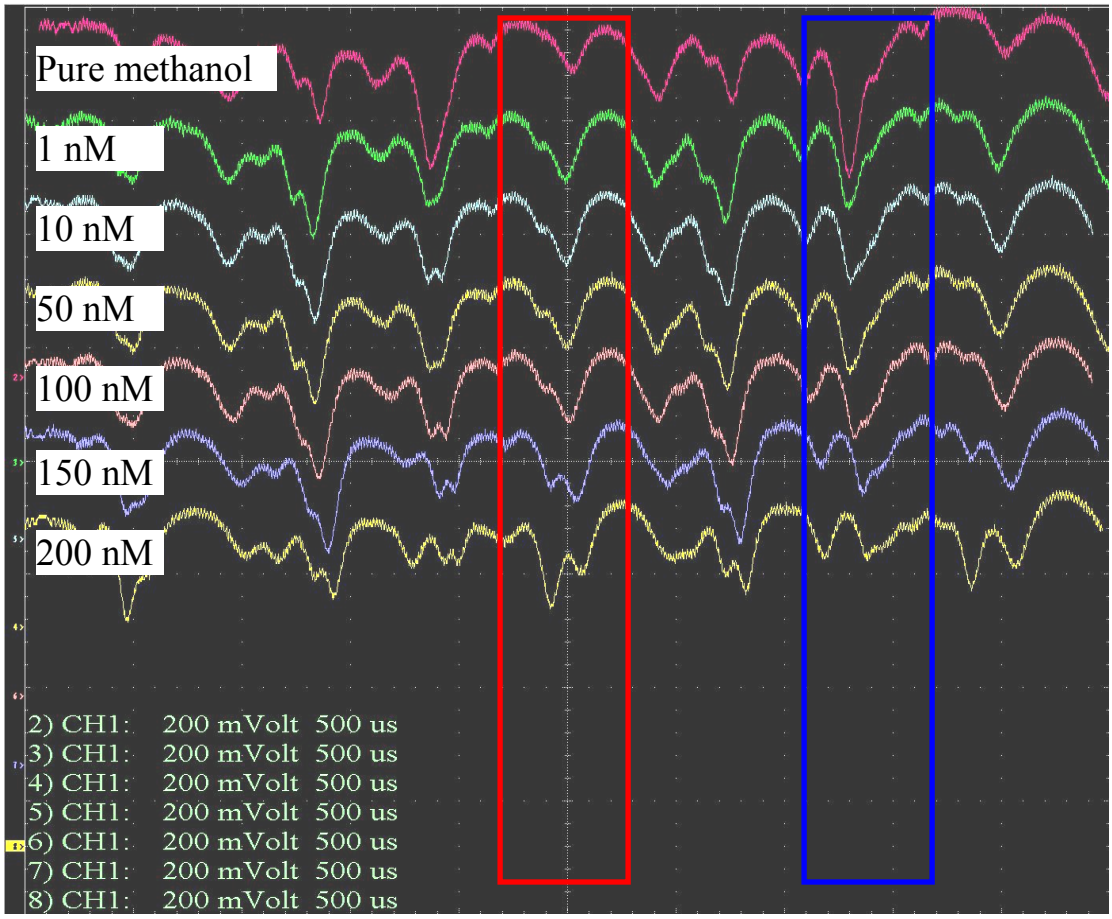

Figure IV.4. Typical experimental result for liquid sensing at 1550 nm. Changes in WGM resonance dip depth with changing concentration of SDA2072. Undercoupled modes become shallower with increasing concentration (blue rectangle) and overcoupled modes become deeper (red rectangle). The traces are vertically shifted for clarity.

The absorption coefficient of SDA2072 is extrapolated from measurements at higher concentration to be $\alpha_m = 0.004$ m^{-1}/nM at 1550 nm.

Figure IV.4 is analogous to Figure III.3. In both figures within the same WGM spectrum both overcoupled and undercoupled modes are observed. As the round-trip loss is increased by increasing the gas pressure and the dye concentration respectively, the overcoupled modes become deeper and the undercoupled modes become shallower. Unfortunately, in Figure IV.4 the WGMs highlighted overlap with the adjacent modes and measurements using these modes would be affected by errors. Figures IV.5 and IV.6 display cleaner WGM spectra on which reliable measurements could be performed.

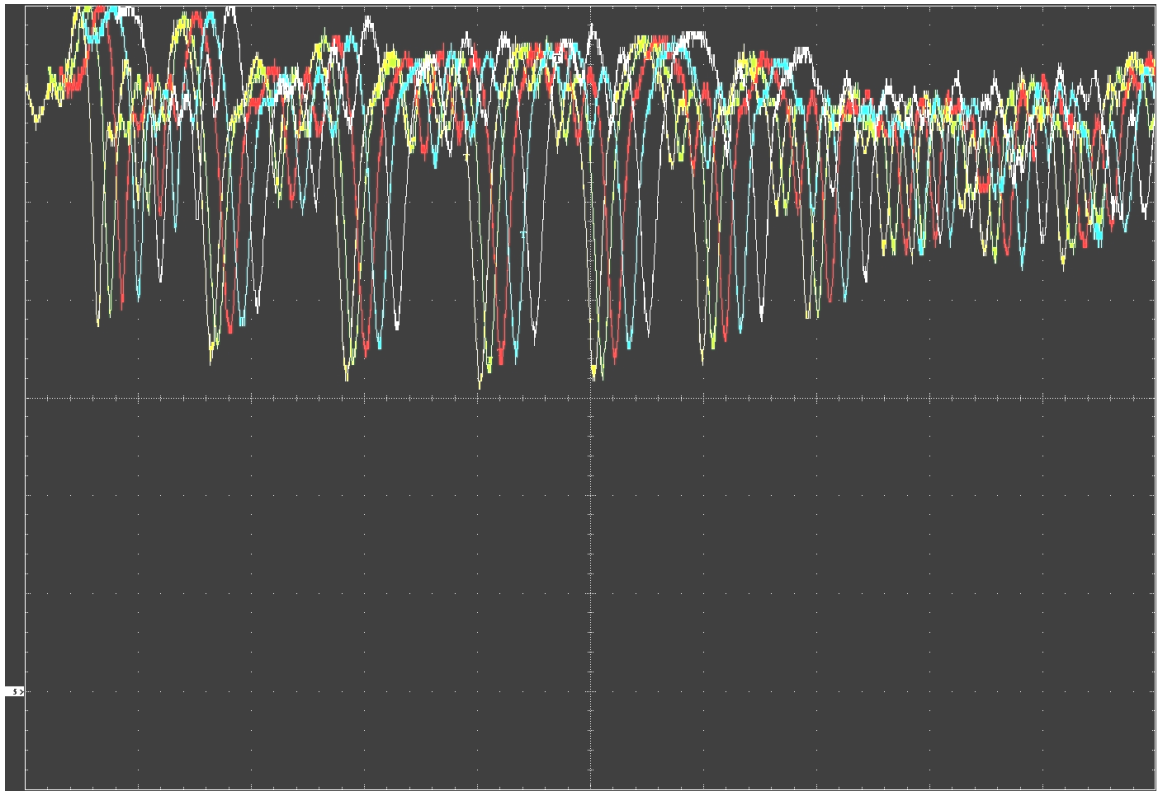

Figure IV.5. Experimental result for liquid sensing at 1550 nm (undercoupled case). SDA2072 concentration is increased in steps of 1 nM. For clarity WGM are shifted to the right as the concentration increases. For each waveform the leftmost WGM is obtained in pure methanol. Each horizontal division corresponds to 1 GHz.

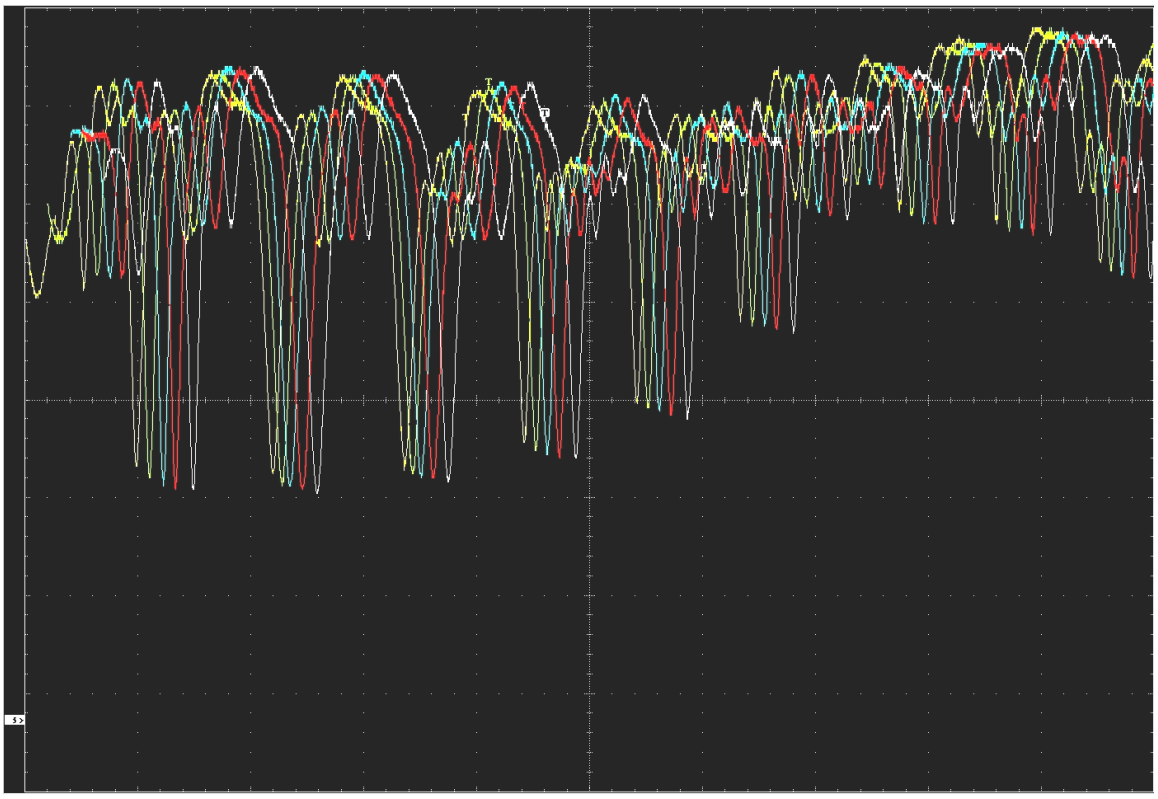

Figure IV.6. Experimental result for liquid sensing at 1550 nm (overcoupled case). SDA2072 concentration is increased in steps of 1 nM. For clarity WGM are shifted to the right as the concentration increases. For each waveform the leftmost WGM is obtained in pure methanol. Each horizontal division corresponds to 1 GHz. Microsphere diameter is 600 μm.

The experimental effective absorption pathlength (determined for the fifth dip from the left in Figure IV.6) is $L^{e}_{eff} = 8.4 \pm 0.8$ m. The theoretical effective absorption pathlength is determined from Eq. (II.34) to be $L^{t}_{eff} = 3.1 \pm 0.3$ cm.

Once again, just as in the ICG case, at 800 nm, the theoretical effective absorption path length is two orders of magnitude smaller than the experimental one. Although the reason remains unknown a few speculations can be made. At high concentrations both dyes "stain" the glass container suggesting that the dye molecules tend to adhere to the microsphere surface resulting in a stronger measured absorption and consequently a

longer experimental effective absorption path length. Also, the theoretical effective absorption path length is calculated using a 3% evanescent fraction.

The ability to measure the weak absorption of the dye ($\alpha_m \sim 4$ä10^{-5} cm^{-1}) in a strongly absorbing solvent ($\alpha_s \sim 8.8$ cm^{-1}) with effective absorption pathlengths on the order of meters is the main figure of merit of this sensing technique. This level of sensitivity cannot be achieved with a traditional method based on an absorption cell due to the large attenuation in the solvent.

4. Evanescent fraction measurement

So far, various schemes for chemical sensing using microresonator WGMs have been proposed. Ultimately all of them rely on the fact that the radiation in a dielectric WGM resonator extends outside the geometrical boundary of the resonator thus being able to interact with the medium surrounding the microresonator. The evanescent fraction or the ratio *f* of the WGM's evanescent mode volume to the total mode volume of the respective WGM could only be calculated but not easily measured.

A method for measuring the evanescent fraction of a whispering-gallery mode (WGM) obtained in a microsphere is presented in this section. The microsphere is immersed in methanol and the loaded quality factor of a critically coupled WGM Q_0 is measured. A 4.43 μM concentration of absorbing dye (SDA 2072, H. W. Sands Corp.) is then created with a measured absorption coefficient of $\alpha_m = 0.16\ \text{cm}^{-1}$. Once again the loaded quality factor Q for the same critically coupled WGM is measured. The change in loaded quality factor of the critically coupled WGM is directly related to the evanescent fraction, the amount of radiation extending outside the microresonator geometrical boundary. A method for direct measurement of the evanescent fraction is crucial for designing microsphere WGM-based chemical sensors.

Microsphere WGMs are excited using an adiabatically tapered fiber placed tangentially in contact. Laser light from the TDL is injected into the tapered fiber at one end and at the other end the throughput is monitored on an oscilloscope as the TDL is scanned in frequency. As usual, the throughput will display sharp Lorentzian dips corresponding to the WGM resonances of the microsphere. The whole microsphere-tapered fiber system is immersed in pure methanol and the position of the microsphere

along the gradually tapered fiber is carefully chosen in order to obtain a critically coupled WGM. Figure IV.7 illustrates the experimental setup.

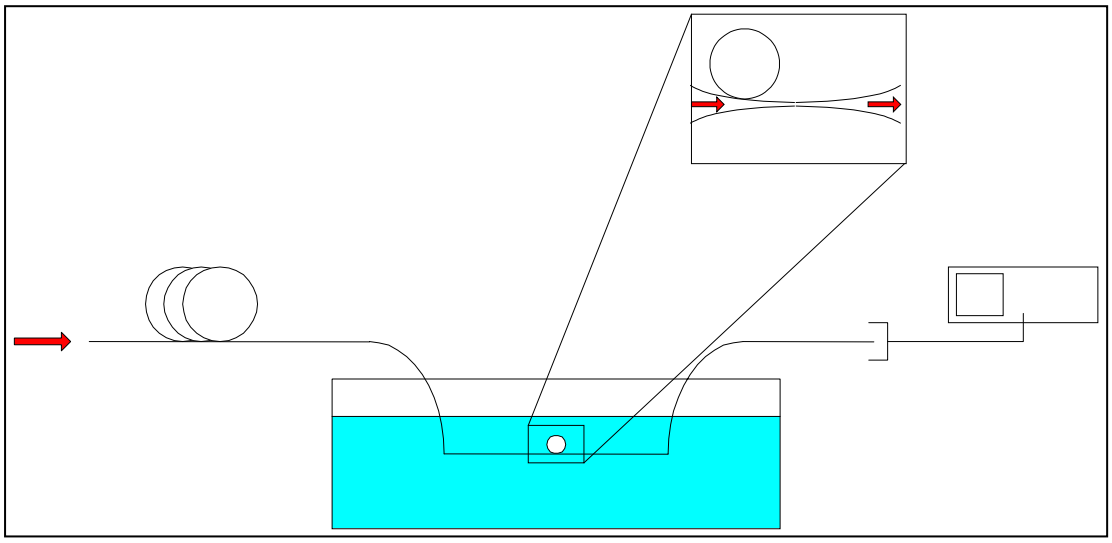

Figure IV.7. Experimental setup for evanescent fraction measurement. The microsphere is translated along the tapered fiber in order to obtain a critically coupled WGM.

Practically, a change in the microsphere's position along the taper results in a change in the coupling loss of the microresonator and whenever the coupling loss equals the intrinsic loss the WGM resonance dip reaches maximum amplitude extending all the way down to zero throughput. The FWHM of the WGM is recorded; it is a measure of the total quality factor Q_0 of the microsphere. Next, absorbing dye is added (SDA2072); this will result in an increase of intrinsic loss due to optical attenuation in the evanescent part of the WGM. Since coupling loss remains constant the WGM departs from the critical regime becoming shallower. Once again the microsphere is translated along the

taper in order to increase the coupling loss to a value equal to that of the new intrinsic loss; critical coupling is again obtained. These steps are presented in Figure IV.8.

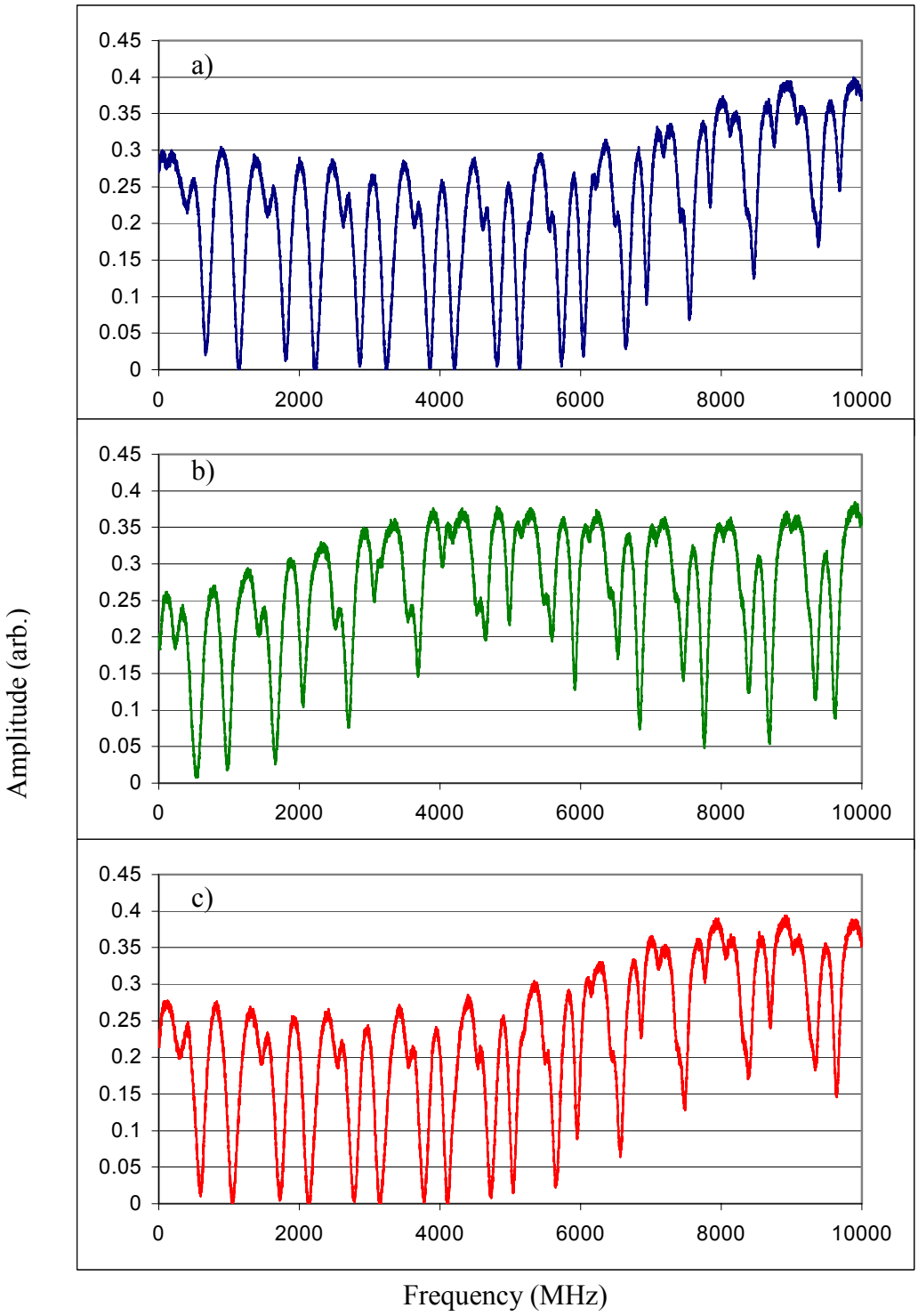

Figure IV.8. Experimental procedure for measuring the WGM evanescent fraction.
a) Critically coupled modes are obtained in pure methanol.
b) SDA2072 dye is added
c) Critically coupled modes are again obtained after sliding the microsphere along the taper

The FWHM is measured again so the total quality factor Q can be obtained in the presence of the absorber within the evanescent fraction of the WGM.

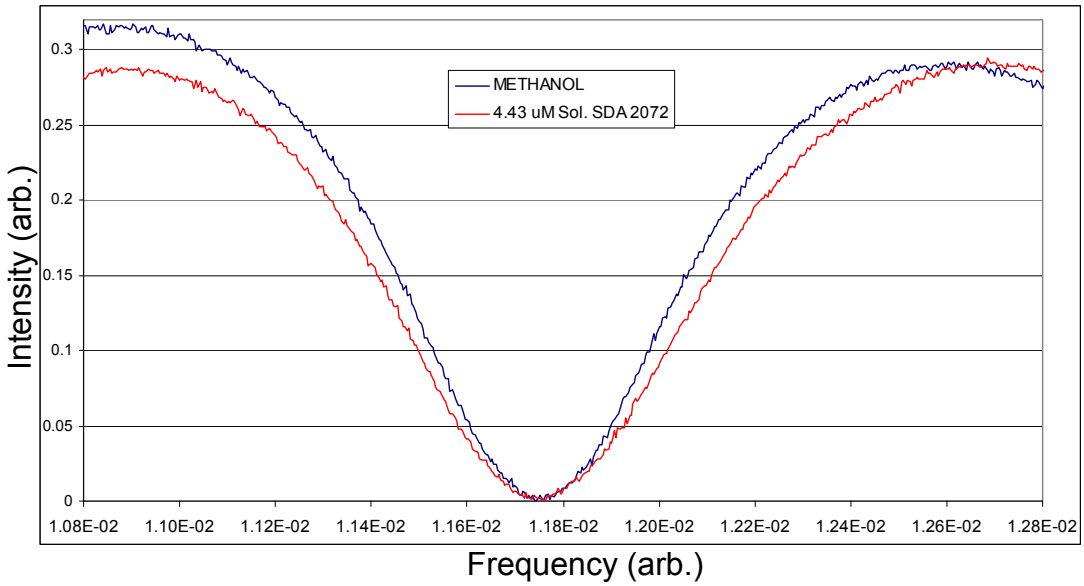

Figure IV.9. Experimental result for measuring the evanescent fraction. The FWHM for the WGM before and after adding SDA2072 dye is measured. The blue trace has a FWHM of 363.80 MHz while the red trace has a FWHM of 390.95 MHz.

The ratio of the two quality factors, before and after adding the dye, corresponds to the inverse ratio of the corresponding FWHMs:

$$\frac{Q_0}{Q} = \frac{\Delta\nu}{\Delta\nu_0}. \tag{IV.1}$$

Knowing that the total quality factor in both cases is half the intrinsic quality factor Q_i for each case, we can write:

$$\frac{Q_0}{Q} = \frac{\alpha_i + f\alpha_m}{\alpha_i}. \tag{IV.2}$$

It follows that

$$f = \frac{\Delta\nu - \Delta\nu_0}{\Delta\nu_0}\frac{\alpha_i}{\alpha_m}, \tag{IV.3}$$

where α_m is measured and α_i is determined from

$$\alpha_i = \frac{2\pi n}{\lambda Q_i}. \tag{IV.4}$$

In this experiment α_m = 0.16 cm^{-1} for 4.43 μM dye concentration. The resulting evanescent fraction f is then obtained to be 2.56%. The uncertainty in measuring the evanescent fraction is greatly affected by the ability to obtain a critically coupled WGM both before and after the dye is added. In this experiment the dip depth measurement accuracy is on the order of 1% resulting in an evanescent fraction uncertainty of approximately 15%.

The dependence of the evanescent fraction on the radial order mode number is well understood and analytical calculation reveals that for a radial order mode number equal to 8 the value of the evanescent fraction is 2.4% in good agreement to our measurement. The experiment was performed using a microsphere with 650 μm diameter at 1610 nm wavelength. Although not impossible, a radial mode order of 8 is quite improbable and another possible source of error is the fact that the dye used might be "sticking" to the resonator's surface resulting in a larger absorption coefficient and a wider FWHM. In turn, this could mimic a larger estimated evanescent fraction. Typically, the "sticking" on the resonator's surface is eliminated by controlling the pH of the solution. Since the presence of an acid or a base in the SDA2072 solution disintegrates the dye's molecules, it is impossible to use this approach.

5. Conclusions

The experimental demonstration of an extremely sensitive chemical detection mechanism for analytes in liquid solution was demonstrated in this chapter. Nano-molar changes in analyte concentration could easily be detected at two different wavelengths. At 800 nm the nm changes in concentration of ICG were monitored. ICG is used in medicine in marking cancerous tumors followed by laser ablation. However, the presence of ICG in the organism should be carefully monitored given its toxicity. Using a setup similar to the one presented in this chapter extremely small fluid samples are needed, a much desired situation in the medical discipline. The volume of the sample should be just enough to fill the entire evanescent part of a WGM resonance.

Another desired aspect in detecting trace amounts of chemicals in solution is the ability to eliminate lengthy sample preparation times by performing the analysis even in an absorbing solvent. This chapter also demonstrates detection in an absorbing solvent, once again with extremely high sensitivity.

Also, a method for measuring the evanescent fraction of a WGM that reveals critical information useful in designing a WGM chemical sensor was developed in this chapter. Knowledge of the evanescent fraction value is important both for estimating the sensitivity of such a sensor, and for packaging design in an eventual commercial application, as the evanescent fraction gives the lower bound on the sample size and shape. To our knowledge, this is the first accurate measurement of a WGM evanescent fraction.

Other applications envisioned for our sensor are in the pharmaceutical area where monitoring the drug dosage is a critical aspect. Given the miniaturized size of our

detection scheme, accurate monitoring of chemical concentration can be performed inside a typical intravenous dripping bag.

CHAPTER V

RESONANCE SHIFT EXPERIMENTS

1. Introduction

A high-sensitivity whispering-gallery-mode (WGM) assisted detection of optically non-absorbing chemicals is presented in this chapter. Laser light is injected into WGMs of fused-silica microspheres (~500 μm in diameter) using a tapered optical fiber. The high quality factor (Q) of such a microcavity makes the fiber throughput spectrum show a sharp dip on resonance. The position (in frequency) of each resonance is highly sensitive to small variations of the refractive index of the microsphere or the surrounding medium. The dependence of the resonance frequency on the surrounding medium is due to the fact that each WGM has an evanescent portion that extends outside the geometrical boundary of the dielectric microsphere.

In our experiment, a nanolayer of Nafion (a fluorinated polymer with separate hydrophilic and hydrophobic domains) is applied on the surface of a microsphere. The Nafion coating is transparent and thin enough (~30 nm) not to affect the Q of the microresonator; it is also thick enough relative to the evanescent extent of a WGM to have a noticeable effect on the resonance frequencies as its index of refraction varies in the presence of the $Ru(bipy)_3^{2+}$ cation (Tris(2,2'-bipyridine) ruthenium(II) chloride hexahydrate). The transparency of the Nafion layer at the operating wavelength is crucial in maintaining the relatively high Q of our microresonators, which in turn guarantees a narrow resonance and thus high sensitivity to a shift in frequency.

2. Theory

The frequency shift due to a change in the effective index of refraction of a WGM can be written as:

$$\Delta\nu = -\frac{\nu}{n_{eff}}\Delta n_{eff}\,. \tag{IV.5}$$

However, for the case of a Nafion nanolayer, only a fraction *f'* of a WGM is contained within the nanolayer so,

$$\Delta\nu = -\frac{\nu}{n_{eff}} f'\Delta n_{nafion}\,, \tag{IV.6}$$

and

$$f' = f\frac{t_{layer}}{\frac{\lambda}{4\pi\sqrt{n_{eff}^{\,2} - n_0^{\,2}}}}\,, \tag{IV.7}$$

where t_{layer} is the Nafion layer thickness, f is the WGM evanescent fraction, and n_0 is the refractive index of the surrounding medium. The quantity in the denominator of (IV.7) is the evanescent intensity decay length. Relation (IV.7) is an approximation valid for a layer thickness $t_{layer} \ll s = \lambda / 4\pi\sqrt{n_{eff}^{\,2} - n_0^{\,2}}$. In general, *f'* is expressed as

$$f' = \frac{\int_0^t e^{-r/s}dr}{s} = f\left(1 - e^{-t/s}\right) \tag{IV.8}$$

3. Experimental setup

The coated microsphere and the tapered fiber are immersed in de-ionized water as shown in Figure V.1. Light from a tunable diode laser (TDL) operating at 1550 nm is injected at one end of the fiber and the signal at the other end is monitored on an oscilloscope. Whenever a WGM resonance condition is met, a sharp Lorentzian dip is observed. The position (in frequency) of a WGM is recorded; then ruthenium complex is added to form a 2 μM solution.

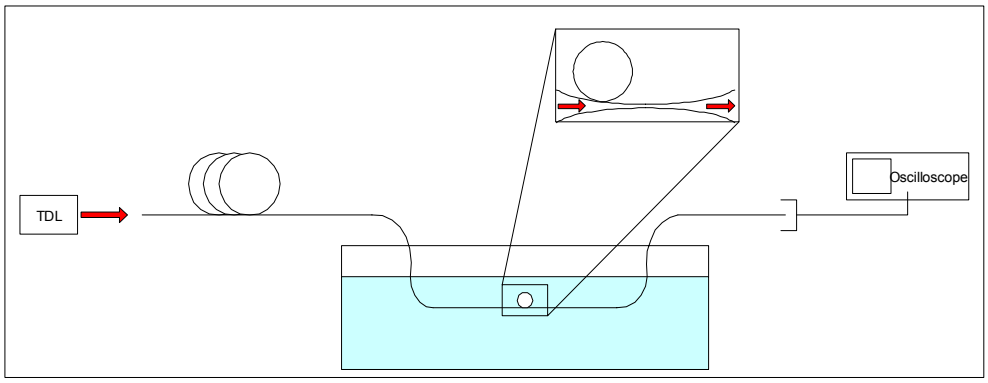

Figure V.1. Experimental setup for a WGM frequency shift measurement. Coated microsphere and tapered fiber are immersed in de-ionized water. Changes in a WGM resonance position are recorded as ruthenium complex is added.

A typical experimental result is presented in Figure V.2. The slow absorption of the ruthenium complex is accompanied by an increase in the refractive index of the Nafion coating. Since the coating is within the evanescent fraction of a WGM, this will result in a frequency shift of the resonances toward lower values. WGM frequency shifts in excess of 9 GHz can be observed for a relatively low concentration of analyte. Throughout this experiment the solution pH is maintained constant to avoid any parasitic effects on the coating.

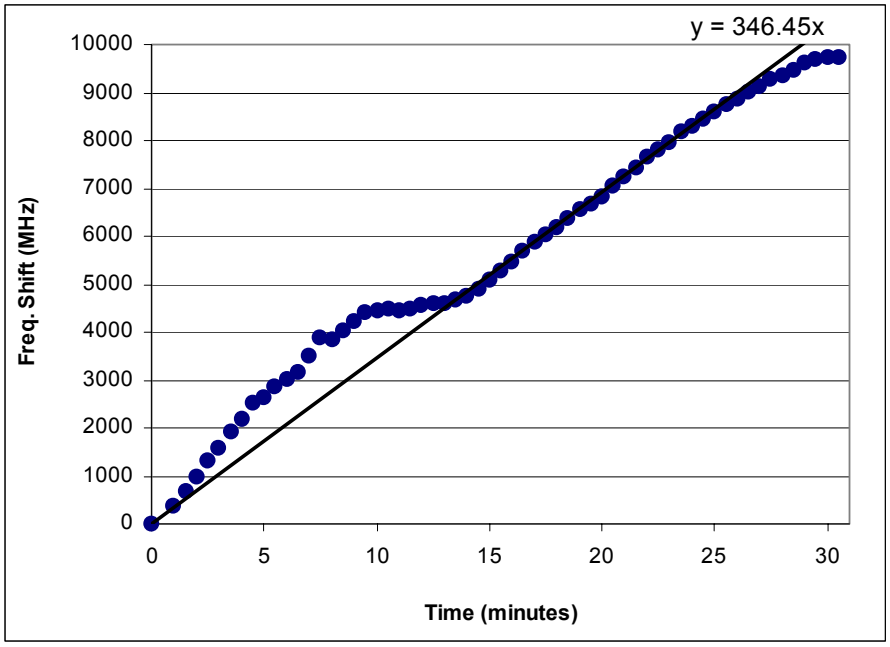

Figure V.2. WGM frequency shift of a Nafion coated microsphere while exposed to ruthenium complex.

A faster frequency shift is observed for the first ten minutes and is believed to be a result of inhomogeneity in the solution. As the solution becomes more homogeneous, the speed at which the WGM resonance frequency shifts decreases, then maintains a linear time dependence. After 30 minutes the shift of the WGM resonances appears to stop as the Nafion nanolayer becomes saturated with the absorbed ruthenium complex.

4. Conclusions

The frequency shift obtained is in good agreement with a theoretically estimated shift of 23 GHz. The estimated shift is based on a Nafion nanolayer thickness of 30 nm and a change in its index of refraction of 0.08. No measurement was made either on the nanolayer thickness or on the actual refractive index variation and it is possible that the thickness is less than 30 nm and the Δn is less than 0.08.

In conclusion, a method for chemical detection by monitoring small changes in refractive index is presented. The enhanced sensitivity of our method relies on the use of WGM resonances that allow a greater interaction pathlength within a small volume. The development of this class of sensors consisting of a WGM microresonator and an analyte-nanolayer pair for label-free detection is still under way, and these results demonstrate the feasibility of such a project.

CHAPTER VI

GENERAL CONCLUSIONS AND PERSPECTIVES

A novel sensing technique for detecting either chemicals in liquid solution or trace gases in the atmosphere is presented in this work. The technique involves the use of the response of WGM resonators to the presence of an analyte within the small evanescent field of a WGM resonance. This technique has three main characteristics required in the development of new sensors: miniaturized, highly sensitive, and inexpensive, making it the ideal next generation detection tool. Its potential applications include pharmaceuticals, medicine, forensics, safety, agriculture, and any other application that requires high sensitivity correlated with small required sample size.

The first experimental demonstration of a LS analog experiment using WGM resonators is also presented. Experimental detection of trace gases in the atmosphere was performed using this novel technique with results comparable to the standard LS technique. However, our technique permits an extreme miniaturization, the size of our active area of detection being at least four orders of magnitude smaller than that of a current standard setup. The resulting tradeoff in sensitivity is minimal and it can be eliminated in principle with small improvements in the experimental design.

A new technique for measuring the evanescent fraction of a WGM resonance is presented as well. Previous attempts in probing the evanescent fraction involved rather elaborate equipment for nano-positioning and near-field measurement. Our method relies on the precise measurement of the resonance losses incurred due to the presence of a known absorbing analyte in the evanescent region of a WGM. The measurement of the added losses is done by balancing them with corresponding coupling losses. Such a measurement can be performed in a precise manner by monitoring a WGM in the critical coupling regime and the evanescent fraction can be determined by comparing the quality factors before and after the extra loss is added.

In the past few years a considerable effort has been dedicated to obtaining various geometries of WGM resonators on a chip. Resonances were obtained but determination of the coupling regime for each resonator required invasive probing of every individual resonator with a loss inducing object. An elegant, noninvasive method for determining the coupling regime was developed in this work. It relies on a qualitative investigation of the resonator's response to a square-wave modulated input. Experimental results are in perfect agreement with the theoretical model and the coupling regime is revealed instantly given the specific response of an overcoupled or undercoupled resonator. Moreover, using modest computational resources the experimental data can be fitted with the theoretical model, one of the fit parameters being the loss ratio $x = T/\alpha l$. Other significant microresonator parameters can be also determined from the response to the square-wave modulation.

When immersed in a liquid solution, a WGM resonator acts like an extremely sensitive detector for changes in the concentration of an absorbing chemical. Nanomolar

changes in dye concentration were easily detected. Such a small concentration corresponds to less than one thousand molecules within the active volume of detection. As a consequence, individual molecules could be detected with small improvements in the experimental setup.

The detection of changes in concentration of an analyte dissolved in an absorbing solvent was also demonstrated experimentally. The same high sensitivity results in effective absorption pathlengths on the order of meters being obtained. The comparison with a typical experimental setup involving an absorption cell is not appropriate anymore since meters of pathlength are impossible for an absorbing solvent. However, if the analogy is maintained, the absolute sensitivity of our experiment is tens of orders of magnitude better than a standard experiment with an absorption cell as long as our effective absorption pathlength.

Currently, the entire setup for liquid sensing is mounted on a book size optical breadboard with the majority of the space being occupied by positioning equipment for the tapered fiber and the microsphere. In an attempt to reduce the size of the setup, optical glue was used to attach the microsphere to the tapered fiber. While successful in immobilizing the microsphere to the fiber the resonator displayed a drastic loss in its quality factor as it ended up being covered in glue, negating also its use as an evanescent-wave sensor. However, it is possible to spot-weld the microresonator to the fiber by a short exposure to a focused CO_2 laser. Similar attempts using a hydrogen-oxygen torch proved encouraging. A successful attachment of a microresonator to the tapered fiber would result in a drastic size reduction of the experimental setup.

Recently, a large enhancement of the evanescent field of a WGM resonance was experimentally demonstrated in our laboratory [73,74]. The enhancement is mediated by the excitation of surface plasmon resonances of gold nanorods grown on the surface of spherical WGM microresonator. An increase in the evanescent field of a WGM resonance would result in a proportional increase in the sensitivity of our sensor.

The sensitivity of a WGM sensor can be also increased by using controlled multimode injection from the tapered fiber into the microsphere. In principle, sensitivity enhancements as large as two orders of magnitude should be possible and previous experimental results obtained in our laboratory [75] are in good agreement with such a prediction. By controlling the shape of the tapered fiber used for WGM coupling, multimode transmission through the tapered region was obtained. For simplicity it is desirable to excite only the fundamental (HE_{11}) and the first excited mode of the tapered fiber (HE_{12}). Preliminary results in this direction were obtained that seem to indicate two-mode transmission in a tapered fiber. Accurate analytical modeling of the tapered fiber modes and inter-modal coupling is currently being performed.

Other possible directions that can be pursued in order to increase the sensitivity of our microresonator include the use of CRIT and CRIA (Coupled Resonator Induced Transparency and Coupled Resonator Induced Absorption) given their strong dependence on the coupling regime and line-narrowing respectively. Also, a laser intracavity detection mechanism can be envisioned using the WGM microlaser developed in our laboratory. Besides the enhancement due to the laser intracavity detection method, an added benefit is the access to longer wavelengths where gas absorption lines are stronger.

REFERENCES

1. M. L. Gorodetsky, A. A. Savchenkov, and V. S. Ilchenko, "Ultimate Q of Optical Microsphere Resonators," Opt. Lett. **21**, 453-455 (1996).
2. J. P. Rezac and A. T. Rosenberger, "Locking a Microsphere Whispering-Gallery Mode to a Laser," Opt. Express. **8**, 605-610 (2001).
3. J. W. Strutt (Lord Rayleigh), *The Theory of Sound*, (Dover, New York, 1945).
4. Lord Rayleigh, "Further Applications of Bessel Functions of High Order to the Whispering Gallery and Allied Problems," Phil. Mag. **27**, 100-109 (1914).
5. Lord Rayleigh, "The Problem of the Whispering Gallery," Phil. Mag. **20**, 1001-1004 (1910).
6. P. Debye, "Der Lichtdruck auf Kugeln von Beliebigem Material," Ann. Phys. **30**, 57-136 (1909).
7. G. Mie, "Beitrage zur Optik Truber Medien," Ann. Phys. **25**, 377-445 (1908).
8. M. Gastine, L. Courtois, and J. L. Dormann, "Electromagnetic Resonances in Free Dielectric Spheres," IEEE Trans. Microwave Theory Tech. **MTT-15**, 694-700 (1967).
9. P. Affolter and B. Eliasson, "Electromagnetic Resonances and Q-Factors of Lossy Dielectric Spheres," IEEE Trans. Microwave Theory Tech. **MTT-21**, 573-578 (1973).

10. D. R. Rowland and J. D. Love, "Evanescent wave coupling of whispering gallery modes of a dielectric cylinder," IEE Proceedings **140**, 177-188 (1993).

11. D. K. Armani, T. J. Kippenberg, S. M. Spillane, and K. J Vahala, "Ultra-high-Q toroid on a chip," Nature **421**, 925-929 (2003).

12. S. Schiller and R. L. Byer, "High-Resolution Spectroscopy of Whispering Gallery Modes in Large Dielectric Spheres," Opt. Lett. **16**, 1138-1140 (1991).

13. S. Lacey and H. Wang, "Directional emission from whispering-gallery modes in deformed fused-silica microspheres," Opt. Lett. **26**, 1943-1945 (2001).

14. M. L. M. Balistreri, D. J. W. Klunder, F. C. Blom, A. Driessen, J. P. Korterik, L. Kuipers, and N. F. van Hulst, "Experimental analysis of the whispering-gallery modes in a cylindrical optical microcavity," J. Opt. Soc. Am. B **18**, 465-471 (2001).

15. A. Ashkin and J. M. Dziedzic, "Observation of Resonances in the Radiation Pressure on Dielectric Spheres," Phys. Rev. Lett. **38**, 1351-1354 (1977).

16. P. Chylek, J. T. Kiehl, and M. K. W. Ko, "Optical Levitation and Partial-Wave Resonances," Phys. Rev. A **18**, 2229-2233 (1978).

17. M. Kuwata-Gonokami, R. H. Jordan, A. Dodabalapur, H. E. Katz, M. L. Schilling, R. E. Slusher, and S. Ozawa, "Polymer Microdisk and Microring Lasers," Opt. Lett. **20**, 2093-2095 (1995).

18. M. Kuwata-Gonokami and K. Takeda, "Polymer Whispering Gallery Mode Lasers," Opt. Mater. **9**, 12-17 (1998).

19. P. Rabiei, W. H. Steier, C. Zhang, and L. R. Dalton, "Polymer Microring Filters and Modulators," J. Lightwave Technol. **20**, 1968-1975 (2002).

20. G. T. Paloczi, Y. Huang, and A. Yariv, "Free-Standing all-polymer Microring Resonator Optical Filter," Electron. Lett. **39**, 1650-1651 (2003).

21. S. Ashkenazi, C.-Y. Chao, L. J. Guo, and M. O'Donnell, "Ultrasound Detection Using Polymer Microring Optical Resonator," Appl. Phys. Lett. **85**, 5418-5420 (2004).

22. C. G. B. Garrett, W. Kaiser, and W. L. Bond, "Stimulated Emission into Optical Whispering Gallery Modes of Spheres," Phys. Rev. **124**, 1807-1809 (1961).

23. P. Walsh and G. Kemeny, "Laser Operation without Spikes in a Ruby Ring," J. Appl. Phys. **34**, 956-957 (1963).

24. V. B. Damiao, E. Fotheringham, V.Shkunov, L. Czaia, and D. Z. Anderson, "Photorefractive $BaTiO_3$ Spheres and Spherical Disks," Opt. Lett. **26**, 611-613 (2001).

25. A. A. Savchenkov, V. S. Ilchenko, A. B. Matsko, and L. Maleki, "KiloHertz Optical Resonances in Dielectric Crystal Cavities," Phys. Rev. A **70**, 051804 (2004).

26. V. S. Ilchenko, A. B. Matsko, A. A. Savchenkov, and L. Maleki, "High-Efficiency Microwave and Millimeter-Wave Electro-Optical Modulation with Whispering-Gallery Resonators," Proc. SPIE **4629**, 158-163 (2002).

27. D. A. Cohen and A. F. J. Levi, "Microphotonic Millimetre-Wave Receiver Architecture," Electron. Lett. **37**, 37-39 (2001).

28. G. Farca, S. I. Shopova, and A. T. Rosenberger, "Intracavity chemical absorption sensing using microresonator whispering –gallery modes," Proc. SPIE **5855**, 427-430 (2005).

29. G. Farca, S. I. Shopova, L. A. Elizondo, A. Naweed, A. T. Rosenberger, "Evanescent-wave chemical sensing using WGM microresonators" Biophotonics/Optical Interconnects and VLSI Photonics/WBM Microcavities, 2004 Digest of the LEOS Summer Topical Meetings, 2004.

30. M. L. Gorodetsky, A. A. Savchenkov, and V. S. Ilchenko, "Ultimate Q of Optical Microsphere Resonators," Opt. Lett. **21**, 453-455 (1996).

31. D. W. Vernooy, V. S. Ilchenko, H. Mabuchi, E. W. Streed, and H. J. Kimble, "High-Q Measurements of Fused-Silica Microspheres in the Near Infrared," Opt. Lett. **23**, 247-249 (1998).

32. V. B. Braginsky, M. L. Gorodetsky, and V. S. Ilchenko, "Quality-Factor and Nonlinear Properties of Optical Whispering Gallery Modes," Phys. Lett. A **137**, 393-397 (1989).

33. L. Collot, V. Lefevre-Seguin, M.Brune, J.-M. Raimond, and S. Haroche, "Very High-Q Whispering-Gallery Mode Resonances Observed in Fused Silica Microspheres," Europhys. Lett. **23**, 327-334 (1993).

34. A. J. Campillo, J. D. Eversole, and H. B. Lin, "Cavity Quantum Electrodynamic Enhancement of Stimulated Emission in Microdroplets," Phys. Rev. Lett. **67**, 437-440 (1991).

35. H. Mabuchi and H. J. Kimble, "Atom Galleries for Whispering Atoms-Binding Atoms in Stable Orbits Around an Optical Resonator," Opt. Lett. **19**, 749-751 (1994).

36. D. Roess and G. Gehrer, "Selection of Discrete Modes in Toroidal Lasers," Proc. IEEE **52**, 1359-1360 (1964).

37. H. M. Tzeng, K. F. Wall, M. B. Long, and R. K. Chang, "Laser Emission from Individual Droplets at Wavelengths Corresponding to Morphology-Dependent Resonances," Opt. Lett. **9**, 499-501 (1984).

38. H. Latifi, A. Biswas, R. L. Armstrong, and R. G. Pinnick, "Lasing and Stimulated Raman Scattering in Spherical Droplets-Time, Irradiance, and Wavelength Dependence," Appl. Opt. **29**, 5387-3592 (1990).

39. R. L. Armstrong, J.-G. Xie, T. E. Ruekgauer, and R. G. Pinnick, "Energy Transfer Assisted Lasing from Microdroplets Seeded with Fluorescent Sol," Opt. Lett. **17**, 943-945 (1992).

40. H.-B. Lin, J. D. Eversole, and A. J. Campillo, "Spectral Properties of Lasing Microdroplets," J. Opt. Soc. Am. B **9**, 43-50 (1992).

41. H. Taniguchi and S. Tanosaki, "3-Color Whispering Gallery Mode Dye Lasers Using Dye-Doped Liquid Spheres," Jpn. J. Appl. Phys. II **32**, L1421-L1424 (1993).

42. H. Taniguchi, H. Tomisawa, and Sarjono, "Morphology-Dependent Dye Lasing from a Single Microdroplet with Double-Layered Dye Doping," Opt. Lett. **19**, 366-369 (1994).

43. F. Lissillour, P. Feron, N. Dubreuil, P. Dupriez, M. Poulain, and G. M. Stephan, "Erbium-Doped Microspherical Lasers at 1.56 μm," Electron. Lett. **36**, 1382-1384 (2000).

44. F. Lissillour, D. Messager, G. Stephan, and P. Ferron, "Whispering-Gallery-Mode Laser at 1.56 μm Excited by a Fiber Taper," Opt. Lett. **26**, 1051-1053 (2001).

45. H. Fujiwara and K. Sasaki, "Microspherical Lasing of an Erbium-Ion-Doped Glass Particle," Jpn. J. Appl. Phys. II **41**, L46-L48 (2002).

46. A. Polman, B. Min, J. Kalkman, T. J. Kippenberg, and K. J. Vahala, "Ultralow-Threshold Erbium-Implanted Toroidal Microlaser on Silicon," Appl. Phys. Lett. **84**, 1037-1039 (2004).

47. S. I. Shopova, G. Farca, A. T. Rosenberger, W. M. S. Wickramanayake, N. A. Kotov, "Microsphere whispering-gallery-mode laser using HgTe quantum dots," Appl. Phys. Lett. **85**, 6101-6103 (2004).

48. S. Blair and Y. Chen, "Resonant-Enhanced Evanescent-Wave Fluorescence Bio-Sensing with Cylindrical Optical Cavities," Appl. Opt. **40**, 570-582 (2001).

49. R. W. Boyd and J. E. Heebner, "Sensitive Disk Resonator Photonic Biosensor," Appl. Opt. **40**, 5742-5747 (2001).

50. E. Krioukov, D. J. W. Klunder, A. Driessen, J. Greve, and C. Otto, "Sensor Based on an Integrated Optical Microcavity," Opt. Lett. **27**, 512-514 (2002).

51. E. Krioukov, J. Greve, and C. Otto, "Performance of Integrated Optical Microcavities for Refractive Index and Fluorescence Sensing," Sensors and Actuators B **90**, 58-67 (2003).

52. F. Vollmer, D. Braun, A. Libchaber, M. Khoshsima, I. Teraoka, and S. Arnold, "Protein Detection by Optical Shift of a Resonant Microcavity," Appl. Phys. Lett. **80**, 4057-4059 (2002).

53. F. Vollmer, S. Arnold, D. Braun, I. Teraoka, and A. Libchaber, "Multiplexed DNA Quantification by Spectroscopic Shift of Two Microsphere Cavities," Biophys. J. **85**, 1974-1979 (2003).

54. S. Arnold, M. Khoshsima, I. Teraoka, S. Holler, and F. Vollmer, "Shift of Whispering-Gallery Modes in Microspheres by Protein Adsorption," Opt. Lett. **28**, 272-274 (2003).

55. I. Teraoka, S. Arnold, and F. Vollmer, "Perturbation Approach to Resonance Shifts of Whispering-Gallery Modes in a Dielectric Microsphere as a Probe of a Surrounding Medium," J. Opt. Soc. Am. B **20**, 1937-1946 (2003).

56. A.T. Rosenberger, J. P. Rezac, S. C. Koterba, and S. A. Bates, "Temperature tuning of optical whispering-gallery modes as a sensitive probe of thermal interaction between a fused-silica microsphere and the ambient air," CLEO 2002 Technical Digest, Lasers and Electro-Optics, 217-218 (2002).

57. J. D. Love, W. M. Henry, W. J. Stewart, R. J. Black, S. Lacroix and F. Gonthier, "Tapered single-mode fibres and devices. I. Adiabaticity Criteria," IEE Proceedings **138**, 343-354 (1991).

58. R. J. Black, S. Lacroix, F. Gonthier and J. D. Love, "Tapered single-mode fibres and devices. II. Experimental and theoretical quantification," IEE Proceedings **138**, 355-364 (1991).

59. A. Yariv, *Optical Electronics in Modern Communications* (Oxford, New York, 1997).

60. M. J. Humphrey, *Calculation of Coupling Between Tapered Fiber Modes and Whispering-Gallery Modes of a Spherical Microlaser*, PhD Diss., Physics Dept., Oklahoma State University (2004).

61. F. Bilodeau, K. O. Hill, S. Faucher, and D. C. Johnson, "Low-loss highly overcoupled fused couplers: Fabrication and sensitivity to external pressure," J. Lightwave Technol. **6**, 1476-1482 (1988).

62. T. A. Birks and Y. W. Li, "The Shape of fiber Tapers," J. Lightwave Technol. **10**, 432-438 (1992).

63. T. E. Dimmick, G. Kakarantzas, T. A. Birks, and St. J. Russell, "Carbon dioxide laser fabrication of fused-fiber couplers and tapers," Appl. Opt. **38**, 6845-6848 (1999).

64. J. P. Rezac, *Properties and Applications of Whispering-Gallery Mode Resonances in Fused Silica Microspheres*, PhD Diss., Physics Dept., Oklahoma State University (2002).

65. S. Deng, W. Cai, V. N. Astratov, "Numerical study of light propagation via whispering gallery modes in microcylinder coupled resonator optical waveguides," Opt. Express **12**, 6468-6480 (2004).

66. A. T. Rosenberger, Department of Physics, Oklahoma State University, 145 Physical Sciences, Stillwater, OK 74078-3072 (personal communication, 2001).

67. The HITRAN molecular spectroscopic database, (1996).

68. S.-I Chou, D. S. Baer, and R. K. Hanson, "Diode laser absorption measurements of CH_3Cl and CH_4 near 1.65 μm," Appl. Opt. **36**, 3288-3293 (1997).

69. A. Boschetti, D. Bassi, E. Iacob, S. Iannotta, L. Ricci, M. Scotoni, "Resonant photoacoustic simultaneous detection of methane and ethylene by means of a 1.63-μm diode laser," Appl. Phys. B **74**, 273-278 (2002).

70. G. Farca, S. I. Shopova, and A. T. Rosenberger, “Cavity Enhanced Laser Spectroscopy Using Microresonator Whispering-Gallery Modes.” Tech. Dig., Conf. on Lasers and Electro-Optics and Quantum Electronics and Laser Science Conf. (CLEO/QELS), May 23-25, 2006, Long Beach, CA (2006).

71. Jason Crull, *Degradation behavior of indocyanine green dye during high intensity laser irradiation*, Masters Thesis, Physics Dept., Oklahoma State University (1994).

72. http://www.hwsands.com/productlists/laserdyes/ld951to1000.htm.

73. S. I. Shopova, C. W. Blackledge, A. T. Rosenberger, and N. F. Materer, “Gold nanorods grown from HgTe nanoparticles directly on various surfaces,” Appl. Phys. Lett. **89**, 023120 (2006).

74. S. I. Shopova, C. W. Blackledge, G. Farca, A. T. Rosenberger;"Enhancement of Evanescent Coupling to Whispering-Gallery Modes Caused by Au Nanorods Grown on a Microresonator Surface," Tech. Dig., Conf. on Lasers and Electro-Optics and Quantum Electronics and Laser Science Conf. (CLEO/QELS), May 23-25, 2006, Long Beach, CA (2006).

75. A. T. Rosenberger, A. Naweed, G. Farca, and S. I. Shopova, “Enhanced evanescent-wave sensing using multimode coupling to microresonator whispering-gallery modes,” 2003 OSA Annual Meeting, Tucson, AZ, 2003.

VITA

George Farca

Candidate for the Degree of

Doctor of Philosophy

Thesis: CAVITY-ENHANCED EVANESCENT-WAVE CHEMICAL SENSING USING MICRORESONATORS

Major Field: Physics

Biographical:

Personal Data: Born in Timisoara, Romania on November 3, 1972, the son of Gheorghe and Maria Farca.

Education: Received Bachelor of Science degree in Physics from The West University of Timisoara, Romania in June 1996; Completed the requirements for the Doctor of Philosophy degree in Physics at Oklahoma State University in December, 2006.

Name: George Farca Date of Degree: December, 2006

Institution: Oklahoma State University Location: Stillwater, Oklahoma

Title of Study: CAVITY-ENHANCED EVANESCENT-WAVE CHEMICAL SENSING USING MICRORESONATORS

Pages in Study: 104 Candidate for the Degree of Doctor of Philosophy

Major Field: Physics

Scope and Method of Study: The purpose of this research was to examine fused silica microresonators into which light was evanescently coupled into whispering-gallery modes (WGMs) using a tapered optical fiber. The high quality factor (Q) of these microcavities makes a sharp dip in a frequency scan when the resonance criterion is met. The depth and width of the dip are determined by the coupling coefficient between the coupler and the microsphere, and the intrinsic loss of the cavity. The use of these modes as sensors was examined.

Findings and Conclusions: Introducing an absorber in the evanescent field of the microresonator's WGM changes the round-trip loss of the cavity and hence a change in dip depth, width, and frequency of a WGM is observed. Absorbers studied in the dissertation include methane, methyl chloride, ethylene, indocyanine green dye in methanol at 800 nm, SDA2072 in methanol at 1650 nm, and ruthenium complex in water. Less than nM concentrations of dye in solution can be easily detected. Trace gas amounts in atmosphere could also be detected.

ADVISER'S APPROVAL: Albert T. Rosenberger